MAGNETOELASTIC CHARACTERIZATION

AND DOMAIN ANALYSIS OF MAGNETIC

THIN FILMS AND MULTILAYERS

THESIS

Presented to the Graduate Council
of Texas State University-San Marcos
in Partial Fulfillment
of the Requirements

for the Degree

Master of SCIENCE

by

Joel H. Dunn Jr., B.S.

San Marcos, Texas
May 2006

MAGNETOELASTIC CHARACTERIZATION

AND DOMAIN ANALYSIS OF MAGNETIC

THIN FILMS AND MULTILAYERS

Committee Members Approved:

_____

Dr. Ir. Wilhelmus J. Geerts, Chair

_____

Dr. Heather C. Galloway

_____

Dr. Victor Michalk

Approved by:

_____

Dr. Michael Willoughby

Dean of the Graduate College

COPYRIGHT

By

Joel H. Dunn Jr.

2006

ACKNOWLEDGEMENTS

I would like to express my deepest gratitude to my beautiful and loving wife, Clancy. Throughout the course of my graduate studies, she has been extremely understanding and incredibly patient. Without her love and support, I never could have made it this far. I would also like to thank my wonderful daughter, Sydney, who unknowingly inspires me to strive for success and who motivates me to attain my full potential. I would also like to thank my parents, Agnes and Joel Dunn Sr., and my sister, Courtney, for their support throughout my life and my education. It is also important for me to thank Ms. Dian Peschel for her unwavering support, and Mr. Chad Barger for his loyal friendship throughout the years.

Academically and professionally I owe a great debt of gratitude to Dr. Geerts, who took on the arduous task of becoming my research advisor back in my undergraduate years. The knowledge I have gained from him is invaluable, and I feel privileged to have had the opportunity to work under his supervision. I also want to thank Dr. Galloway and Dr. Michalk for serving on my committee, and every member of the Physics faculty (Dr. Spencer, Dr. Donnelly, and Dr. Olson) as well as Professor Stouder from the Technology department at Texas State University-San Marcos. I have obtained an excellent education thanks to their commitment to teaching and expert instruction. My colleagues also deserve my deepest appreciation for their support and assistance throughout the course of my studies here at Texas State.

TABLE OF CONTENTS

Page

LIST OF TABLES

LIST OF FIGURES

CHAPTER 1

INTRODUCTION

Magnetic materials are a vital component in many modern technological applications. In order to improve magnetic devices and memories, and promote technological progress, innovative materials must be fabricated and characterized. The focus of this thesis is a comprehensive investigation of the magnetic and magnetoelastic properties of a selected array of ferromagnetic materials, including thin films (NiFe) and rare earth/transition metal alloy multilayers (TbFe/FeCo).

The research presented in this thesis initially stemmed from research assistance incurred from Southwest Research Institute. Southwest Research Institute was seeking magnetic and magnetoelastic characterization for an array of multilayered thin films with the objective of finding a suitable material to be used in sensors to detect fatigue cracks in turbine jet engines. The desire was to develop a highly magnetostrictive, low coercive film to deposit inside the jet engine housing. However, there is no single element or alloy known that simultaneously exhibits the highly magnetostrictive, soft magnetic behavior required for such an application. It was proposed that the desired properties could be obtained by alternating thin layers of FeCo, a soft magnetic alloy, and terbium, a giant magnetostrictive rare earth element that was also alloyed with iron (TbFe). Multilayered films (TbFe/FeCo) with varying numbers of layers and varying layer thicknesses were

deposited to undergo magnetoelastic characterization using the magnetostriction setup here at Texas State University. In addition to the TbFe/FeCo multilayers, NiFe films are also examined in this thesis. NiFe films are widely used in magnetic read/write heads and magnetic recording media. The NiFe samples studied were fabricated by Claude Garrett during his research here at Texas State. The NiFe samples were single layers of NiFe alloy ranging in thickness from 100 to 800 nm.

In addition to magnetic and magnetoelastic characterization of the selected samples, a secondary motivation for the research was to optimize the characterization instruments; in particular, the Scanning Kerr Microscope. The goal was to ultimately produce a finalized version of the instrument that could reliably produce high quality quantitative domain images with the highest possible resolution and be simple enough for an undergraduate researcher to operate.

CHAPTER 2

THEORETICAL BACKGROUND

2.1   Magnetism in Matter and Ferromagnetic Order

Magnetism and the magnetic properties of materials are based on concepts

derived from the existence of the magnetic dipole moment. The magnetic dipole moment

can be introduced by first considering a loop enclosing an area, (A), and carrying a

current, (I).
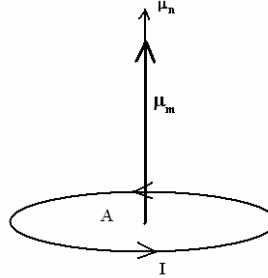
Figure 2.1
Magnetic moment produced by a circulating current

The magnetic dipole moment, or more conveniently, the magnetic moment (μ_m) can be

defined as:

$$\boldsymbol{\mu}_\mathbf{m} = IA\boldsymbol{\mu}_\mathbf{n} \tag{2.1}$$

where $\boldsymbol{\mu}_\mathbf{n}$ is a unit vector normal to the enclosed area of the loop.

If placed in an external magnetic field (**B**), the magnetic moment will experience a

torque, (τ) as it tries to align in the direction of the field.
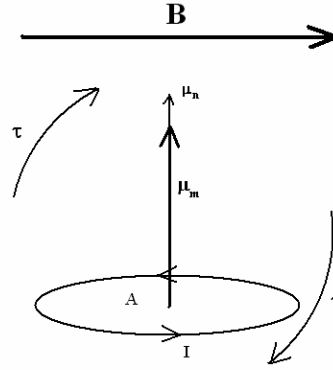
Figure 2.2
Torque experienced by magnetic moment due to external B- field

Because the magnetic moment is represented as a circulating current, it also creates its own magnetic induction field (B), with field lines emanating in the direction of the magnetic moment, similar to the magnetic field lines generated by a bar magnet.
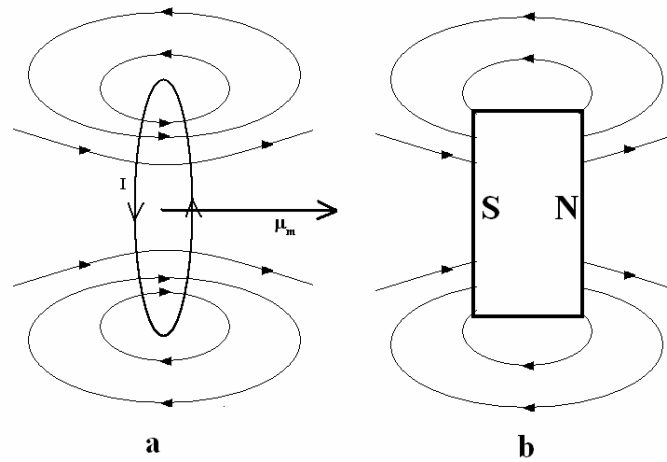
Figure 2.3
B-field generated by: a) current loop and b) bar magnet

The magnetic field, at a point (P) along the axis through the center of the area enclosed by the loop can be determined by the Biot-Savart Law:

$$\mathbf{B} = \frac{\mu_0}{4\pi} \oint_C \frac{Idl \times \mathbf{r}}{r^3}$$

(2.2)

where μ_0 is the permeability of free space, **r** is the vector between a point on the loop and the point (P) where the B field is observed, and r is the modulus of the vector **r**. For the specific case of the circular current loop, the magnitude of the B field at a point (P) directly on the axis is:

$$B = \frac{\mu_0 I}{2R} \sin^3 \theta \qquad (2.3)$$

where R is the radius of the current loop and θ is the angle between the axis and a vector connecting (P) to the loop[1].

2.1.1 Microscopic Origins of Magnetic Properties

The principle of magnetic moments can be applied to describe the magnetic properties of matter by assuming that the electrons in atoms act as current loops, giving rise to atomic magnetic moments. The total atomic magnetic moment is comprised of two contributions. One contribution is the orbital magnetic moment (μ_L), due to the orbital angular momentum (L) of the electron. Since current is charge/unit time, the current generated by an electron "orbiting" an atom can be expressed by:

$$I = \frac{-e}{period} \rightarrow \frac{-e\omega}{2\pi} \qquad (2.4)$$

here (e) is the elementary charge, and ω is angular frequency of the electron. If the electron has an "orbit" of radius (r), the orbital magnetic moment (μ_L), can be expressed as:

$$\mu_L = I(\pi r^2) = \frac{-e\omega r^2}{2} \tag{2.5}$$

and since

$$L = m_e(v)r = m_e(\omega r)r \tag{2.6}$$

(μ_L) can be expressed as:

$$\boldsymbol{\mu_L} = -\frac{e}{2m_e}\mathbf{L} \tag{2.7}$$

This shows that the orbital magnetic moment is proportional to the orbital angular

momentum by a factor of ½ of the charge to mass ratio of the electron.

In addition to the orbital magnetic moment, the electrons also have a spin magnetic

moment (μ_s) associated with their intrinsic spin (S). This contribution is quantitatively

expressed as:

$$\boldsymbol{\mu_s} = -\frac{e}{m_e}\mathbf{S} \tag{2.8}$$

which is similar to the orbital contribution but has a ratio that is a factor of 2 greater. The

total atomic magnetic moment (μ_{at}) is the vector sum of the orbital and spin

contributions, and can be conveniently expressed as:

$$\boldsymbol{\mu}_{at} = \gamma\hbar\mathbf{J} \tag{2.9}$$

where $\hbar$ **J** is the sum of the quantized orbital and spin angular momentum ($\hbar$(**L+S**)), and

the constant γ is the gyromagnetic ratio; the ratio of the atomic magnetic moment to the

total angular momentum. The constant (γ), and thus μ_{at}, can be expressed in terms of the

constants: (g) the spectroscopic splitting factor, and μ_B, the Bohr magneton.

$$-\gamma\hbar \equiv g\mu_B \rightarrow \boldsymbol{\mu}_{\mathbf{at}} = g\mu_B\mathbf{J} \tag{2.10}$$

the spectroscopic splitting factor (g) has a value of 2.0023, and the value of the Bohr

magneton (μ_B) is e $\hbar$/ $2m_e$, which is equal to the magnetic moment of a free electron

(S = 1/2 $\hbar$).

Since the angular momenta of the electrons, and thus their magnetic moments, are vector

quantities, equal and opposite values of L,S and ultimately **J**, will cancel, resulting in a

null magnetic moment for closed electron shells. The equal and opposite nature of the

angular momenta in closed shells is a direct result of the Pauli exclusion principle, which

implies that the wave functions of electrons (in general all fermions) must be totally anti-

symmetric, causing their wave functions to vanish if two particles exist in the same

energy eigenstate. For electrons, which are spin ½ particles, the only possible values for S

are +/- ½, so the total spin and angular momentum, and thus the magnetic moment, for

closed shells is zero. This implies that only unfilled electron shells contribute to the

overall atomic magnetic moment.

2.1.2   Macroscopic Theory of Magnetism

Extending the idea of atomic magnetic moments to a volume (V) containing many

atoms, the magnetization vector (**M**) can be defined as:

$$\mathbf{M} = \frac{1}{V}\sum_{i=1}^{N}\boldsymbol{\mu}_{\mathbf{at}} = n_{at}\boldsymbol{\mu}_{\mathbf{av}} \tag{2.11}$$

where n_{at} is the number atoms per unit volume, and $\boldsymbol{\mu}_{\mathbf{av}}$ is the average magnetic moment

per atom. If the volume above is placed in a magnetic field ($\mathbf{B_0}$), the atomic magnetic

moments in the material will orient along the direction of the field, creating their own

magnetic field that is proportional to the magnetization (**M**). Therefore, the total field at a point inside the material involves a contribution from the external magnetizing field and the magnetization of the material, and can be expressed by:

$$\mathbf{B} = \mathbf{B_0} + \mu_0\mathbf{M} \tag{2.12}$$

When studying magnetic materials, it is often convenient to separate the internal induced magnetic field and the magnetizing field. This magnetizing field is commonly called the magnetic field intensity, and is denoted (**H**). It can be easily derived from equation 2.12:

$$\mathbf{H} = \frac{1}{\mu_0}\mathbf{B} - \mathbf{M} \quad (2.13) \qquad \text{or:} \qquad \mathbf{H} = \frac{1}{\mu_0}\mathbf{B_0} \tag{2.14}$$

Now that the magnetic field intensity (H) has been formally introduced, it is now appropriate to proceed to intrinsic magnetic properties of materials, such as magnetic susceptibility (χ_m). For most materials, the magnetic susceptibility is defined as the magnetization per unit magnetizing field or:

$$\chi_m = \frac{M}{H} \tag{2.15}$$

However, it should be noted that this relation will require some modification when dealing with the materials that posses a spontaneous magnetization like ferromagnetic, and ferrimagnetic materials. The former case will be presented in more detail in the subsequent sections.

2.1.3 Classifications of Magnetic Materials

There are generally five classifications of magnetism: diamagmetism, paramagnetism, antiferromagnetism, ferromagnetism, and ferrimagnetism. Magnetic materials usually fall into one of these classes based on their magnetic properties, i.e. susceptibility, relative orientation of magnetic moments, and presence of spontaneous magnetization.

Diamagnetism: Materials are said to be diamagnetic if they possess a very small, negative susceptibility at and near room temperature. If placed in an eternal field, the magnetization vector (**M**) is opposite the direction of the external field. Typically, diamagnetic materials are atoms with closed electron shells. At temperatures below a certain critical temperature (T_{cr}), the susceptibility of some diamagnetic materials becomes (–1), and the materials become superconducting, meaning they exhibit no electrical resistance. However, other than superconductivity, diamagnetic materials have no useful widespread applications based on their magnetic properties.

Paramagnetism: Paramagnetic materials generally have a small positive magnetic susceptibility. The magnetic moments in paramagnetic material are randomly oriented, except when introduced to an external magnetic field. This random orientation of magnetization generally results in a very small or zero net macroscopic magnetization. In the presence of a magnetizing field, the moments will align in the direction of the field, but if the field goes to zero, the moments assume their random orientation; therefore they exhibit no spontaneous magnetization.

Antiferromagnetism: Materials are classified as antiferromagnetic if they have a crystal lattice that contains magnetic moments of equal magnitude, with opposite susceptibilities. In the simplest case, adjacent sub lattices posses equal and opposite magnetization vectors, thus canceling any net magnetization. The figure below illustrates this principle:
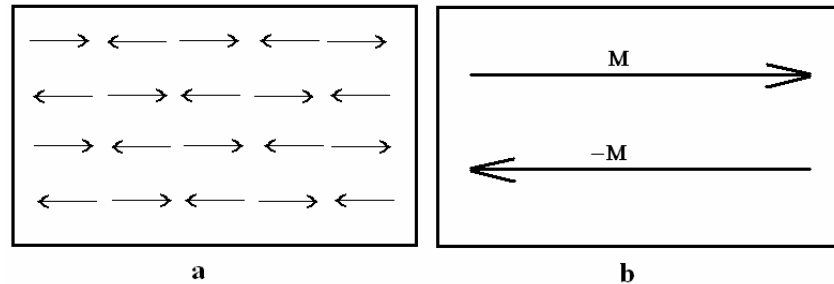
Figure 2.4
Orientation of a) magnetic moments; b) magnetization vectors, in
a simple antiferromagnetic material

.

It is clear from Figure 2.4b that the magnetization vectors in an antiferromagnetic material are equal in magnitude and opposite in direction resulting in no net macroscopic magnetization.

Ferrimagnetism: Ferrimagnetic materials have a magnetic structure similar to that of antiferromagnetic materials, with one exception: the magnetization vectors representing the sum of the magnetic moments have opposite directions, but different magnitudes.
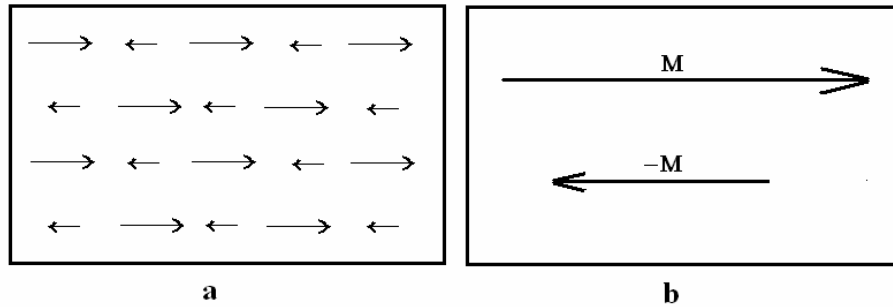
Figure 2.5
Orientation of a) magnetic moments; b) magnetization vectors in a ferrimagnetic material

Ferrimagnetic materials have a small positive susceptibility, because the magnetic

moments that align with the external field usually have the greater magnitude. Another

consequence of the differing magnitudes is a small, but stable, spontaneous

magnetization.

Ferromagnetism: Ferromagnetic materials have a very large, positive (sometimes infinite)

susceptibility and a large spontaneous magnetization. Unlike ferrimagnetic materials, all

of the magnetic moments in a ferromagnet tend to align in the direction of the

magnetizing field. Because the majority of this thesis deals with ferromagnetic materials

and their properties, they are discussed in greater detail in the next section.

2.1.4   Ferromagnetic Order and Exchange Energy

The spontaneous magnetism of a ferromagnetic material can be understood by

considering the electron configuration of a single atom of a ferromagnetic material (Fe).

For example, the electron configuration of an iron atom is [Ar] $3d^6 4s^2$.
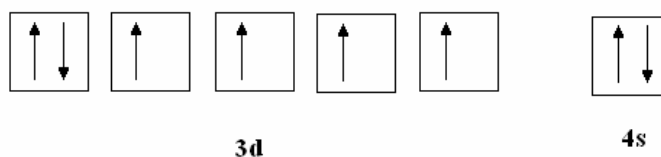
Figure 2.6
Electron configuration of an isolated iron Atom

All orbitals below 3d are filled and make no contribution to the magnetic moment of the atom. It can be seen from figure 2.6 that the 3d orbital contains 4 unpaired electrons. This configuration is the result of a lower energy configuration, versus filling the 3d shell before filling the 4s shell as dictated by Hund's Rules and the Pauli Exclusion Principle. These unpaired spins result in a net magnetic moment for the atom, as well as an induced internal field causing the magnetic moments of neighboring atoms in a crystal lattice to align in the same direction, thus further lowering the total energy of the system. The electron configuration of the isolated iron atom has a net magnetic moment of $4\mu_B$. In a crystal, the effect is slightly smaller than that an isolated atom. For iron, the actual magnetic moment per atom is closer to $2.22\mu_B$.[2] The internal field generated by the magnetic moments is often called the exchange field, or molecular field and is proportional to the magnetization (**M**) of the material. It is also responsible for the alignment of the moments or magnetic ordering, in this case, ferromagnetic ordering. While stable at low temperatures, magnetic ordering is opposed by thermal agitation, and above a certain temperature, the Curie temperature (T_C), the ordering and thus spontaneous magnetization disappear completely and the material behaves as paramagnetic.

The exchange field is responsible for the quantum mechanical exchange interaction between the spins of two neighboring electrons of atoms i and j. The energy (U) of the two interactions between these electrons is represented in the Heisenberg model as:

$$U = -2J\mathbf{S}_i \cdot \mathbf{S}_j \qquad (2.16)$$

where the quantity J is the exchange integral, related to the overlap of the charge distributions of atoms i and j. This expression is often used to quantify the exchange energy of a ferromagnetic material. It will be seen in the following sections that the exchange energy plays an important role in describing the behavior of ferromagnetic materials[3].

2.1.5   Ferromagnetic Domains

When a ferromagnetic material is maintained below its Curie temperature (T_c), it is expected that the exchange interactions will dominate and lead to a parallel alignment of atomic magnetic moments within the sample, producing a spontaneous magnetization even with no external field present, but in fact this is not the case. If a ferromagnetic material is heated above its Curie temperature, and allowed to cool in the absence of a magnetic field, it will be found that the material will have no spontaneous macroscopic magnetization. This is the result of the formation of magnetic domains. Magnetic domains are areas within a crystal where the magnetization is in only one direction. By forming domains, the material has lowered its total energy state by closing the magnetic field lines generated by the formation of magnetic poles on the edges of the sample.
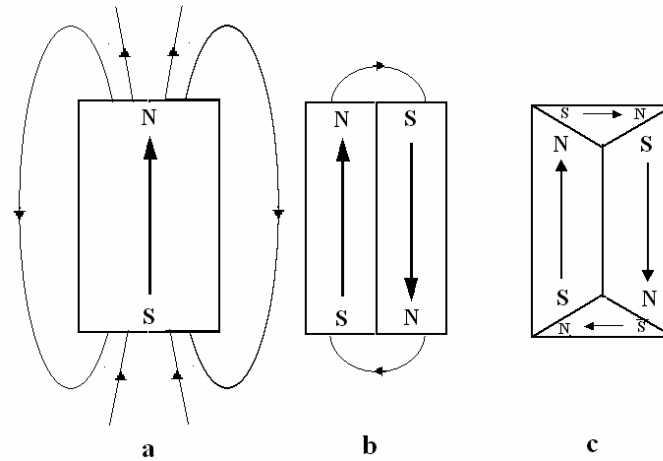
Figure 2.7
Domain configurations: a) single domain; b) two domains separated by 180° domain wall; c) closure domains added to (b) separated by 90° domain walls

Since there is magnetostatic energy stored in a magnetic field, it can be seen from figure 2.7b, that this energy can be reduced by separating the sample into two domains, and reduced further by the addition of closure domains as in figure 2.7c. The formation of domains (i.e., number and geometry) is dictated by competition between the exchange interaction and the dipolar interaction. The competition arises from the opposing nature of the two interactions. For instance, the exchange interaction favors all magnetic moments aligned in a single direction. In contrast, the dipolar interaction favors opposite orientations of adjacent moments to close the field lines. Since there is no simultaneous solution for minimizing the energy of both interactions, ferromagnetic materials submit to a compromise resulting in the lowest total energy.

In addition to the exchange and the dipolar interactions, magnetocrystalline anisotropy also plays a role in determining the behavior of magnetic domains. The direction of magnetization within the domains is usually determined by the crystal structure of the material. In many magnetic materials there is a crystal direction along which the moments prefer to be magnetized. Such a direction is known as an easy

direction or easy axis. As the name suggests, it is "easy" to magnetize a material along its easy direction, meaning that magnetic saturation can be reached for a modest cost in energy along the easy direction. In contrast, as the magnetic moments are rotated away from the easy direction, they do so at the expense of an increase in energy. The axis that demands the most energy to align the moments is known as a hard axis, or hard direction. The excess energy cost of aligning the moments along a hard axis is the magnetocrystalline anisotropy energy.

2.1.6 Domain Walls

When domains form in a material, they are separated by a domain wall. As with the domain structure, there is a compromise of interactions involved with the interface between adjacent domains. In an ideal system, as well as in bulk material, a Bloch wall separates two domains. A domain wall separating two domains is a compromise between the exchange energy and the anisotropy energy resulting in a finite thickness. This energy compromise is inevitable due to the opposing nature of the exchange and anisotropy energies.

Suppose a domain wall separates two domains with an 180° difference in magnetization along an easy axis. If the domain wall existed with the shortest distance possible, between two adjacent atomic planes, it would do so for virtually no cost in anisotropy energy, because no magnetic moments would be rotated away from the easy direction. However, this arrangement it not favorable due to the enormous cost in exchange energy for having adjacent moments anti-parallel, recalling that the exchange interaction is at its lowest energy when all moments are aligned parallel. Therefore the

exchange interaction would prefer that the magnetic moments rotate slightly over a large distance to minimize energy cost. The cost in exchange energy for a line transition over a distance of N+1 atoms can be derived from a classical interpretation of the Heisenberg model for exchange energy (Eq. 2.16).

$$w_{ex} = JS^2\varphi^2 \tag{2.17}$$

where J is the exchange integral, S is the spin quantum number, (φ) is the angle between neighboring atoms and w_{ex} is the energy associated with parallel spins. If the angle (φ) between neighboring atoms is π/N equation (Eq. 2.17) becomes:

$$Nw_{ex} = \frac{JS^2\pi^2}{N} \tag{2.18}$$

Conversely, a similar problem occurs when the exchange energy is minimized. Ideally the lowest cost in exchange energy results from a transition over an infinite number of atoms. However this would result in an infinite number of magnetic moments rotated away from their easy axes, thus summing up to an infinite anisotropy energy. The actual domain wall thickness is a compromise that results in the lowest total energy of the transition between domains.
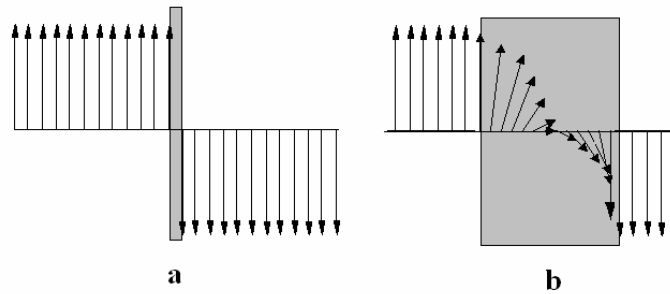
Figure 2.8
Domain walls; a) narrow wall, high exchange, low anisotropy; b) low exchange, high anisotropy

The energy per unit area of the domain wall (σ_w) is the sum of the exchange (σ_{ex}) and anisotropy contributions[3] (σ_{an}).

$$\sigma_w = \sigma_{ex} + \sigma_{an} \tag{2.19}$$

with:

$$\sigma_{ex} = \frac{\pi^2 JS^2}{Na^2} \quad \text{and} \quad \sigma_{an} = KNa \tag{2.20}$$

where a is the lattice constant and K is a constant associated with the anisotropy of the material. The minimum energy per unit volume (σ_w) of the domain wall with respect to N is therefore:

$$\frac{\partial \sigma_w}{\partial N} = \frac{\partial}{\partial N}\left(\frac{\pi^2 JS^2}{Na^2} + KNa\right) = 0 = -\frac{\pi^2 JS^2}{N^2 a^2} + Ka \rightarrow N = \sqrt{\frac{\pi^2 JS^2}{Ka^3}} \tag{2.21}$$

The result of equation (2.21) predicts the total energy per unit volume of the most energetically favorable domain wall to be:

$$\sigma_w = 2\pi\left(\frac{KJS^2}{a}\right)^{\frac{1}{2}} \tag{2.22}$$

As previously stated, in an ideal system, as well as in bulk material, a Bloch wall separates two domains. In a Bloch wall, the moments rotate in a plane perpendicular to the direction of the domain wall width, and parallel to the direction of the magnetization as in the figure below:
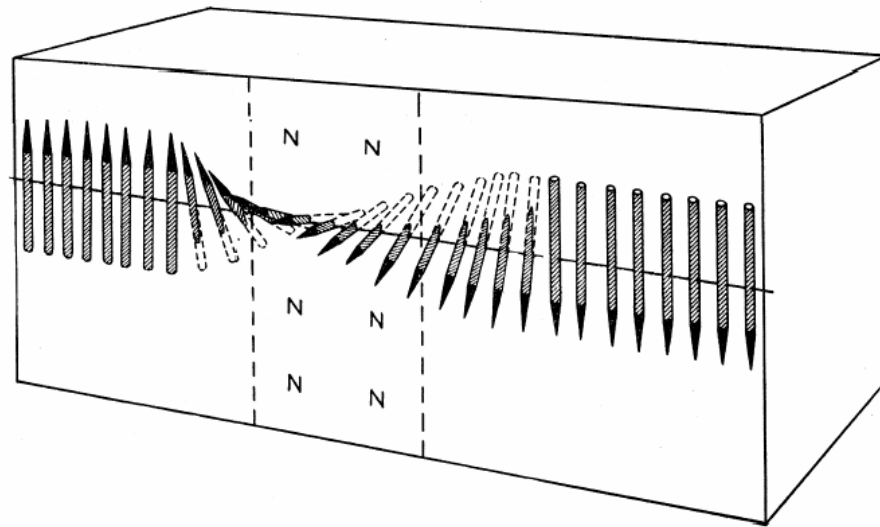
Figure 2.9
Rotation of magnetic moments in a Bloch Wall[4]

For instance, in Cartesian coordinates, if the magnetization were in the y-direction, and

the domain wall spanned the x-direction, the axis of rotation of the moments would be

along the x-axis, and the moments themselves would rotate out of the x-y plane, in the

y-z plane. However, not all materials are ideal.

Many magnetic materials are deposited in the form of thin films. The dimensions

of the material can have an effect on the structure of the domain wall. In very thin films,

the material may be considered a two-dimensional structure, breaking the symmetry of an

ideal system, and the symmetry found within a bulk material. If a Bloch wall existed in a

thin film, rotating the moments about the direction of the wall, rotation would result in

the creation of poles at the surface of the film. This would introduce a large energy

contribution from the dipolar interaction. The formation of these poles can be avoided if

the moments were to rotate about the z-axis, staying in the plane that contains the wall

and the direction of magnetization. A domain wall in which the moments rotate in this

manner is known as a Neel wall. Neel walls are generally formed in thin films and

multilayer materials.
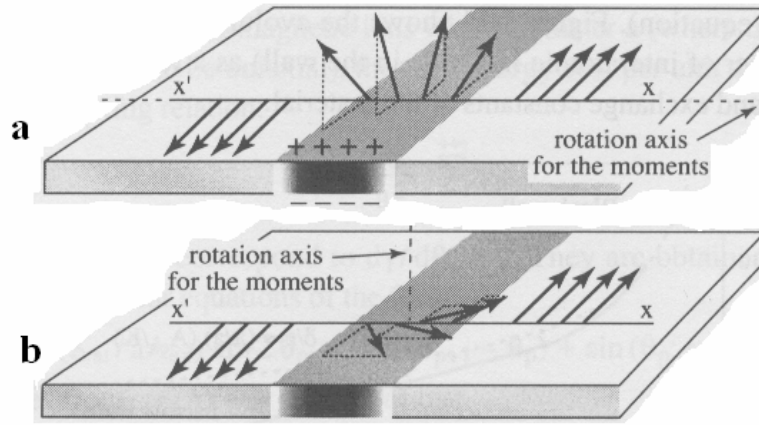
Figure 2.10
Magnetic moment rotation in: a) Bloch Wall; b) Neel Wall[1]

A derivation similar to the one done for the energy of a Bloch Wall has been done for a

Neel wall, giving an expression for the energy (σ_{nw})[33]:

$$\sigma_{nw} = 4\left[\frac{nJS^2}{a}\left(K + \frac{I_s^2}{2\mu_0}\right)\right]^{\frac{1}{2}} \tag{2.23}$$

where J, S,(a) and K are the same as in the derivation for the energy of a Bloch Wall,

Equation (2.21), and (n) is the number of atoms per unit cell. The term $\dfrac{I_s^2}{2\mu_0}$ is the

contribution from the stored magnetostatic energy present in a Neel Wall. Figure 2.11

illustrates the dependence of wall energy on film thickness for both Bloch and Neel

Walls.
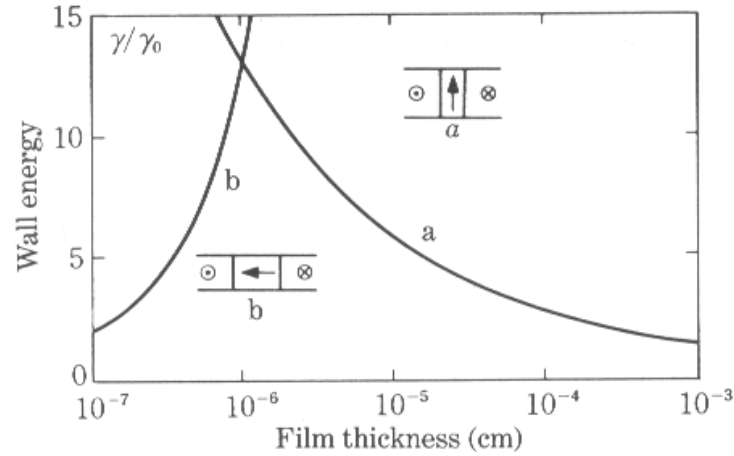
Figure 2.11
Domain wall energy vs. film thickness; a) Bloch Wall; b)Neel Wall[33]

It is clear from Figure 2.11 that a Neel Wall is preferred for thin and ultra-thin films,

whereas a Bloch Wall is preferred in thicker films and bulk materials. There appears to be

a critical thickness on the order of 10^{-6} cm under which the Neel Wall is energetically

favorable. The energy for a Neel Wall decreases with thickness, and the energy of a

Bloch Wall increases as thickness decreases. This is the result of the growing

magnetostatic energy contribution as the Bloch Wall forms poles on the surface of a thin

film.

2.2　Hysteresis and Magnetic Reversal

Exposure to an external magnetic field will cause the magnetic moments in a ferromagnetic material to align in the direction of the applied field. The magnetization versus external field (M vs. H) behavior of a material is the standard method for general magnetic characterization. Measuring the magnetization of a ferromagnetic material as afunction of applied external magnetic field, from positive to negative saturation, and back to positive saturation, results in a hysteresis loop, or hysteresis curve.

2.2.1　Hysteresis

The hysteresis curve provides salient information used to characterize a material. Most technological applications for ferromagnetic materials depend on the existence of a hysteresis loop. The figure below illustrates a typical hysteresis loop with several important values indicated:
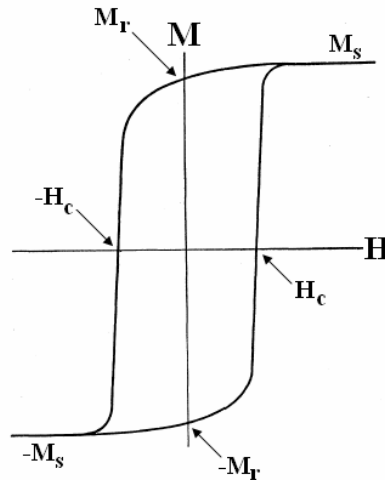
Figure 2.12
Typical hysteresis loop

The hysteresis loop above shows the nonlinear M vs. H behavior of a typical ferromagnetic material. If the material is subjected to a magnetic field (H) higher than that required to saturate the material, and then allowed to decrease toward the negative saturation, the M vs. H curve behaves as follows:

The material will be at positive saturation (M_s), meaning that it is at its maximum magnetization, and an increase in the magnetic field intensity can cause no greater magnetization because the magnetic moments of all the atoms are aligned with the external field.

As the field decreases, the magnetization will remain, even as the field goes to zero. The magnetization remaining at zero field is known as the remnance (M_r), in this case, the positive remenance. This value plays an important role in non-volatile magnetic memory devices.

As the field decreases toward negative saturation, there is a negative field where the material becomes demagnetized (M=0). This field value is the coercive field, or coercivity, in this case the negative coercivity ($-H_c$). As the field decreases further, the material will saturate in the negative direction.

From the negative saturation ($-M_s$) the field is increased to zero. Some negative magnetization remains even at zero field. The magnetization at H=0 for the ascending curve is the negative remenance ($-M_r$).

The field continues to ascend, and at some positive field, the material becomes demagnetized. This field value is the positive coercivity (H_c). The negative and positive

coercivity, as well as the negative and positive remnance and saturation fields should have the same absolute value. As the field continues to increase, it will again reach its positive saturation. This is one complete hysteresis loop, or cycle.

2.2.2   Magnetic Reversal Mechanisms

Hysteresis involves the magnetization of a material transitioning between its saturation states. This process of reversing polarity is known as magnetic reversal. There are several mechanisms by which this process can occur, but the two predominant methods are domain wall motion and reversal by rotation of magnetic moments. The type of reversal mechanism depends largely on the crystal structure of the material and the relative direction of the applied field with respect to the axes of the crystal.

Domain Wall Motion is the dominant reversal mechanism in a system where the external field is applied in the direction of an easy axis. As the magnitude of the external field is increased, the domain walls will displace themselves in a way that increases the size of the domains oriented in the direction of the field, at the expense of unfavorably oriented regions.
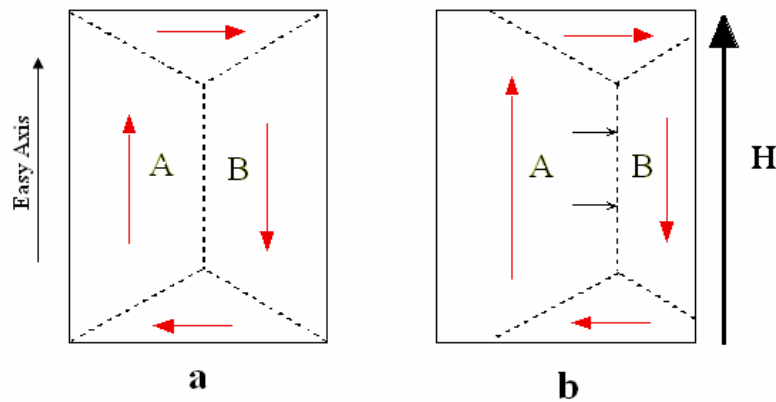
Figure 2.13
Magnetic domains: a) with no external field;
b) experiencing a field strong enough to move domain wall[2]

In an ideal crystal, the movement of the domain wall would be smooth and unrestricted, resulting in an instantaneous transition between saturation states. In a non-ideal system (i.e. reality), the domain wall will encounter various obstructions, generated by various factors. The nature of these defects range from stresses and strains caused by magnetostriction, to imperfections the crystal lattice, including impurities and dislocations. Consider a domain containing an impurity with no permanent magnetization. The domain would tend to magnetize the impurity, creating poles. As the domain wall intersects this impurity, closure domains form at the poles to decrease the magnetostatic energy[2]. Because this is a more favorable energy configuration, the domain wall is pinned at the impurity, and more energy (higher external field) is required to break the domain wall free and advance the movement.
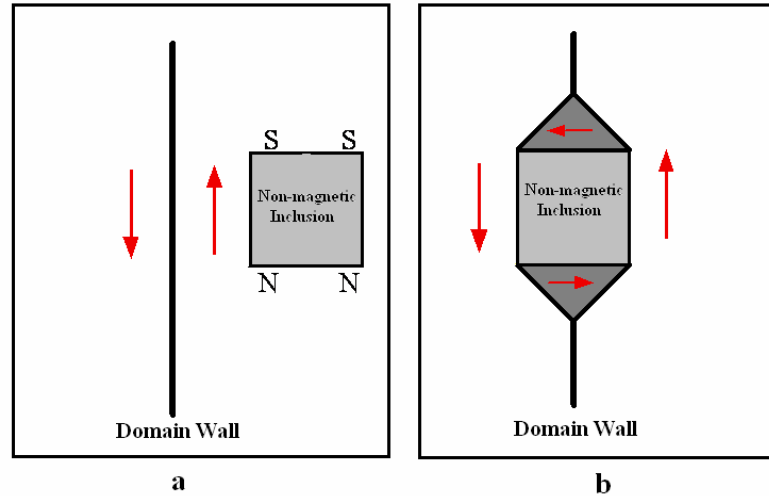
Figure 2.14
Domain wall: a) approaching inclusion; b) becoming pinned by inclusion[2]

Magnetization by rotation of magnetic moments is the method of reversal employed by systems in which the external field is applied in a direction away from the easy axis. Consider a material with a strong uniaxial anisotropy, where an external field is applied normal to the easy direction. The magnetization of the domains favors the easy direction, therefore neither of the domains will grow, because neither of them have a favorable magnetization. Instead, the torque experienced by the moments cause them to rotate away from the easy axis, in the direction of the external field. The magnetization of the moments evolves symmetrically, increasing the angle from the easy direction (θ) identically within each domain.
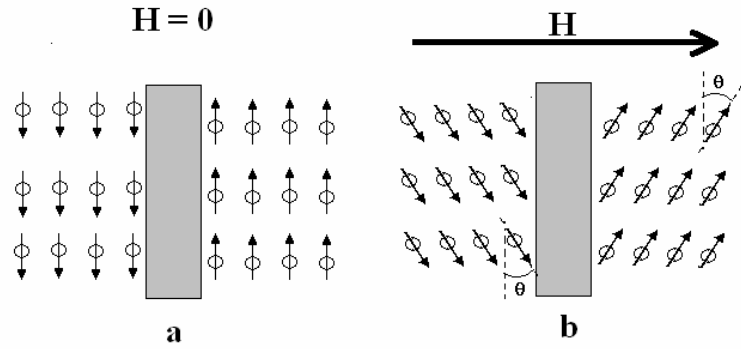
Figure 2.15
Two domains: a) no external field;
b) external field normal to easy axis

As the field intensity increases, the moments rotate farther from the easy direction until the material is saturated. Assuming the sample has no net magnetization prior to the application of the field, the macroscopic magnetization (M) at an angle (θ) can be given as:

$$M = M_s \sin(\theta) \tag{2.24}$$

If the external field is applied at an angle (φ), other than 0° or 90°, with respect to an easy axis, the magnetization is due to contributions from both domain wall displacement and rotation. As the field intensity is increased, the field component along the easy axis results in domain wall displacement. The displacement continues until the internal field along the easy axis is cancelled. The magnetization then turns to rotation, orienting the domains towards the direction of the field.

2.3 Magneto-Optical Effects

Classically, interactions between electric and magnetic fields are quantitatively correlated by Maxwell's equations[5]:

$$\nabla \cdot \mathbf{B} = 0 \tag{2.25}$$

$$\nabla \times \mathbf{E} = -\frac{\partial \mathbf{B}}{\partial t} \tag{2.26}$$

$$\nabla \times \mathbf{H} = \frac{\partial \mathbf{D}}{\partial t} + \mathbf{J} \tag{2.27}$$

$$\nabla \cdot \mathbf{D} = \rho \tag{2.28}$$

The equations involving the magnetic induction **B** (2.25 and 2.26) can be satisfied using a vector potential **A** and a scalar potential Φ by:

$$\mathbf{B} = \nabla \times \mathbf{A}$$
$$and$$
$$-\nabla \Phi = E + \frac{\partial \mathbf{A}}{\partial t} \tag{2.29}$$

Substituting these relations into Ampere's law (2.27) and using a vector identity:

$$\nabla \times (\nabla \times \mathbf{A}) = \nabla (\nabla \cdot \mathbf{A}) - \nabla^2 \mathbf{A} \tag{2.30}$$

yields a characteristic wave equation:

$$\nabla^2 \mathbf{A} - \varepsilon \mu \frac{\partial^2 \mathbf{A}}{\partial t^2} = -\mu \mathbf{J} + \varepsilon \mu \nabla \frac{\partial \Phi}{\partial t} + \nabla (\nabla \cdot \mathbf{A}) \tag{2.31}$$

A relationship between the charge density and potentials can be derived by substituting Eq. 2.29b into Coulomb's Law (2.28), which gives:

$$\nabla \cdot \mathbf{E} = \frac{1}{\varepsilon} \rho = -\nabla^2 \Phi - \varepsilon \mu \frac{\partial}{\partial t} (\nabla \cdot \mathbf{A}) \tag{2.32}$$

and since:

$$\nabla \cdot \mathbf{A} = 0 \tag{2.33}$$

Eq. 2.32 reduces to Poisson's equation:

$$\nabla^2 \Phi = -\frac{1}{\varepsilon} \rho \tag{2.34}$$

and a similar result can be derived for the vector potential from Eq. 2.27:

$$\nabla^2 \mathbf{A} = -\mu \mathbf{J} \tag{2.35}$$

relating the vector potential $\mathbf{A}$ to the current density $\mathbf{J}$.

Maxwell's equations can be supplemented by the material equations that quantify specific material properties like conductivity (σ), dielectric permativity (ε), and magnetic permeability (μ).

$$\mathbf{D} = \hat{\varepsilon} \cdot \mathbf{E} = \varepsilon \mathbf{E} + \mathbf{P} \tag{2.36}$$

$$\mathbf{H} = \hat{\mu} \cdot \mathbf{H} = \frac{1}{\mu} \mathbf{B} + \mathbf{M} \tag{2.37}$$

$$\mathbf{J} = \hat{\sigma} \cdot \mathbf{E} \tag{2.38}$$

where it is implied that the permittivity and permeability of free space are unity. The dielectric permeability (ε) and the optical conductivity (σ) are complex quantities given by:

$$\hat{\varepsilon} = \varepsilon_1 + i\frac{\sigma_1}{\omega} = \varepsilon_1 + i\varepsilon_2 \tag{2.39}$$

$$\hat{\sigma} = \sigma_1 + i\sigma_2 \tag{2.40}$$

The complex permittivity and optical conductivity are related through:

$$\hat{\varepsilon} = 1 + \frac{i}{\omega}\hat{\sigma} \qquad (2.41)$$

In general, what is sometimes referred to as the dielectric constant is in fact not a

constant, but a function depending on spatial and time variables. Taking this into account,

the displacement field, D(r,t), is related to the Electric field, E(r',t') by:

$$\mathbf{D}(\mathbf{r},t) = \int\int_{-\infty}^{t} \hat{\varepsilon}(\mathbf{r},\mathbf{r}',t')\mathbf{E}(\mathbf{r}',t')dt'd\mathbf{r}' \qquad (2.42)$$

Other similar equations can be derived for the conductivity and magnetic permeability,

and can even be dependent on the applied field strength. The results are material

quantities taking the form of tensors, rather than constants.

In addition to material properties, Maxwell's equations can directly generate wave

equations governing the propagation of EM waves through a medium. This is the

classical basis for optical properties of solids where the wave aspect of light is the

significant attribute. Given an electrically neutral medium and neglecting boundary and

edge effects, the electric and magnetic fields of the waves in a medium follow:

$$\mathbf{E}(\mathbf{r},t) = \mathbf{E}_0 e^{i(\mathbf{k}\cdot\mathbf{r}-\omega t)} \qquad (2.43)$$

$$H(\mathbf{r},t) = H_0 e^{i(\mathbf{k}\cdot\mathbf{r}-\omega t-\phi)} \qquad (2.44)$$

where $\mathbf{k}$ is the wave vector and ϕ accounts for the phase difference that may exist

between the electric and magnetic fields. Applying the vector identity (Eq.2.30) to

equations (2.26) and (2.28), allows the electric and magnetic components to be separated

to obtain:

$$\frac{\partial}{\partial t}(\nabla \times \mathbf{B}) = \nabla^2 \mathbf{E} - \nabla\left(\frac{\rho_{ext}}{\varepsilon_1}\right) \tag{2.45}$$

and substituting the three material equations into Ampere's Law gives:

$$\nabla \times \mathbf{B} = \varepsilon_1 \mu_1 \frac{\partial \mathbf{E}}{\partial t} + \mu_1 \sigma_1 \mathbf{E} \tag{2.46}$$

combining this with equation (2.45) leads to the wave equation for the electric field:

$$\nabla^2 \mathbf{E} - \varepsilon_1 \mu_1 \frac{\partial^2 \mathbf{E}}{\partial t^2} + \mu_1 \sigma_1 \frac{\partial \mathbf{E}}{\partial t} = 0 \tag{2.47}$$

and the magnetic field:

$$\nabla^2 \mathbf{H} - \varepsilon_1 \mu_1 \frac{\partial^2 \mathbf{H}}{\partial t^2} + \mu_1 \sigma_1 \frac{\partial \mathbf{H}}{\partial t} = 0 \tag{2.48}$$

assuming there is no significant electrical loss ($\sigma_1 = 0$) the wave equations reduce to their more familiar forms:

$$\nabla^2 \mathbf{E} - \varepsilon_1 \mu_1 \frac{\partial^2 \mathbf{E}}{\partial t^2} = 0 \tag{2.49}$$

$$\nabla^2 \mathbf{H} - \varepsilon_1 \mu_1 \frac{\partial^2 \mathbf{H}}{\partial t^2} = 0 \tag{2.50}$$

This shows that the magnitude of $\mathbf{E}$ and $\mathbf{H}$ do not change in the medium, but the velocity does decrease by a factor of $(\varepsilon_1 \mu_1)^{1/2}$ when compared to vacuum propagation.

Now that the equations governing the propagation of light in a medium have been introduced, the effects of a magnetized medium can be discussed. Such effects are appropriately referred to as magneto-optical effects. For magnetically ordered materials, the effects are present even in the absence of an external field. Magneto-optical effects occur in many forms, but essentially all are direct consequences of the splitting of atomic

energy levels in a magnetic field, formally called the Zeeman Effect. The magneto optical

effects of relevance for this work originate from optical anisotropy on a magnetized

medium that shows up in light reflected at oblique incidence from the surface of the

magnetized material, referred to as the magneto-optical Kerr effects. These effects were

first observed in 1888 by Scottish physicist John Kerr[1]. Kerr noticed that when plane

polarized light was reflected from the pole of an electromagnet, it became elliptically

polarized with the major axis of the ellipse rotated with respect to the incident plane of

polarization. If the incident light is either s- or p- polarized, the electric fields are oriented

perpendicular (s) or parallel (p) to the plane of incidence and the magneto-optical effects

are dependant on which polarization is present. In addition to the polarization, the

specific Kerr effect observed depends on the direction of magnetization relative to the

plane of incidence. If the magnetization vector (**M**) is perpendicular to the surface of

reflection, the polar Kerr effect is observed; if the magnetization (**M**) lies in the plane

parallel to the surface and the plane of incidence, the longitudinal Kerr effect is observed.

Finally if the magnetization lies in the surface plane, but is perpendicular to the plane of

incidence, the transverse Kerr effect is observed. The Figure 2.16 gives an illustration to

distinguish between the three Kerr effects:
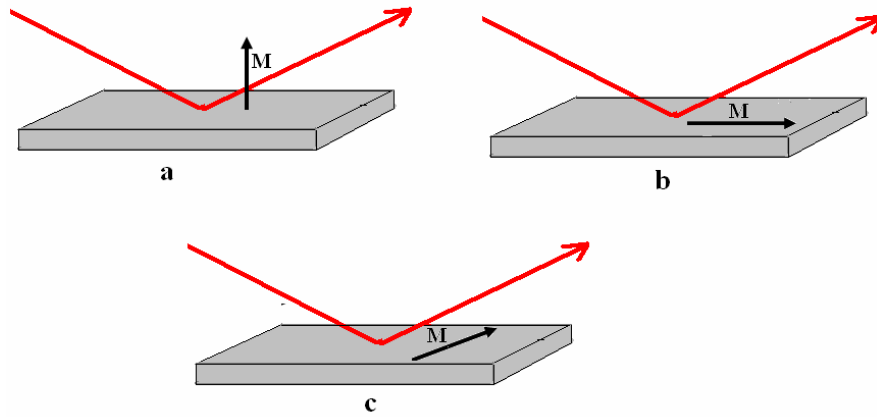
Figure 2.16
Kerr Effects: a) polar; b) longitudinal; c) transverse

Each effect is quantitatively explained below. They are treated separately because the effects vary depending on the geometry and direction of the magnetization.

2.3.1   Polar Kerr Effect

As mentioned above, the polar Kerr effect occurs when the plane of incident light and magnetization are arranged as in Figure 2.16a. This is the effect of great importance for MO data storage, and results in the largest magnitude of polarization change after reflection. If the plane of incidence is taken to be the x-y plane then, for the polar Kerr effect, the dielectric tensor (ε) is composed of the diagonal elements ε_{xx} and ε_{zz} and the off diagonal element ε_{xy}, resulting in:

$$\hat{\varepsilon} = \begin{pmatrix} \varepsilon_{xx} & \varepsilon_{xy} & 0 \\ -\varepsilon_{xy} & \varepsilon_{xx} & 0 \\ 0 & 0 & \varepsilon_{zz} \end{pmatrix} \tag{2.51}$$

the elements ε_{ij} are comprised of the complex parts: $\varepsilon_{ij} = \varepsilon_{ij}^{(1)} + i\varepsilon_{ij}^{(2)}$ where

i,j = x,y,z and $\varepsilon_{xx} = (n+ik)^2$, where (n) is the refractive index and (k) is the extinction coefficient. The dielectric tensor is again related to the optical conductivity tensor, $\sigma_{ij} = \sigma_{ij}^{(1)} + i\sigma_{ij}^{(2)}$ by:

$$\hat{\varepsilon}_{ij}(\omega) = \delta_{ij} + \frac{i}{\omega}\hat{\sigma}_{ij}(\omega) \tag{2.52}$$

The four non-zero elements of the dielectric tensor can be used to obtain and fully quantify the Polar Kerr effect. This can also be done using the complex refractive index N(ω).

$$\hat{N}(\omega) = \sqrt{\hat{\varepsilon}(\omega)} = n(\omega) + ik(\omega) \tag{2.53}$$

Solutions to Maxwell's equations yield the normal modes that correspond to the propagation of pure polarization states along specific directions in the sample[6] i.e. circularly polarized states. For normal incidence the complex Kerr angle and the dielectric tensor components are related by:

$$\frac{1 + \tan \eta}{1 - \tan \eta} e^{i2\theta} = \frac{1 + \hat{N}_+}{1 - \hat{N}_+}\frac{1 - \hat{N}_-}{1 + \hat{N}_-} \tag{2.54}$$

where

$$\hat{N}_\pm = (\varepsilon_{xx} \pm i\varepsilon_{xy})^{\frac{1}{2}} \tag{2.55}$$

In Equation (2.54), η and θ are the Kerr rotation and Kerr ellipticity respectively. It is clear that the maximum Kerr rotation (θ) is +/- 90°, and the maximum ellipticity (η) is +/- 45°. In reality, the Kerr rotation and ellipticity for most materials is generally less than 1°.

For such small θ and η, and in cases where the magnitude of ε_{xy} is much less than ε_{xx}, the above expression can be accurately approximated by the simplified expression:

$$\theta + i\eta \approx \frac{-\varepsilon_{xy}}{(\varepsilon_{xx} - 1)\sqrt{\varepsilon_{xx}}} \tag{2.56}$$

2.3.2   Longitudinal Kerr Effect

The Longitudinal Kerr Effect is present for incidence and magnetization similar to Figure 2.16b. If the y-axis is chosen to be parallel to both the plane of incidence and the magnetization vector (M), the dielectric tensor is of the form:

$$\hat{\varepsilon} = \begin{pmatrix} \varepsilon_{xx} & 0 & \varepsilon_{xz} \\ 0 & \varepsilon_{xx} & 0 \\ -\varepsilon_{xx} & 0 & \varepsilon_{zz} \end{pmatrix} \tag{2.57}$$

The complex Kerr angle for this situation can be given by:

$$\theta_{s,p}^{L} + i\eta_{s,p}^{L} = -\frac{2\varepsilon_{xx}\sin\varphi\cos\varphi\sqrt{\varepsilon_{xx}}}{D} \tag{2.58}$$

where D is given by[6]:

$$D = \left(\sqrt{(\varepsilon_{xx}(\varepsilon_{zz} - \sin^2\varphi)} + \sqrt{(\varepsilon_{zz}(\varepsilon_{xx} - \sin^2\varphi)}\right) \times \left(\sqrt{\varepsilon_{xx} - \sin^2\varphi} \pm \cos\varphi\right)$$
$$\left(\sqrt{\varepsilon_{xx}\varepsilon_{zz}}\cos\varphi \mp \sqrt{\varepsilon_{zz} - \sin^2\varphi}\right)$$

where (φ) is the angle of incidence and the plus and minus signs correspond to the p- and s- polarized incident light respectively. If ε_{xx} and ε_{zz} are approximately equal, as in an optically isotropic material, Eq. 2.58 simplifies to:

$$\theta_{s,p}^{L} + i\eta_{s,p}^{L} = -\frac{2\varepsilon_{xz}\sin\varphi(\sqrt{\varepsilon_{xx}-\sin^2\varphi} \pm \sin\varphi\tan\varphi)}{(\varepsilon_{xx}-1)(\varepsilon_{xx}-\tan^2\varphi)\sqrt{\varepsilon_{xx}-\sin^2\varphi}}$$

(2.59)

2.3.3 Transverse Kerr Effect

The geometry of the transverse Kerr effect is illustrated in Figure 2.14c, and is unique in that it does not measure a Kerr angle or ellipticity, but rather a modulated difference in intensity of the reflected light. This arises from the fact that an MO effect exists for only a p-polarized incident wave, meaning that the transverse Kerr effect can be measured without a polarizer. The transverse Kerr effect will occur by choosing the plane of incidence where the wave vector is in the y-z plane and a magnetization in the +/- x direction. It has been shown[6] that the total reflectivity difference (δ_K) for the two magnetization directions can be given by:

$$\delta_K = \mathrm{Re}\left[\frac{2\varepsilon_0\varepsilon_{xz}\sin 2\varphi}{\varepsilon_{xx}^2\cos^2\varphi - \varepsilon_0\varepsilon_{xx} + \varepsilon_0^2\sin^2\varphi}\right]$$

(2.60)

When compared to the polar and longitudinal Kerr effects, the transverse effect is less frequently used in spectroscopic applications, but is useful in analyzing surface structures[6].

2.4   Magnetoelasticity

Magnetoelasticity is the coupling of the magnetization of a magnetic material and its elastic properties. This phenomena exists in two general forms, the inverse magnetoelastic effect and the direct magnetoelastic effect – magnetostriction. Inverse magnetoelastic effects involve the alteration of the magnetic properties of a material when it experiences an external stress. The figure below shows the effect of external isotropic stress on the hysteresis curve of a NiFe film.
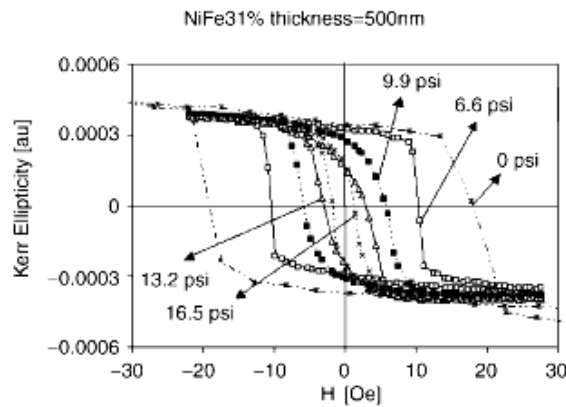
Figure 2.17
Effects of external isotropic stress on magnetic properties of NiFe film[7]

More information of the effects of external stress on the magnetic properties of NiFe films, can be found in several of the sources cited[7,8]. The magnetoelastic effects addressed herein are limited to magnetostriction.

2.4.1   Magnetostriction Theory

Magnetostriction is considered the direct magnetoelastic effect, an elastic response to an applied external magnetic field. There are many mathematical models used to derive the formalisms used in modern magnetostriction theory. This section will concentrate on formulating a suitable description for magnetostriction with the purpose of

quantifying the phenomena of magnetostriction in a ferromagnetic thin film. Magnetoelastic coupling is the tendency of atoms to shift their position in response to the rotation of magnetic moments resulting in an anisotropic strain induced along the direction of magnetization in the material experiencing the magnetization. The result of the change in position of the atoms is a relative change in length in the direction of magnetization, giving rise to magnetostriction (λ), formally defined by:

$$\lambda = \frac{\Delta l}{l} \tag{2.61}$$

2.4.2   Mathematical Formulation of Magnetostriction

Magnetostriction is primarily due to the anisotropy energy associated with the spin-orbit coupling between atoms. Because the anisotropy energy varies with strain, a lattice may sometimes spontaneously strain if it provides a favorable lower-energy equilibrium state. This phenomenon can be introduced by first considering the anisotropy energy of a non-strained ideal material with cubic anisotropy expressed by:

$$E_{an} = K(\alpha_1^2\alpha_2^2 + \alpha_2^2\alpha_3^2 + \alpha_3^2\alpha_1^2) \tag{2.62}$$

where K is the anisotropy constant, and the α's are the direction cosines of the magnetization in reference with the crystal lattice such that:

$$\alpha_1^2 + \alpha_2^2 + \alpha_3^2 = 1 \tag{2.63}$$

As previously mentioned, the strain must be included to yield an accurate interpretation of the strain dependent anisotropy energy. This can be done by first expanding Eq. (2.62) in a Taylor series. A reasonably accurate interpretation can be gathered by keeping only the first two terms in the expansion:

$$E_{an} = (E_{an})_0 + \sum_{i \geq j} \left(\frac{\partial E_{an}}{\partial \varepsilon_{ij}} \right)_0 \varepsilon_{ij} \tag{2.64}$$

In the above equation, $(E_{an})_0$ is the energy of the original undisturbed lattice, and the ε's are the symmetric components of the strain tensor, not to be confused with the dielectric tensor previously used to derive the Kerr effects. Since the anisotropy energy has now been quantified, it is appropriate to formulate an expression for the total crystal energy involving the anisotropy energy, elastic energy, and the magnetostrictive energy:

$$E = K(\alpha_1^2 \alpha_2^2 + \alpha_2^2 \alpha_3^2 + \alpha_3^2 \alpha_1^2) + B_1(\alpha_1^2 \varepsilon_{xx} + \alpha_2^2 \varepsilon_{yy} + \alpha_3^2 \varepsilon_{zz}) + B_2(\alpha_1 \alpha_2 \varepsilon_{xy} + \alpha_2 \alpha_3 \varepsilon_{yz} + \alpha_3 \alpha_1 \varepsilon_{zx})$$
$$+ \frac{1}{2} c_{11}(\varepsilon_{xx}^2 + \varepsilon_{yy}^2 + \varepsilon_{zz}^2) + \frac{1}{2} c_{44}(\varepsilon_{xy}^2 + \varepsilon_{yz}^2 + \varepsilon_{zx}^2) + c_{12}(\varepsilon_{yy} \varepsilon_{zz} + \varepsilon_{xx} \varepsilon_{zz} + \varepsilon_{xx} \varepsilon_{yy})$$

$$\tag{2.65}$$

where the c's in Eq.(2.64) are the elastic constants given in Voigt's notation, and the B's are the magnetoelastic coupling constants. A more comprehensive introduction on Voigt's notation and magnetoelastic coupling constants is given in [Etienne du Tremolet de Lacheisserie][1, 9].

To find equilibrium, the minimum energy must be found by taking $\frac{\partial E}{\partial \varepsilon_{ij}} = 0$ for all ε_{ij}, where the results are:

$$\frac{\partial E}{\partial \varepsilon_{xx}} = c_{11}\varepsilon_{xx} + c_{12}(\varepsilon_{yy} + \varepsilon_{zz}) + B_1\alpha_1^2 = 0$$

$$\frac{\partial E}{\partial \varepsilon_{yy}} = c_{11}\varepsilon_{yy} + c_{12}(\varepsilon_{zz} + \varepsilon_{xx}) + B_1\alpha_2^2 = 0$$

$$\frac{\partial E}{\partial \varepsilon_{zz}} = c_{11}\varepsilon_{zz} + c_{12}(\varepsilon_{xx} + \varepsilon_{yy}) + B_1\alpha_3^2 = 0$$

$$\frac{\partial E}{\partial \varepsilon_{xy}} = 4c_{44}\varepsilon_{xy} + B_2\alpha_1\alpha_2 = 0 \qquad\qquad (2.66)$$

$$\frac{\partial E}{\partial \varepsilon_{xz}} = 4c_{44}\varepsilon_{xz} + B_2\alpha_1\alpha_3 = 0$$

$$\frac{\partial E}{\partial \varepsilon_{yz}} = 4c_{44}\varepsilon_{yz} + B_2\alpha_2\alpha_3 = 0$$

and the solutions for stable equilibrium are:

$$\varepsilon_{ii} = B_1\left[c_{12} - \alpha_i^2(c_{11} + 2c_{12})\right] \qquad\qquad (2.67)$$

and

$$\varepsilon_{ij} = -\frac{B_2\alpha_i\alpha_j}{c_{44}} \qquad \text{for } i \neq j \qquad\qquad (2.68)$$

To formally express the magnetostriction, an equation relating the strain tensor elements to the change in length (δl) is needed. This relationship can be expressed by:

$$\frac{\delta l}{l} = \sum \varepsilon_{ij} \beta_l \beta_k \tag{2.69}$$

where β is a vector in the direction along which the change in length is measured, and

k,l = 1,2,3; x = 1, y = 2 and z = 3.

Inserting equations (2.66 and 2.67) into equation 2.68 yields an equation linking the magnetostriction, direction of δl, and the crystal constants:

$$\lambda = \frac{\delta l}{l} = -\frac{B_1}{c_{11} - c_{12}} \left[\alpha_1^2 \beta_1^2 + \alpha_2^2 \beta_2^2 + \alpha_3^2 \beta_3^2 \right] - \frac{B_2}{c_{44}} \left[\alpha_1 \alpha_2 \beta_1 \beta_2 + \alpha_2 \alpha_3 \beta_2 \beta_3 + \alpha_3 \alpha_1 \beta_3 \beta_1 \right]$$
$$+ \frac{3 c_{12} B_1}{(c_{11} - c_{12})(c_{11} + 2 c_{12})}$$

$$\tag{2.70}$$

Referring back to minimizing the anisotropy energy (equation 2.63), a direct treatment of minimizing the expression by taking the derivatives is arduous and unnecessary. Minimizing the energy and arriving at an expression for an equilibrium state with a strain can be reached by recognizing that the form of the desired expression should be:

$$E_{an} = (K_0 + \Delta K)(\alpha_1^2 \alpha_2^2 + \alpha_2^2 \alpha_3^2 + \alpha_3^2 \alpha_1^2) \tag{2.71}$$

In the above equation, ΔK is independent of the direction cosines, but is related to the elastic modules and the magnetic coupling constants. One way to arrive at an expression similar to equation (2.70) is to introduce magnetostriction constants, λ_{100} and λ_{111} in the [100] and [111] crystallographic directions, respectively. The constants are equal to[4]:

$$\lambda_{100} = -\frac{2}{3} \frac{B_1}{c_{11} - c_{12}} \tag{2.72}$$

and

$$\lambda_{111} = -\frac{1}{3}\frac{B_2}{c_{44}} \tag{2.73}$$

In terms of the magnetostriction constants, ΔK can be expressed as:

$$\Delta K = \frac{9}{4}\left[(c_{11} - c_{12})\lambda^2_{100} - 2c_{44}\lambda^2_{111}\right] \tag{2.74}$$

If the material is indeed isotropic, then $\lambda_{100} = \lambda_{111} = \lambda$, and equations (2.71 and 2.71) can be written as:

$$B_2(c_{11} - c_{12}) = 2B_1c_{44} \tag{2.75}$$

Using these new expressions, equation (2.69) can be simplified to:

$$\frac{\delta l}{l} = \frac{3}{2}\lambda\left[(\alpha_1\beta_1 + \alpha_2\beta_2 + \alpha_3\beta_3)^2 - \frac{1}{3}\right] \tag{2.76}$$

Finally, by defining $\cos\theta = \alpha_1\beta_1 + \alpha_2\beta_2 + \alpha_3\beta_3$, where θ is the angle between the direction of magnetization and the direction along which δl is measured, a final expression for $\delta l/l$ in terms of θ and the saturation magnetostriction λ_s can be given by[9]:

$$\frac{\delta l}{l} = \frac{3}{2}\lambda_s\left[\cos^2\theta - \frac{1}{3}\right] \tag{2.77}$$

It is important to point out that this expression describes the saturation magnetostriction of an isotropic material. This is evident from the lack of a crystallographic reference in the equation. This expression is not particularly useful for describing the magnetostriction of most magnetic specimens, as they are generally not isotropic. However, it can be applied to individual domains, and using averaging methods, it can be employed to derive an approximation for the saturation magnetostriction of specimens at random angles, and is suitable for use in the applied measurement technique[10].

CHAPTER 3

FABRICATION AND CHARACTERIZATION OF SAMPLES

The samples studied originated from two different sources. The specifics of the fabrication processes and physical characteristics for both types of samples are discussed in this chapter. Only samples that underwent characterization are presented here, details for all samples can be found in Appendix A.

3.1 NiFe Samples

The NiFe samples were fabricated by Claude Garrett in 2001 as part of his thesis work. Several variations of NiFe films were produced, all by DC magnetron sputtering. Some samples were deposited on silicon substrates, while others were deposited on glass substrates. Only films deposited on silicon were used for the research in this thesis, therefore the glass-substrate samples will be neglected. Two types of silicon substrates were used: 1-inch p-type <100> substrates with ρ = 1-20 Ω.cm, and large pieces cut from a 4-inch p-type <100> wafer with ρ = 1-20 Ω.cm. In addition to differing substrates, films with different iron concentrations were sputtered from NiFe35% and NiFe45% targets. Before sputtering the samples were heated to 350°C to remove contaminants. Deposition was done below 50°C. The working gas used was Ar, introduced to a background pressure of $8x10^{-7}$ torr with a sputtering power of 70 Watts[11]. Varying film thicknesses were produced by altering the sputter times. Subsequent to sputtering, the film thickness and thus the sputter rates were estimated using the vibrating sample

magnetometer (VSM - See Chapter 4.1). The film thicknesses were estimated using the

known saturation magnetization per unit volume of the given film composition (M_s/V),

the magnetic saturation measured via the VSM (M_{vsm}), and the surface area (A) of the

sample; the thickness (t) of the film can be estimated by:

$$t = \frac{M_{vsm}V}{M_s A}$$

the calculations made for thicknesses of the various films are given below:

Sample ID	Sputter Time	Composition	M (emu)	H (Oe)	Estimated Thickness (nm)
102701-01	16:30	NiFe-45%	17.48×10^{-2}	2.26	288.3
102701-04	21:00	NiFe-45%	24.10×10^{-2}	1.26	397.5
102701-03	31:00	NiFe-45%	35.01×10^{-2}	1.32	577.5
102701-02	46:00	NiFe-45%	48.74×10^{-2}	4.14	803.4

Sample ID	Sputter Time (min:sec)	Film Thickness
101601-02	12:31	225.3 nm
101901-01	29:00	522 nm
101901-03	5:33	99.9 nm
101701-03	7:30	135 nm
101901-02	5:33	100 nm
101701-04	7:30	135 nm

Table 3.1
NiFe sample characteristics[11]

3.2   TbFe/FeCo Multilayers

TbFe/FeCo multilayers were acquired from Southwest Research Institute (SWRI) in San Antonio, Texas. Two sets of samples were acquired; one set was obtained in the spring of 2005, the other in the summer of the same year. SWRI was seeking assistance in magnetic/magnetoelastic characterization of the samples with the premise of finding an application specific material with a large magnetic saturation (M_s) and a large magnetostriction (λ)/saturation field (H_s) ratio. FeCo has a large saturation magnetization, a small magnetostriction, and a negligible anisotropy, whereas TbFe has a large magnetostriction but relatively low saturation magnetization[16]; measurement results show that M_s(FeCo) is approximately $5M_s$(TbFe). Theory suggests that combining both materials in a multilayer would result in a material with a magnetostriction two times lower and a saturation field 6 times lower, assuming that the TbFe layer thickness and the FeCo layer thickness in the ML is equal[18]. Since the maximum applicable field in applications is always limited, the ideal material should have a large magnetostriction (λ)/Hs ratio.

Although the samples were deposited at SWRI facilities, the deposition specifics (i.e. sputtering parameters, layer thicknesses, number of layers, etc.) were acquired and information for relevant samples is provided in the Table 3.2.

ID#	Repeat#	Fe-Co Thickness sec(nm)	TbFe Thickness sec(nm)	Total Thickness (kA)
40205(#1)	160x	9(11)	4(5)	26.3/27.8
33105(#1)	320x	5(5)	3(3)	30.7/34.4
32805(#1)	160x	9(11)	4(5)	3.21
32805(#2)				22.5
32205(#2)	160x	8(9)	4(4)	2.93
32105(#2)	160x	10(11)	5(5)	11.1
32105(#1)	160x	10(11)	5(5)	24.7
31805	50x *	10(11)	5(5)	8.88
31705(#2)	160x	8(9)	7(7)	27.36
31705(#1)	160x	9(9)	9(7)	25.8
52405(#2)	175X	10(7)	13(10)	N/A
60605(#1)	150X	20(10)	9(10)	1.5 um (TbFe)
60605(#2)	235X	20(10)	6(7)	1.645 um (TbFe)

Table 3.2
Sputtering results for selected TbFe/FeCo multilayers

CHAPTER 4

MAGNETIC CHARACTERIZATION EQUIPMENT

4.1   Vibrating Sample Magnetometer (VSM)

The vibrating sample magnetometer (VSM) generates hysteresis loops based on the principles of magnetic induction. In a VSM, a sample is attached to a vibrating rod and allowed to vibrate in a magnetic field produced by electromagnets. As the magnetization of the sample increases due to the increasing magnitude of the field, the change in flux induces an EMF resulting in a voltage signal measured by induction coils located near the sample (see Fig. 4.15). The signal is usually small, and is measured by a lock-in amplifier at a frequency specified by the signal from the sample vibrator.
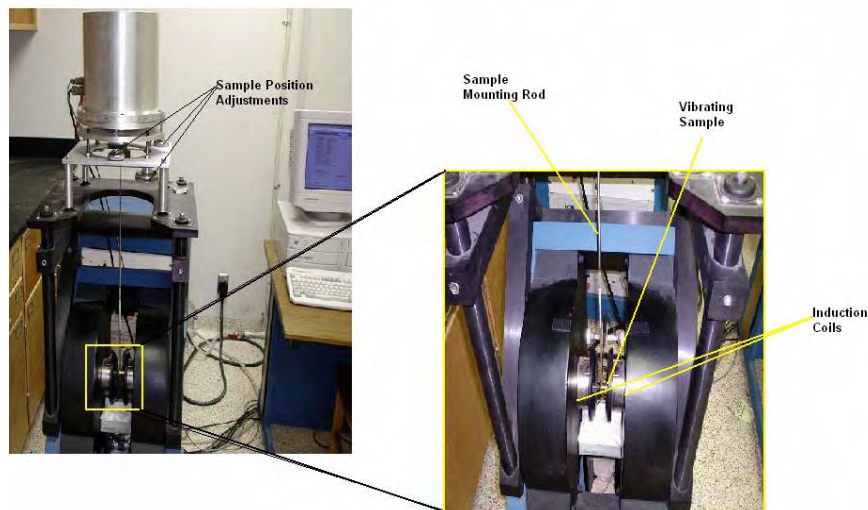
Figure 4.1 – Photo of VSM

The signal measured by the induction coils is directly proportional to the magnetization of the sample, and independent of the external field intensity. Plotting the induction vs. magnetic field intensity (H) results in a hysteresis curve representative of the magnetization vs. field behavior of the sample. The VSM is generally considered a reliable and accurate method for obtaining hysteresis measurements on materials with a sizable magnetic moment, although it can lack adequate sensitivity on ultra thin films or samples with only small amounts of magnetic material. The measurements in this report were done with a LDJ Electronics 6140 VSM. The model used has a sensitivity of .001 emu, and a maximum applicable field range of 10000 Oe (-5000 to 5000 Oe). All measurements were done at room temperature, and no corrections were made for the signal originating from the sample holder.

4.2   Kerr Tracer

4.2.1   Theory of Operation

Hysteresis curves were also obtained for several samples using the Kerr Tracer. The Kerr Tracer measurement system is essentially a modulated ellipsometer that measures the longitudinal Kerr effects occurring as a magnetic sample is magnetized. Ellipsometry is a method of characterizing materials based on changes in polarization upon reflection from or transmission through the material. As discussed in chapter 2, reflection from the surface of a magnetic material causes linearly polarized incident light to become elliptically polarized with its major and minor axes rotated with respect to the orientation of the incident beam.
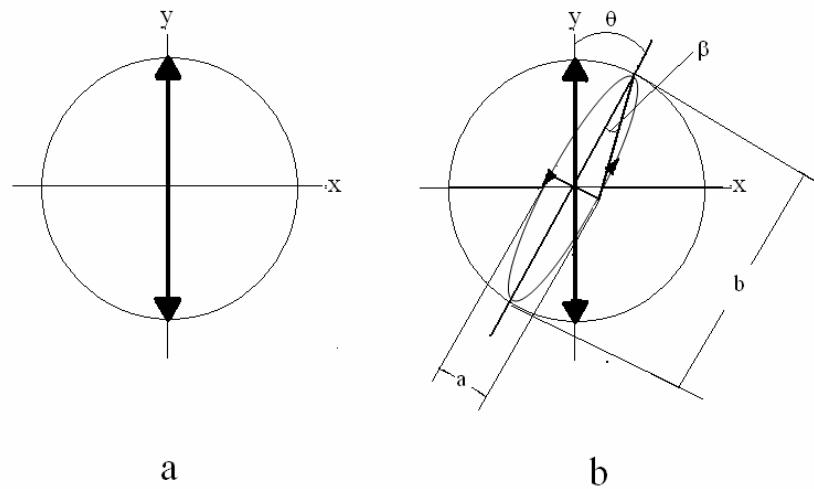
Figure 4.2
Schematic representation of: a) linearly polarized incident beam and;
b) elliptically polarized reflected beam

One measurable feature of the reflected light is the rotation of the major axis from the incident linear orientation, called the Kerr rotation, denoted θ_k, or θ as shown in Fig 4.2b.

The absolute magnitude of the Kerr rotation is dependent on the material, but its relative

magnitude is directly proportional to the magnetization of the material. In addition to the

Kerr rotation, another measurable quantity is the Kerr ellipticity, ε_k, defined as:

$$\varepsilon_k = \frac{a}{b} = \tan \beta \approx \beta \qquad (4.1)$$

where a, b, and β are defined in Fig 4.2b. The ellipticity is the ratio of major and minor

axes of the ellipse, and is directly proportional to the magnetization. The Kerr Tracer can

measure both the Kerr rotation and Kerr ellipticity by modulating the polarization of the

reflected beam using a Photoelastic Modulator (PEM) developed and manufactured by

Hinds Instruments[12]. A Photoelastic Modulator is a transparent bar of fused silica

connected to a piezoelectric crystal set to vibrate at a fixed frequency. The vibration of

the piezoelectric crystal induces birefringence in the fused silica by manipulating the

distance between the crystallographic planes within the fused silica bar.
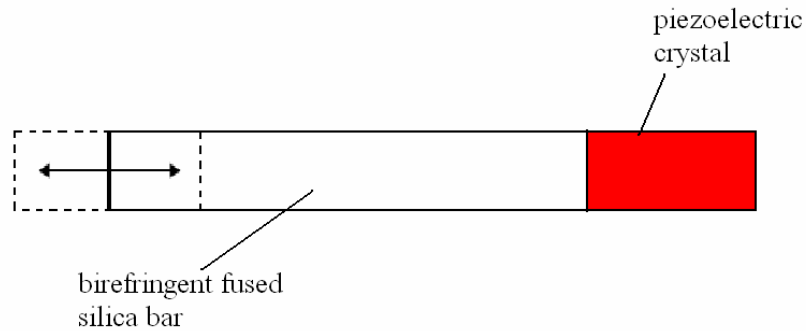
Figure 4.3
Schematic of photoelastic modulator

The birefringence causes the light passing through the crystal to travel at different speeds

depending on the direction of polarization. The increase or decrease in speed is dependent

on the state of the fused silica bar. When the bar is relaxed, the beam passes through the

bar unmodulated, because there is no birefringence induced. When the bar is

compressed, the y-component of the polarization is unaffected, but the x-component is slowed down and emerges from the PEM lagging behind the y-component resulting in an induced phase shift between the x- and y-components. Conversely, when the bar is stretched the beam leaves the PEM with the x-component leading the y-component which is still unaffected, again causing a phase shift between the components, but in the opposite direction. The modulated phase shift between the polarization components is called the retardation. The magnitude of the retardation and the frequency of modulation can be adjusted on the PEM control box. For the current Kerr Tracer setup, the retardation is set to 2.4 radians, and the frequency is 50 kHz. The choice of these settings will be discussed shortly.

The figure below schematically shows the waveform of the beam leaving the PEM for different states of the fused silica bar.
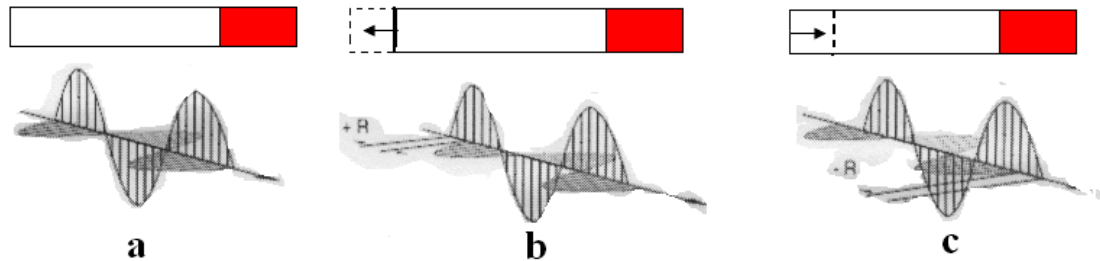
Figure 4.4
Waveform emerging from PEM: a) relaxed; b) stretched; c) compressed

Since the light emerging from the PEM is modulated, placing an analyzer at an angle of 45° with respect to the incident polarization direction will allow only the component of polarization along the 45° axis to pass through, resulting in modulated intensity fluctuations at the photodetector. The photodetector converts the photonic intensities into

voltages; a DC voltage for the continuous beam reaching the detector, and an AC voltage generated by the intensity fluctuations caused by the PEM and analyzer. For the polar Kerr configuration, the intensity of the laser light (I) that reaches the detector can be expressed by:

$$I = [R + \frac{\Delta R}{2}\sin\delta + R\cos\delta\sin(\Delta\theta + 2\varphi)]I_0 \tag{4.2}$$

where R is the reflection of the sample, equal to:

$$R = \frac{1}{2}(r_+^2 + r_-^2) \tag{4.3}$$

and ΔR is:

$$\Delta R = r_+^2 - r_-^2 \tag{4.4}$$

and

$$\Delta\theta = \theta_+ - \theta_- \tag{4.5}$$

The variables r and θ are related to the Fresnel coefficients (F) of circularly polarized light by the equation:

$$F^{\pm} = r_{\pm}e^{i\theta_{\pm}} \tag{4.6}$$

Where +/- denote right circular and left circular polarization respectively.

The retardation of the modulator is denoted δ, and I_0 is the intensity of the incident beam.

The retardation (δ) of the PEM is a function of time, varying as:

$$\delta = \delta_0 \sin(2\pi ft) \tag{4.7}$$

where f is the frequency of the PEM and sinusoidal modulated intensity (50 kHz), allowing equation (4.3) to be rewritten as:

$$I = I(0) + I(f)\sin 2\pi ft + I(2f)\cos 4\pi ft + ...$$ (4.8)

In Eq. (4.8), I(0) is the DC intensity measured at the detector, I(*f*) is the first harmonic of

the frequency of modulation (50kHz), and I(*2f*) is the second harmonic (100 kHz). The

DC, *1f* and *2f* functions can be approximated using Bessel functions yielding the

expressions:

$$I(0) = I_0[R(1 + J_0(\delta_0)\sin(\Delta\theta + 2\varphi)]$$ (4.9)

$$I(f) = I_0 \Delta R J_1(\delta_0)$$ (4.10)

$$I(2f) = 2I_0 R J_2(\delta_0)\sin(\Delta\theta + 2\varphi)$$ (4.11)

where J_n are the Bessel functions of nth order. The first three Bessel functions are plotted

in Figure 4.5:
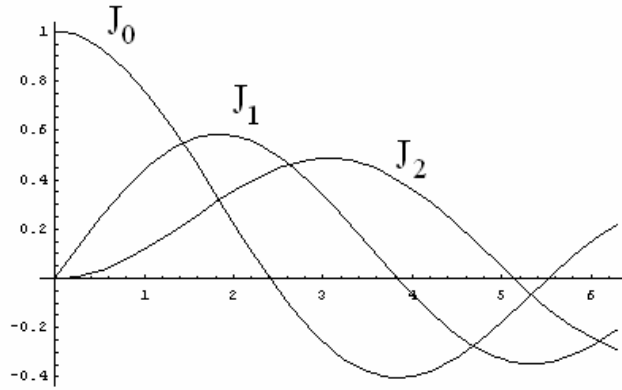
Figure 4.5
Plots of the 0th, 1st and 2nd order Bessel functions

Equations (4.9, 4.10 and 4.11) show that the first harmonic depends on ΔR and is

proportional to the Kerr Ellipticity, and the second harmonic depends on the Kerr

Rotation. By choosing $\delta_0 = 2.4$ radians, it can be seen from figure 4.5, that the DC

component is made independent of the Kerr rotation ($J_0(\delta_0)= 0$), and is directly

proportional to the laser intensity.

The Kerr rotation and Kerr ellipticity can be extracted from the modulated signal at the

detector by first recognizing that the Kerr rotation (θ_k) and Kerr ellipticity (ε_k) are equal

to:

$$\theta_k = -\frac{\Delta\theta}{2} \quad \text{and} \quad \varepsilon_k = \frac{\Delta R}{4R} \tag{4.12}$$

The Kerr rotation and ellipticity can be calculated from ratios, $I(f)/I(0)$ and $I(2f)/I(0)$. In

the general case where the angle (ϕ) of the analyzer is set to zero, the ratios, $I(f)/I(0)$ and

$I(2f)/I(0)$ can be expressed as:

$$\frac{I(f)}{I(0)} = \frac{AI(f)}{I(0)} = AJ_1(\delta_0)\frac{\Delta R}{R} \tag{4.13}$$

$$\frac{I(2f)}{I(0)} = \frac{BI(2f)}{I(0)} = BJ_2(\delta_0)2\Delta\theta \tag{4.14}$$

Dividing by the DC component results in values that are independent of the laser

intensity, therefore the measurement results are independent of laser noise and other

intensity fluctuations.

Correction factors A and B were added in Equations (4.13 and 4.14) to denote parameters

representing the ratio of gains for the detector-amplifier system for the modulated ($1f$ and

$2f$) components to the DC component. Using Eq. (4.12) the Kerr rotation and ellipticity

are calculated to be:

$$\theta_k = -\frac{1}{BJ_2(\delta_0)}\frac{I(2f)}{I(0)} \tag{4.15}$$

$$\varepsilon_k = \frac{1}{4AJ_1(\delta_0)}\frac{I(f)}{I(0)} \tag{4.16}$$

These equations show that the Kerr ellipticity is proportional to fundamental modulation frequency, while the Kerr rotation is proportional to the second harmonic of the modulation frequency[13]. Given that A and B are determined from the system, the Kerr rotation and Kerr ellipticity can be directly measured using a lock-in amplifier set to measure signals modulated at frequencies corresponding the Kerr ellipticity (50 kHz), and the Kerr rotation (100 kHz). These frequencies were chosen because the bandwidths of the lock in amplifiers are 100 kHz, so the first and second harmonics can be measured without obstruction.
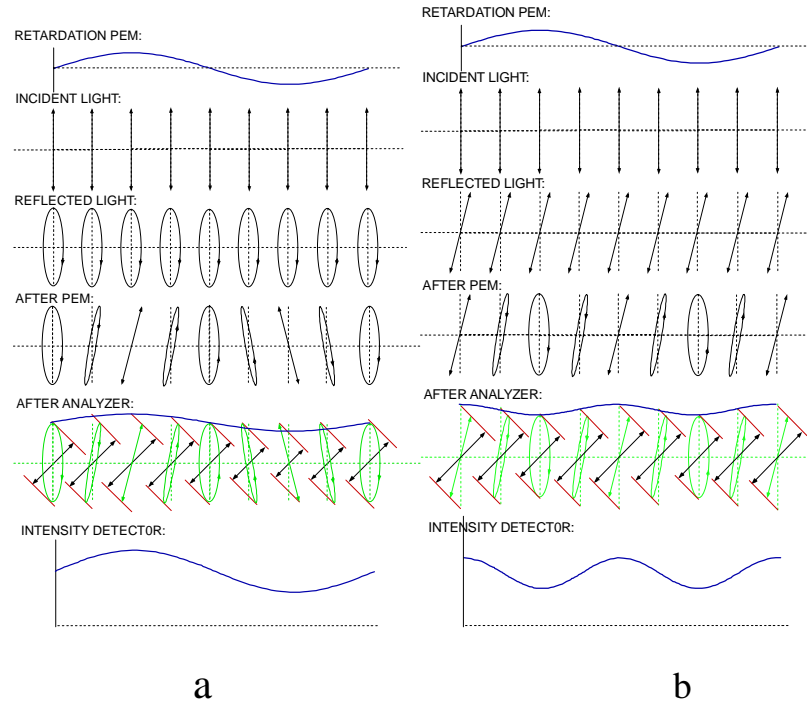
Figure 4.6
Polarizations of light and the resulting intensity at the detector
a) strong Kerr ellipticity; b) strong Kerr rotation[14]

Figure 4.5 illustrates the entire process, from the linearly polarized incident light to the

waveform of the intensity at the detector for a material with a strong Kerr rotation and

strong Kerr ellipticity. At the top, the retardation of the PEM is shown along with the

state of polarization of the incident beam. The Kerr effect will cause a rotation in the

polarization plane of the reflected beam, and a small ellipticity to be introduced. The

PEM will modulate the state of polarization, and the analyzer will convert the varying

state of polarization into a varying beam intensity that is detected at the photodetector.

4.2.2 Kerr Tracer Setup

A block diagram of the optical components of the Kerr Tracer in its present configuration is shown below:
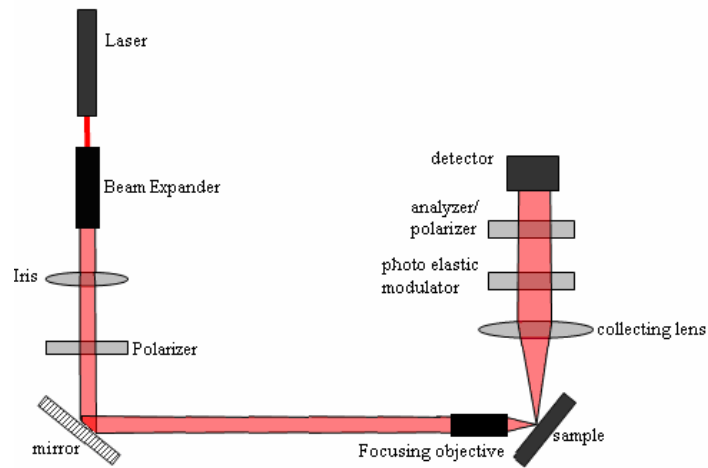
Figure 4.7
Block diagram of the current Kerr Tracer optical components and configuration[15]
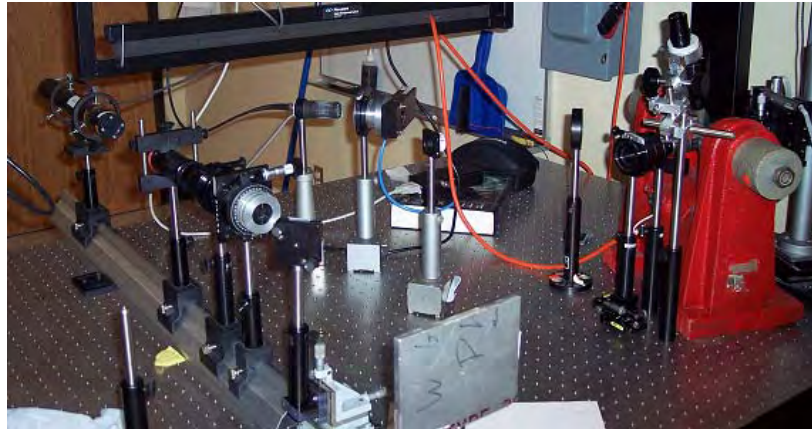
Figure 4.8
Photo of current Kerr Tracer setup

4.2.1.1 Optical and Mechanical Components

The components of the setup and their respective functions are described below:

Melles Griot 05 STP 901 HeNe Intensity Stabilized Laser – produces a highly collimated beam of light with a 632.8 nm wavelength. The laser has the option of being wavelength or intensity stabilized, depending on application specifics. Since the intensity variations should be minimized for optimum detection of Kerr effects, the intensity stabilization is used in this setup. The intensity of the beam is stabilized internally by automatic adjustments of the resonant cavity. This laser used in the setup has a beam diameter of 0.5 mm with a full cone divergence 1.8 mrad. The intensity stabilization limits intensity fluctuations to less than 0.02% over one minute and less than 0.1% over one hour.

Beam Expander – A beam expander was used to increase the diameter of the beam and decrease the divergence. A beam expander typically uses a combination of lenses in an arrangement similar to that in the figure below:
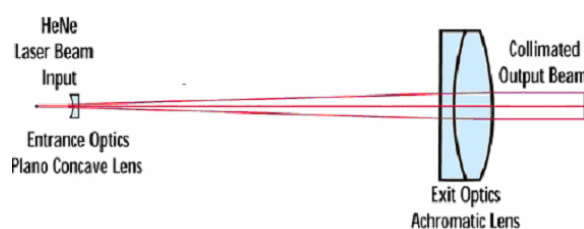
Figure 4.9
Beam Expander[27]

The planar concave lens causes the beam to diverge while an achromatic lens then re-collimates the beam, resulting in a highly-collimated expanded beam with a large diameter and a very low divergence; both of which are desirable for focusing to a small

spot size. It is also possible to accomplish this using a spatial filter, as was done in previous configurations of the setup. A spatial filter is generally two positive lenses where the focal distance of the first lens is smaller than the focal distance of the second. The distance between the two lenses is the sum of their focal distances, so that a parallel input beam will create a collimated output beam with a larger diameter. A pinhole is located at focal point to create a homogeneous beam intensity profile. This type of expander has advantages. However it is not used because alignment is very critical, and is sensitive to small displacements of the beam.

Mirror – section of polished silicon wafer directs the laser toward the sample.

Polarizer – linearly polarizes the incident laser beam. Measurement of the longitudinal Kerr effect is desired; therefore the polarizer is oriented to produce s-polarized light with respect to the plane of incidence. This results in the ability to measure only the component of magnetization parallel to the plane of incidence.

Focusing Objective – focuses the linearly polarized laser beam onto the sample. This lens must be strain-free, to prevent depolarization of the beam. The objective can be adjusted for best focusing onto the sample. The intricacies of the focusing objective are discussed thoroughly in the description of the Scanning Kerr Microscope, as a small spot size is essential to observing domains.

Electromagnet – produces the external H-field between the poles of the magnet. The field orientation results in sample magnetization in a direction lying mainly in the plane of incidence of the laser, giving rise to the longitudinal Kerr effect.

Sample Holder and Servo-Motors – holds the sample in place between the poles of the electromagnet. The high resolution servo-motors are used to precisely position the laser spot on the desired area of the sample. The movement of the motors is controlled from a computer by a LabView program.

Collecting Lens –after the beam is reflected from the sample it diverges. The collecting lens collects and focuses the diverging beam to conserve the intensity of the reflected light.

Photo Elastic Modulator (PEM) – modulates the elliptically polarized reflected beam by inducing a time dependent phase shift between the s- and p-polarized components of the beam. The phase difference is the result of birefringence induced by a fused silica bar vibrating in response to a piezoelectric transducer. The PEM used in the setup vibrates at 50 kHz.

Analyzer – the analyzer is a polarizer set to a fixed orientation and located immediately after the PEM. As the beam passes through the analyzer, its intensity varies based on its polarization state with respect to the orientation of the analyzer. The analyzer in the Kerr setup is set to 45°.

Photo Detector –collects the laser beam and measures the intensity after passing through

the analyzer. The detector sends electrical signals to a DC voltmeter and the Lock-in

Amplifiers proportional to the intensity of the light that reaches the detector,

4.2.2.2 Electronic and Software Components

The electronic components of the Kerr Tracer setup are listed and described below:

Power Supply/Switching Box – the power supply provides the voltage that drives the

electromagnet while the switching box changes the polarity, thus reversing the polarity of

the field. The current setup has a reliable field setting resolution of 0.25 Gauss and a

maximum field of 1200 Gauss.

Gauss Meter – measures the magnetic field intensity between the poles of the

electromagnet and provides the H-field measurement data used in plotting the hysteresis

curves.

Lock-in Amplifiers (LIA) – The lock-in amplifiers can measure signals embedded in

noise often much larger than the signal amplitude, by "locking-in" on signals at a certain

frequency, for example, an AC voltage at a frequency specified by a reference input. In

this setup the reference frequency is supplied by the PEM at 50 kHz. The LIAs can also

measure signals at harmonics of the fundamental frequency. Currently there are two

Stanford Research LIAs measuring the Kerr signals. Using two LIAs allows the

measurement of the Kerr ellipticity (50 kHz) and the Kerr rotation (100 kHz)

simultaneously.

DC Voltmeter – gives a DC voltage proportional to the intensity of the reflected laser

beam that reaches the photo detector. Although the laser is intensity stabilized, small

variations in the DC intensity occur, but the LIA measurements can be adjusted, or

normalized, by the DC measurement to account for these variations.

Computer/LabView – A computer running Windows XP is used to communicate with

and control the electronic components of the Kerr Tracer. In conjunction with equipment

drivers, LabView programs were created to control and take measurement data from the

various electronic components via GPIBs.

4.3 Scanning Kerr Microscope

The Scanning Kerr Microscope used for the domain analysis was built from the existing Kerr Tracer components and was initially created by Hans Willem ten Brinke in the summer of 2004. The optical setup of the Scanning Kerr Microscope is basically the same as the Kerr Tracer, and uses the same technique for measuring the Kerr effects. Domains are observed using the contrast in the magneto-optical Kerr effects exhibited by domains with different magnetization orientations. For example, two domains with anti-parallel magnetization will have Kerr effects with amplitudes that differ only in sign. The difference in sign results in a modulated contrast in the intensity of light reaching the photodetector measured at the lock-in amplifiers. The Scanning Kerr Microscope scans the surface of the sample with the laser spot and measures the Kerr signal at points along the scan. The scan area and sampling rate can be specified in the control software. The points are plotted with a color contrast representing the contrast in the Kerr effects measured, producing a pixel by pixel image of the magnetic surface of the sample. The color contrast creates an image of the sample surface where areas of different magnetization direction can be distinguished, thus revealing the domains patterns.

4.3.1 Scanning Kerr Microscope Setup

The majority of the Kerr microscope setup is identical to the Kerr Tracer setup. However, there are two components that can be neglected in the Kerr Tracer application that are vital for the Kerr Microscope: the servomotors and the focusing objective. These components are critical for the Scanning Kerr Microscope because the resolution is

dependent on the minimum step size of the motors and more importantly the spot size of the laser.

The servomotors are used to move the sample, allowing the laser to scan the surface. The Encoder Mike servomotors used are operated on an independent power supply (Encoder Mike amplifier 18104) and controller card (DMC-1000), all from Oriel Instruments. The motors have a range of 25mm in both the x and y-directions, with a resolution of 25nm. The error in the absolute position is determined by several factors: mass, speed and the settings of the built in PID controller. After the PID settings were optimized the motors could be positioned very accurately. The absolute position errors of the motors were less than 100 nm horizontally and 400 nm vertically[14]. Since the motors had position sensors with an accuracy down to 25nm, the position errors were not cumulative.

4.3.2   Beam Focusing

The resolution of the Scanning Kerr Microscope is only as good as the minimum spot size that can be focused on the sample; the smaller the spot size, the smaller the domains the instrument can resolve. When focusing a laser beam, there are two contributions limiting the minimum spot size. The first is the Rayleigh criterion.

Assuming the laser beam has a typical Gaussian profile, focusing the beam to its minimum spot size through a lens with a diameter (D) and a focal length (*f*) would resemble Figure 4.10:
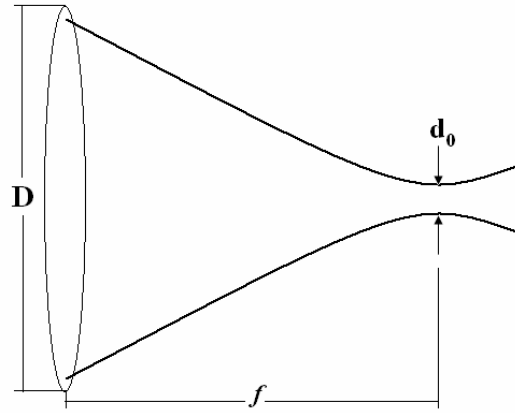
Figure 4.10
Schematic of focusing a Gaussian Beam

Neglecting various aberrations, when a highly collimated Gaussian beam is focused by a lens of focal length (f), the beam waist is the focal spot of diameter w_0, and is theoretically located at a distance equal to (f) from the center of the lens[28]. In reality, the waist is located at a point inside the geometrical focal length, but this is insignificant here because the diameter of the spot size is the only parameter of interest here, not the position. Letting $w(f)$ be the Gaussian spot size at the lens, a relationship between the focal spot size (w_0), the diameter of the beam entering the lens $w(f)$, the focal length (f) of the lens, and the wavelength of the laser (λ) can be represented by:

$$w_0 \cdot w(f) \approx \frac{f\lambda}{\pi} \tag{4.17}$$

This relation implies that the minimum focal spot will occur when the lens aperture is flooded to the maximum extent by the incident beam. For practical purposes it is common to let:

$$D = \pi w(f) \tag{4.18}$$

thus adopting the 99% criterion for the focusing lens, while at the same time adopting the 1/e criterion for the focused spot, which would imply:

$$d_0 = 2w_0 \tag{4.19}$$

thus defining d_0 as the effective diameter of the focused spot. Combining the two

criterion gives an approximation for the minimum focusable spot size as:

$$d_0 \approx \frac{2f\lambda}{D} \tag{4.20}$$

Another common term involved in focusing optics is the f-number or f# defined as:

$$f\# = \frac{f}{D} \tag{4.21}$$

which is the ratio of effective focal length to the lens diameter. Introducing the f#

simplifies Eq. (4.20) to:

$$d_0 \approx 2f\#\lambda \tag{4.22}$$

It is clear from Eq. (4.22) that the minimum spot size is directly proportional to

the f# of the focusing lens used, assuming that the lens is flooded. This limit on the

minimum spot size is commonly called the Rayleigh criterion[29].

In addition to the Rayleigh criterion, the minimum obtainable spot size is also

limited by the aberrations of the lens system. Aberrations occur in many forms including,

spherical aberration, coma and astigmatism, and can degrade image quality and

significantly increase the size of a focused spot. Aberrations are the result of rays passing

through a lens outside the paraxial region that are refracted at higher angles and focused

in front of the paraxial rays. In particular, spherical aberration (SA) is the main factor

prohibiting the ability to focus a Gaussian beam to the theoretical spot size set forth by

the Rayleigh criterion. The Figure 4.11 is a schematic ray trace demonstrating SA.
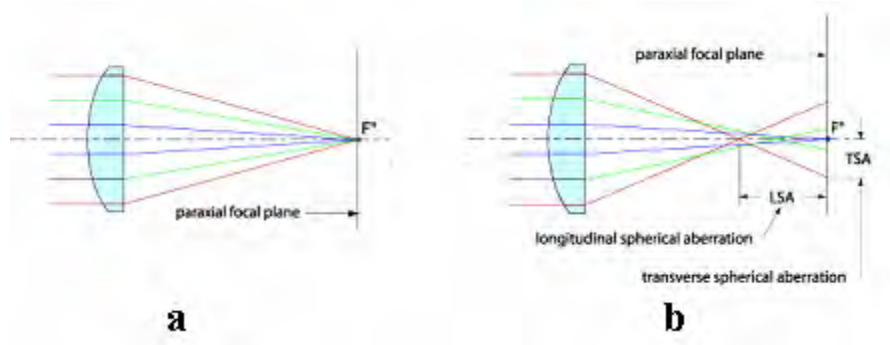
Figure 4.11
Lens focusing: a) with no spherical aberration;
b) with spherical aberration[30]

In general, the rays entering the lens farthest from the paraxial region are focused farther inside the focal length and intersect the focal plane at a greater distance from the paraxial focal point. The distance along the optical axis from the intersection of the marginal rays to the primary focal point is the longitudinal spherical aberration (LSA), whereas the distance between the primary focal point and the intersection of the marginal rays with the focal plane is the transverse spherical aberration (TSA). The LSA and TSA are related by:

$$TSA = LSA \cdot \tan \theta \tag{4.23}$$

where θ is the angle between the optical axis and the marginal ray from the intersection of the LSA .

The total spherical aberration is dependent on several factors including lens shape, f#, material composition and index of refraction. The LSA can be calculated via a surprisingly simple equation (Eq. 4.24), granted the aberration constant (k) for the lens type is known[30,31].

$$LSA = \frac{k \cdot f}{(f\#)^2} \tag{4.24}$$

The aberration constants (k) for most common lens types are given in Figure 4.12 below:
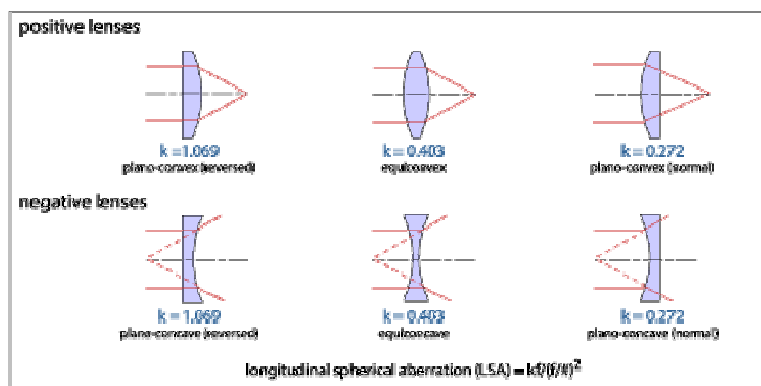
Figure 4.12
Spherical aberration constants for common lenses[30]

It should be noted that the aberration constants listed above are correct only to the third order[31]. For an exact calculation, the use of a ray tracing program is necessary. Calculations on such a program have been done using MathCAD. The details of the ray tracing program and the calculation can be found in Appendix B. Based on the aberration conditions and the Rayleigh criterion, it is evident that there is a problem resulting from criteria with opposing means of minimizing the spot size. The Rayleigh criterion shows that the minimum spot size is achieved by maximizing the diameter of the incoming beam, i.e. flooding the lens. However, flooding the lens allows light to enter far from the paraxial region, inevitably resulting in spherical aberration. Most compound objectives are designed to minimize aberrations, thus the minimum spot size is limited by the Rayleigh criterion and is achievable by flooding the lens. The smallest spot size will result from the incoming beam size that is the best compromise between the two limiting factors.

4.3.3 Spot Size Profiling

Theoretical calculations are rarely acceptably accurate when dealing with optical systems where aberrations are significantly present and the fact that the waist of a Gaussian beam lies inside the focal length: a position that is best found experimentally. With this in mind, a measurement technique was developed for estimating the size of the focused laser spot using the existing Kerr microscope components. The servomotors were used to move the sample under the laser spot thus scanning a single line across the surface. During the scan, the DC intensity from the photodetector was monitored and plotted vs. the position of the beam on the sample. It was assumed that if the spot passed over a sharp step between a highly reflective film (high DC intensity measured), and a less reflective substrate (lower DC intensity measured), the distance over which the transition between high and low DC intensities occurred would be a good estimate of the spot size.
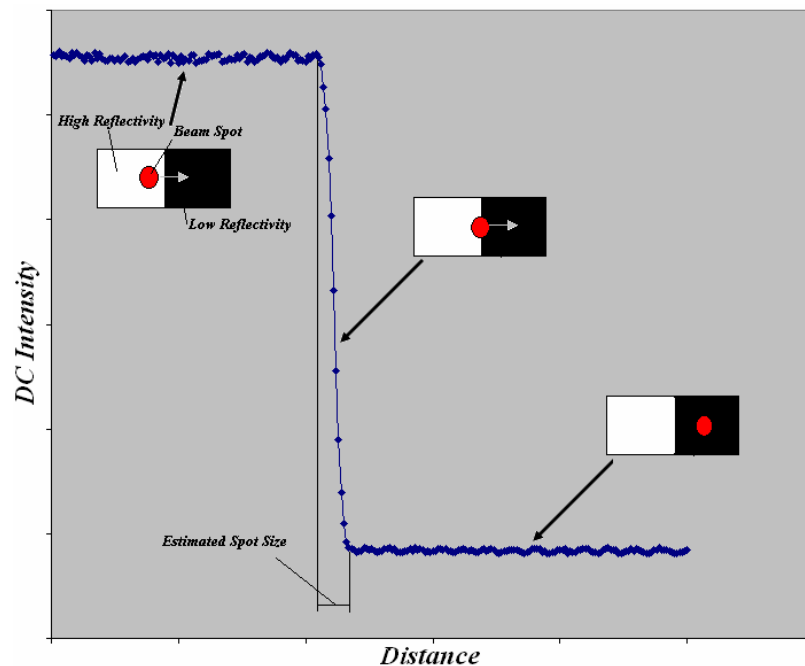
Figure 4.13
Schematic representation of spot size measurement procedure

Control software for the profile scanning method was written to control and record the movement of the servomotors, monitor DC signal and analyze the data. In addition to directly measuring and plotting the DC signal and position, the software calculates the derivative of the intensity with respect to position, and plots it vs. the position to allow a more accurate estimate of the spot size.

4.3.4   Investigation of Modified Setup

A modified configuration of the Scanning Kerr Microscope was investigated with the intention of increasing the resolution by decreasing the minimum obtainable spot size. The setup was modified to the configuration shown below:
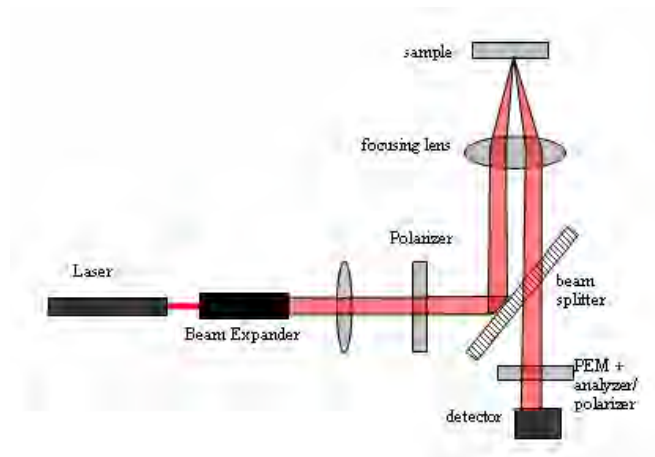
Figure 4.14
Proposed configuration of high
resolution Scanning Kerr Microscope[15]

The new configuration is theoretically a higher resolution arrangement[26]. The major change compared to the original setup is the use of the same lens as the focusing and collecting lens. In this arrangement, it is imperative that the focusing/collecting lens be strain free, because strain in the lens would induce depolarization effects. The mirror

in the original setup was replaced by a beam splitter to allow the light to reach the

detector after passing through the focusing/collecting lens. As with the other optics in the

system, the beam splitter was made of UV grade fused silica to prevent depolarization

effects. Furthermore, the light incident on the beam splitter was s-polarized to avoid any

change in polarization of the incident beam upon reflection from the beam splitter. The

beam splitter used a Thor Labs BSW16 with a diameter of 50.8mm[15]. The major

advantage of this setup is that it allows for a much smaller working distance, and

according to Eq. (4.20), it would reduce the minimum obtainable spot size. Also, the

angle of incidence of the laser beam depends on the f# of the lens. For the longitudinal

Kerr effect, the higher the angle of incidence, the stronger the signal, and there are no

effects observed at normal incidence. After the new configuration was implemented, the

next task was to verify that the modification was in fact an improvement to the setup by

determining the minimum achievable spot size. The focusing lens used was a plano-

convex lens with a focal length of 5cm in combination with a meniscus lens with a focal

length of 7.5 cm. Both lenses had a diameter of 1 inch. The angle of incidence was

achieved by focusing the laser from near the edge of the lens, and collecting the reflected

beam near the opposite edge. Measurements were taken for the incoming beam near the

left edge of the focusing lens; this is the position that would yield the highest angle of

incidence which is the most favorable for observing Kerr effects. The lens was initially

positioned as close to the sample as the setup would allow, and moved farther away in

increments of 1 mm. Measurements were first taken at each millimeter interval spanning

the entire range of the micrometer. After analyzing the measurements it was determined

that the minimum spot size fell in the 0.75mm to 1.25mm object distance range.

Measurements were then taken every 50 microns within the best focus range.

Spot Size vs. Working Distance
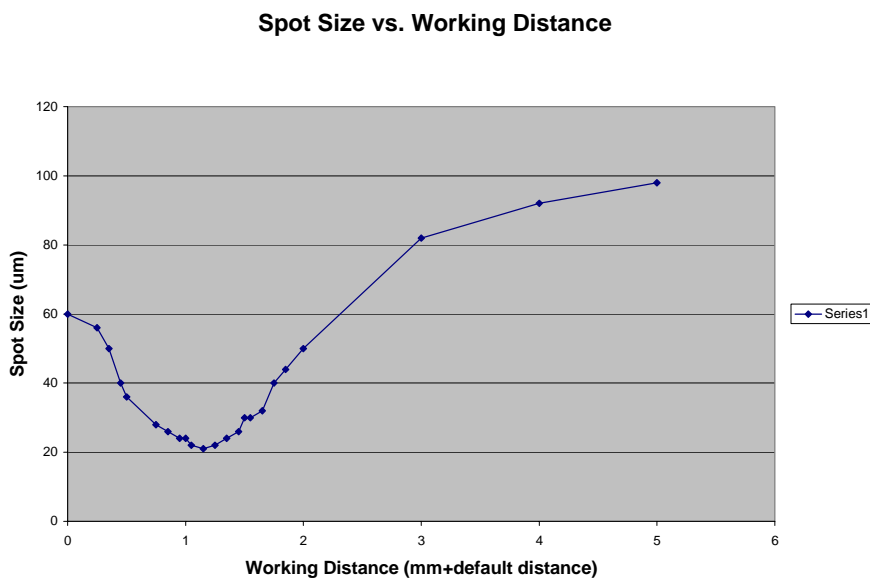
Figure 4.15
Spot Size vs. Working Distance

Figure 4.15 shows the spot size for different working distances. The working distance

was determined from the reading on the micrometer that was used to move the lens. It

should be noted that there was some unknown default offset resulting from the limited

range of the micrometer (i.e. at 0mm the lens was not in contact with the sample). From

the results, it was determined that the minimum obtainable spot size was 21 microns.

Clearly this was not an acceptable alternative to the original setup, in fact, the resolution

was over a factor two lower than the original setup. This was found to be the result of the

beam entering the lens so far from the optical axis that the spherical aberration was

extremely limiting the spot size. One way to decrease the aberration was to limit the size

of the beam entering the lens, which goes against the Rayleigh criterion as well as

decreases the measurable intensity causing additional problems when measuring the Kerr

effects. Another way to decrease the aberration was to move the beam closer to the center

of the lens. As the beam was moved closer to the center of the lens smaller spot sizes

were measured, but the Kerr signals became weaker as the angle of incidence decreased.

Spot sizes near 8 microns were measured at the center of the lens, but no Kerr effects are

measured at normal incidence, so this offered no advantage.
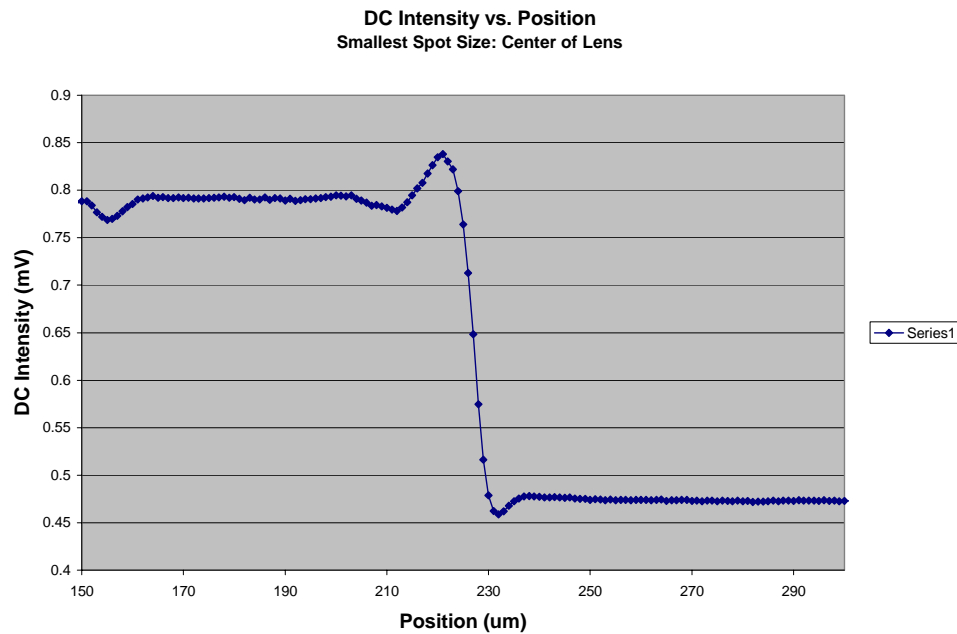
Figure 4.16
DC Intensity vs. Position for center of lens

DC Intensity Derivative
Smalllest Spot: Center of Lens
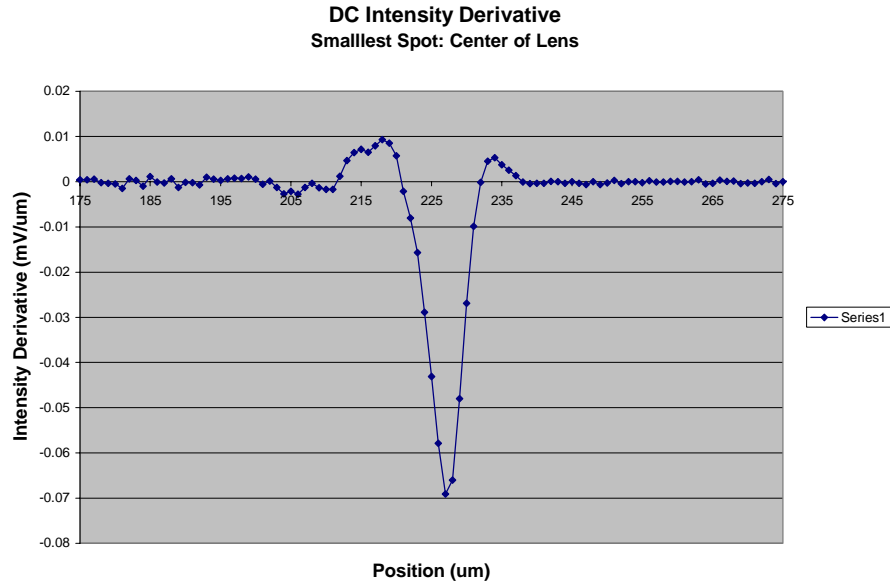
Figure 4.17
DC Intensity Derivative vs. Position for center of lens

The focusing lens being used was a compound lens consisting of a plano-convex lens with a meniscus lens directly in front of it. The meniscus lens was placed in the mounting tube in an attempt to increase the numerical aperture of the focusing lens by reducing the focal length. The higher numerical aperture would effectively increase the angle of incidence, but at the same time it was believed to be increasing the aberration. The meniscus lens was removed and the spot size re-measured, but with no considerable improvement. It was concluded that for this setup the spot size was severely aberration limited, to a point that made it not useful for our setup. The major shortcoming of this setup was that there was no lens currently available that would offer a high numerical aperture while minimizing the spherical aberration for a beam entering off-axis.

4.3.5   Infinity Corrected Objective Focusing

Since there was no lens available for solving the aberration problems with the modified configuration, another method for focusing the laser spot was investigated: infinity corrected objectives. It was found that infinity corrected focusing objectives generally had extended working distances, ranging from 6 to34 mm, depending on power, and a relatively high numerical aperture. In addition to the extended working distance, objectives are also designed to minimize aberrations. Specifications for several Mitutoyo M Plan APO Series long working distance objectives are given in the table below:

Magnification	2X	5X	10X	20X	50X	100X
Numerical Aperture, NA	0.055	0.14	0.28	0.42	0.55	0.70
Working Distance, WD	34.0mm	34.0mm	33.5mm	20.0mm	13.0mm	6.0mm
Focal Length	100mm	40mm	20mm	10mm	4mm	2mm
Resolving Power	5.0µm	2.0µm	1.0µm	0.7µm	0.5µm	0.4µm
Depth of Focus	91.0µm	14.0µm	3.5µm	1.6µm	0.9µm	0.6µm

Table 4.1
Specifications for Mitutoyo M Plan APO Series Objectives[27]

Although the objectives listed in table 4.1 are rather expensive, there was no need to purchase any objective(s), because three of the Mitutoyo M Plan APO objectives (20x, 50x and 100x were available. The objectives were previously purchased for the Laser Writer Lithography system, and were not currently in use. Each of the objectives was installed in place of the original focusing lens and spot sizes were profiled for the 20x and 50x objectives. Theoretically the smallest spot sizes based on the Rayleigh criterion for the 20x and 50x objectives are 1.38 µm and 0.96µm, respectively. Since the objectives were infinity corrected, it was assumed that the aberrations would be minimized for a collimated laser beam and the spot size would be diffraction limited. Since the working distance of the 50x objective was only 13mm, it would have limited the obtainable angle

of incidence, so it was dismissed as an applicable replacement. The attention was then

placed entirely on the 20x objective. It offered both an acceptable resolving power and a

decent working distance (20mm), making it the most suitable replacement for the original

focusing unit. Spot size scans were done using the 20x objective and the results are

shown in Figure 4.18 below:

Objective Lens Focusing: Smallest Spot
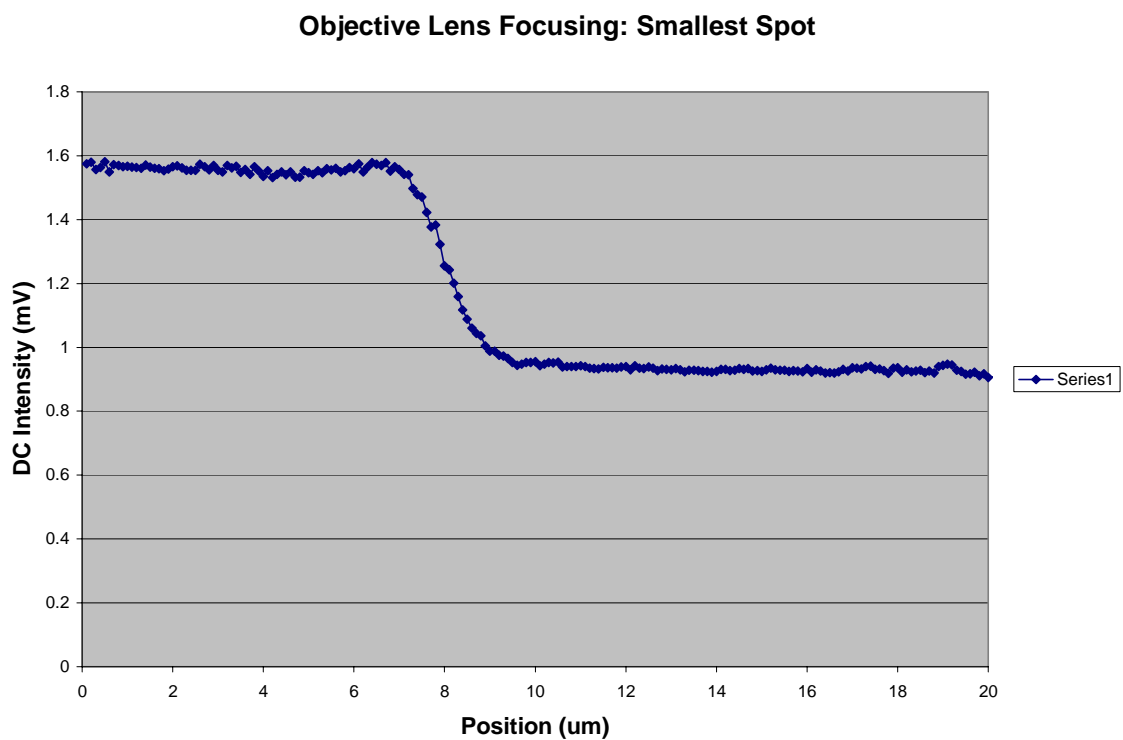
Figure 4.18
Intensity vs. Position for small spot

The smallest spot size measured was ~2.25μm, which was larger than the theoretically

calculated value. One possible reason for the enlarged spot size was that Raleigh criterion

was not optimally satisfied. When the iris was opened to a point that allowed the beam to

fill the lens, the beam was reflected off the objective and sample back into the resonating

cavity of the laser, which interfered with the intensity stabilization. Back reflection can

damage the laser and reliable measurements cannot be taken unless the laser is stabilized,

therefore the incoming beam was restricted, but just to the extent that did not allow significant reflection back into the laser. Although the beam was restricted as little as possible, it was enough to prevent the beam from filling the lens, which likely contributed to a larger spot size. While not ideal, the spot obtained with the objective was the smallest measured thus far.

4.4   Magnetostriction Measurement System

The magnetostriction setup used for the magnetoelastic characterization directly measures the magnetostriction of a cantilever strip consisting of magnetic thin films deposited on non-magnetic substrates. The sample is placed in the sample holder that clamps the sample at one end, leaving the other end free. An external magnetic field applied in the plane of the sample will induce magnetostriction in the film causing the sample to bend from the strain on the non-magnetic substrate. A photonic sensor is used to detect the magnitude of deflection, i.e. the bending of the strip. To understand the measurement results, a relation between the deflection of the sample and the induced magnetostriction must be formulated. Prior to the derivation of this relation, the physical setup will be introduced and discussed.

4.4.1   Magnetostriction Setup

The first component of the magnetostriction measurement setup is the sample. In order for the system to operate properly, the samples must consist of a ferromagnetic film deposited on non-magnetic substrates i.e. glass or silicon. These types of samples are referred to as cantilever strips, and have the following basic structure:
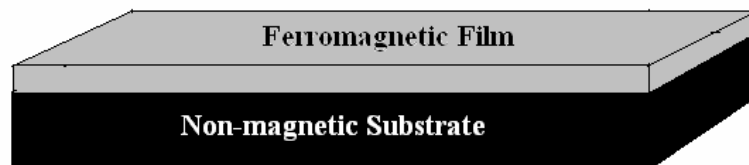
Figure 4.19
Cantilever structure of magnetostriction samples

A block diagram of the magnetostriction setup is shown in Figure 4.20.
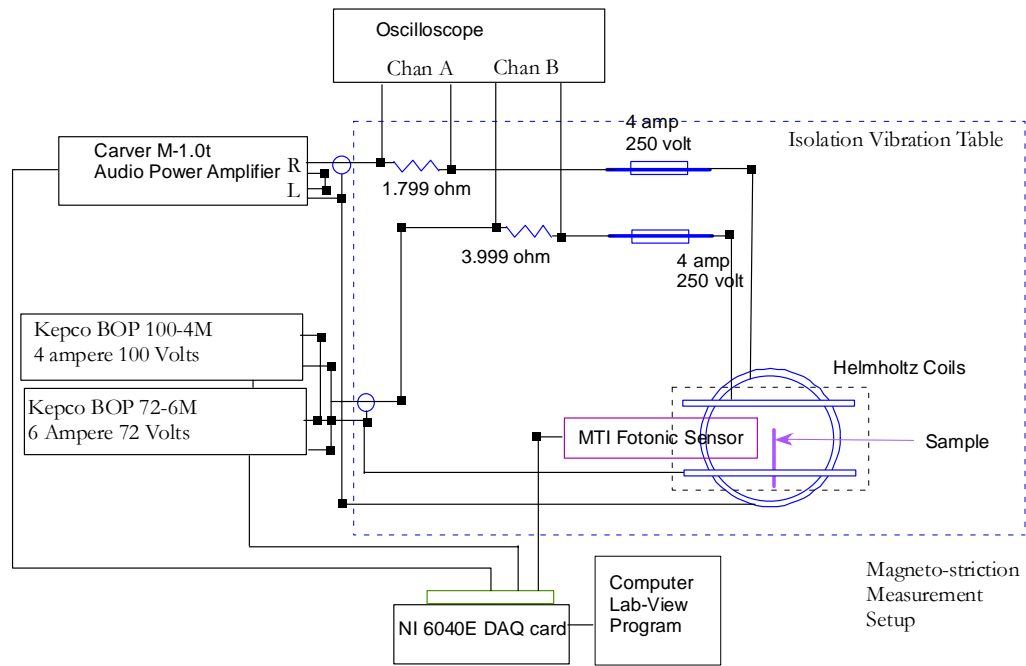
Figure 4.20
Block diagram of magnetostriction setup

The Helmholtz coils are powered by sinusoidal currents generated by the PC, and amplified by the audio amplifier and two Kepco power supplies. The setup has two pairs of Helmholtz coils that enclose the sample holder; one set runs vertical (inner coils) and the other horizontal (outer coils). The sinusoidal signals sent to each pair of coils are 90° out of phase, equivalent to one set of coils following a sine function and the other a cosine at a time (t). This arrangement produces a magnetic field that rotates at a frequency f_0 in the plane of the sample. The current setup uses a frequency (f_0) of 20 Hz to control the field. The rotating field causes the sample to vibrate, and the Fotonic sensor transforms the displacement of the sample to an electric signal with a frequency f equal to $2f_0$, because the sample deflects twice during each sine cycle. The components of the setup are listed and described below:

PC – The PC controls the setup and acquires the data through a LabView program written by graduate student Jonathan Garrett. The program generates and checks the sinusoidal functions used to power the coils and produce the magnetic field, and the software receives and records the electronic signals from the Fotonic sensor.

Amplifier – The weak signal generated by the PC software is amplified by the audio amplifier or Kepco power supplies and sent to the Helmholtz coils. Since the frequency (f_0) of the sine wave is rather low, a high end audio amplifier is perfectly capable of amplifying the signal.

Helmholtz Coils – The Helmholtz coils are responsible for providing the magnetic field used to induce the magnetostriction in the samples. The current setup has two sets of coils arranged as in figure 4.21 below.
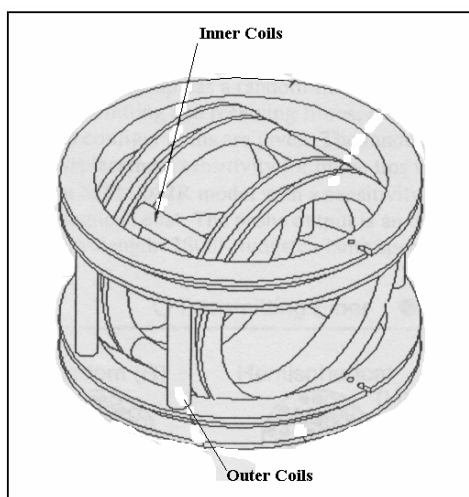
Figure 4.21
Arrangement of Helmholtz coils in magnetostriction setup[10]

Each coil is identical to the other coil in the set, but the two sets themselves are not identical. If two coils are placed a distance (L) apart, they will produce a homogeneous field at a point (x) in the center of the coils (x = 1/2 L), illustrated in figure 4.22:
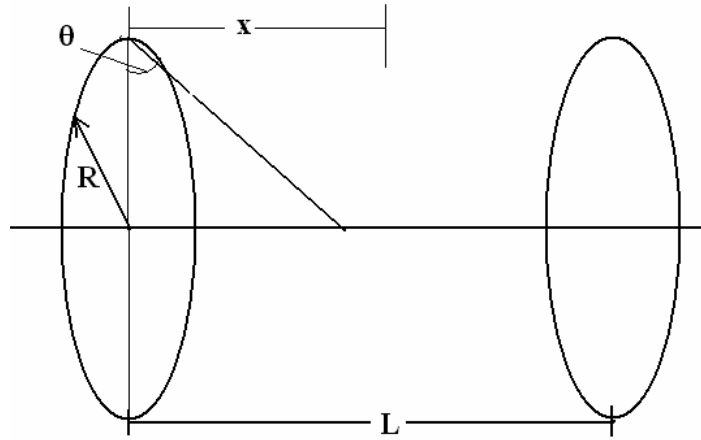
Figure 4.22
Schematic of two parallel Helmholtz coils

The field at the center of two coils can be determined by first considering the effect of one coil with radius (R) and (N) turns of wire carrying a current (I). The field B at a distance (x) along the central axis of the coils can be represented by:

$$B(x) = \frac{\mu_0 NI}{4\pi} \cdot \oint \frac{\cos\theta}{R^2 + x^2} dl \qquad (4.25)$$

where:

$$\cos\theta = \frac{R}{(R^2 + x^2)^{\frac{1}{2}}} \qquad (4.26)$$

Substituting (4.26) into (4.25) yields:

$$B(x) = \frac{\mu_0 NI}{4\pi} \cdot \frac{R^2}{(R^2 + x^2)^{\frac{3}{2}}} \cdot \oint dl \rightarrow \frac{1}{2}\mu_0 NI \cdot \frac{R^2}{(R^2 + x^2)^{\frac{3}{2}}} \qquad (4.27)$$

The addition of a second identical coil located at a distance L from the central plane of the first will modify (4.27) to account for the second coil.

$$B(x) = \frac{1}{2}\mu_0 NI \cdot R^2 \left[\frac{1}{(R^2 + x^2)^{\frac{3}{2}}} + \frac{1}{(R^2 + [L-x]^2)^{\frac{3}{2}}} \right] \qquad (4.28)$$

Since the field is desired to be homogeneous for a given current (I), Eq. (4.28) can be simplified by letting $L = R$ and $x = \frac{1}{2}R$, giving:

$$B(x = \tfrac{1}{2}R) = \mu_0 NI \cdot R^2 \left(\frac{1}{R^2 + \tfrac{1}{4}R^2} \right)^{\frac{3}{2}} = \left(\frac{4}{5} \right)^{\frac{3}{2}} \cdot \frac{\mu_0 NI}{R} \qquad (4.29)$$

Since it is physically impossible to have two sets of coils at the same distance (L) apart, one set must fit inside the other. In order to produce a homogeneous field at the center of all four coils the number of turns (N) must be adjusted so that the difference in geometry is compensated for and the field acting on the sample is homogeneous with a given current (I). Table 4.2 gives the specifications for the coils in the setup.

	Inner Diameter (mm)	Outer Diameter (mm)	Distance Between (mm)	Turns (N)	Wire Diameter (mm)	R (Ω)	L (mH)
Inner Coils	98	122	48	140	0.8	3.46	6.26
Outer Coils	128	158	70	180	0.8	5.75	14.53

Table 4.2
Helmholtz coil specifications[10]

The maximum field obtainable by the coils in the current setup is 170 Oe. To curb

the heat generated by the coils, the software applies a pulsed current to the coils for one

to two seconds during which measurements are taken, and then the coils are allowed to

cool for a few seconds before the next field step is applied. Since the setup was not

originally designed to operate at 170 Oe, measurements taken above 75 Oe would show

small noise signals (<40 Å) for non-magnetic silicon substrates. This was not a major

concern because the noise was reproducible and negligible for samples with a large

magnetostriction, and could be subtracted from measurements of samples with a weak

magnetostriction. The Deflection vs. H curve for a SiO_2 substrate is shown in Figure

4.23.

Background Signal from SiO2 Substrate
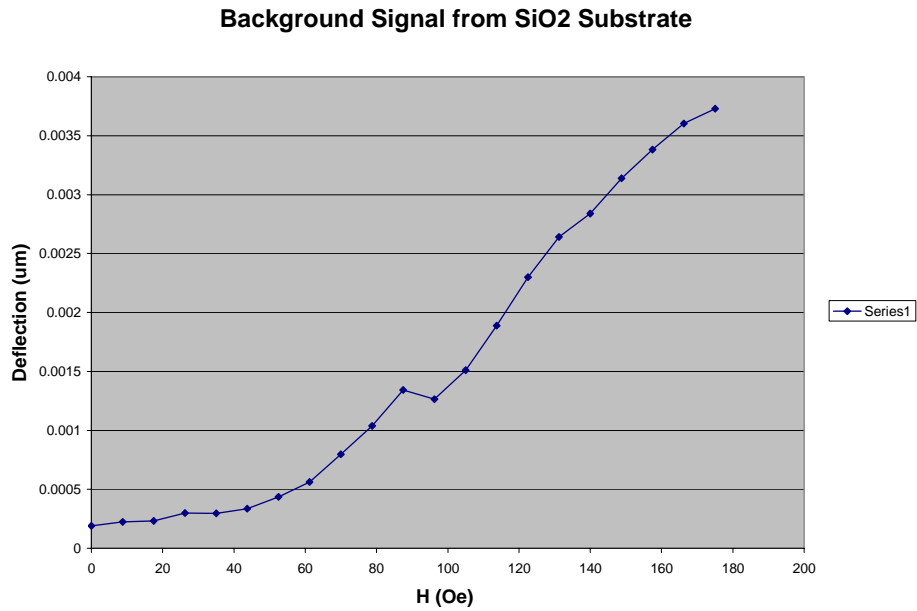
Figure 4.23
Background signal measured for SiO$_2$ substrate

Fotonic Sensor – The Fotonic sensor used to measure the displacement of the sample vibrations is an MTI – 2000 with a fiber-optic probe tip. The tip used in the magnetostriction setup has a random fiber distribution, where the transmitting and receiving fibers are randomly distributed on the probe tip.
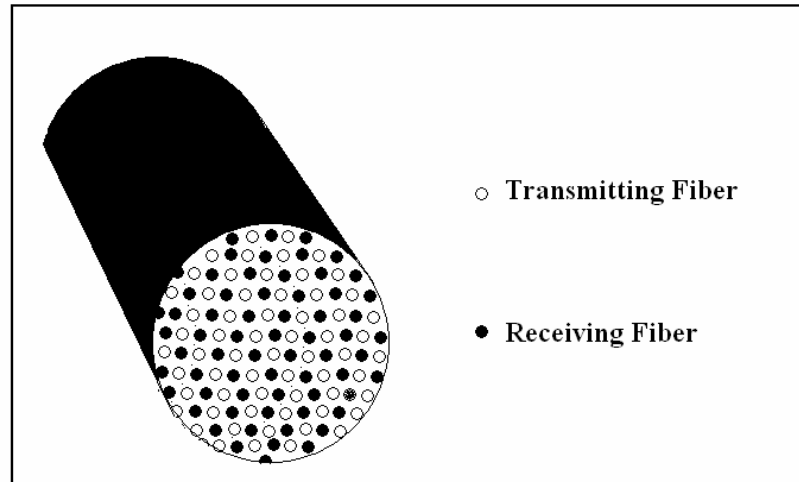
Figure 4.24
Randomly distributed probe tip

The fiber-optic probe tip offers several advantages over other magnetostriction

measurement methods which use a laser and a separate sensor to measure the deflection

of the sample. Namely the fiber-optic tip increases the speed at which measurements can

be taken. During measurements, the probe tip is positioned close enough to the sample to

allow most of the transmitted light to be collected by the receiving fibers. However, if the

tip is positioned too close to the sample, the transmitted light will be reflected back

toward the transmitting fiber and none will be collected by the receiving fibers. The

optimum position for the probe tip is set during the calibration procedure, and lies on the

slope of Range 1, as illustrated in the Instrument Output vs. Probe Gap plot (Fig. 4.25).
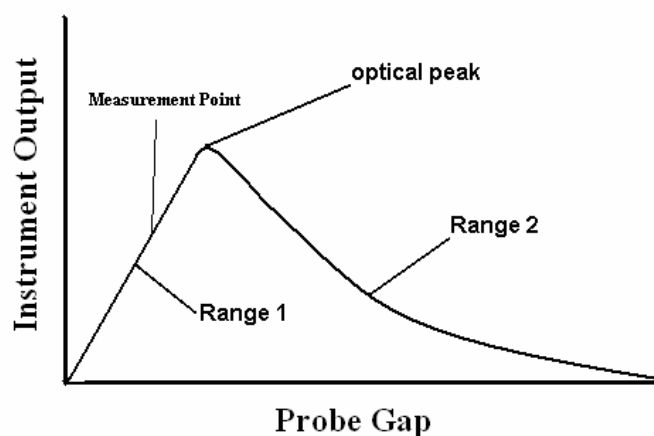
Figure 4.25
Output vs. Probe gap[19]

The tip position for measurements lies roughly on the center of the Range 1 slope, giving

a suitable range for measuring the deflection, since the probe gap will vary as the sample

vibrates. A photo of the physical setup and a simplified schematic are shown below:
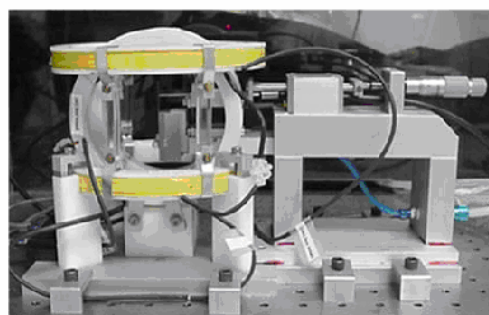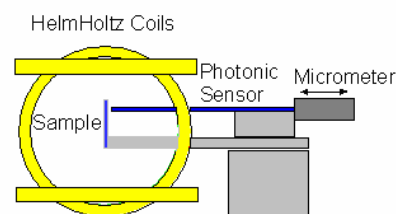
Figure 4.26
Magnetostriction setup: a) photo; b) schematic

The current setup has a sensitivity of 0.59 nm/mV due to a recent upgrade of the Fotonic

sensor.

4.4.2   Measurement Technique and Data Acquisition

The cantilever samples are initially loaded into the sample holder with the film facing the probe tip because the film will generally have a higher reflection coefficient allowing for more efficient measurements. As previously mentioned, the currents driving each pair of coils are 90° out of phase, causing the field in the plane of the sample to rotate. The coils are designed to produce a homogeneous field at the area of the sample. Since the field retains constant amplitude, but changes direction, the sample will experience a circularly rotating magnetic field. The magnetostriction measurements can be interpreted by recalling the equation for the magnetostriction of an isotropic material, (Eq. 2.76) from Chapter 2:

$$\lambda = \frac{3}{2} \lambda_s \left[\cos^2 \theta - \frac{1}{3} \right]$$
(4.30)

where θ is the angle between the magnetostriction and the direction of the measurement. For the circularly rotating field, the angle θ at a time (t) is:

$$\theta = \omega t$$

Giving the equation:

$$\lambda(t) = \frac{3}{2} \lambda_s \left[\cos^2 (\omega t) - \frac{1}{3} \right]$$
(4.31)

The maximum strain of the film will cause the maximum deformation and deflection of the sample. The maximum deflection ($D_{//}$) is a result of the y-component of the H-field and occurs twice for each cycle of the field rotation, A smaller deflection ($D_\perp$) caused by

the x-component of the field also reaches a maximum two times per field cycle. An

exaggerated illustration of the deflection is shown in the figure below:

$$\mathbf{D}_{/\!/} \xleftrightarrow{\hspace{2cm}} \mathbf{D}_{\perp}$$
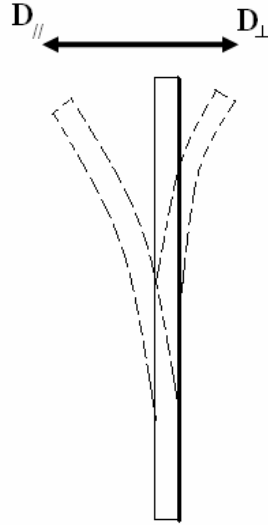
Figure 4.27
Exaggerated deflection of sample

   The deflection of the sample is the direct result of the magnetostriction of the magnetic

film bound to the non-magnetic substrate. The sign of the magnetostriction can be taken

from the deflection due to the y-component of the applied field. A deflection that

increases the probe–sample gap is taken to be positive, and a negative magnetostriction

results in a reduced gap. The actual magnitude of the deflection is directly measured by

the Fotonic sensor, and can be related to the saturation magnetostriction of the sample by

a formulation originally introduced by Klokholm in 1976, and later revised by

Du Tremolet de Lacheisserie and Peuzin for a more accurate model[10]. The original

formulation relating the total deflection (D) to the magnetostriction (λ) is used for the

measurements taken via the current setup, and is given by:

$$D = \frac{9}{2}\lambda_s l^2 \cdot \frac{E_f t_f}{E_s t_s^2} \frac{1-\nu_s}{1+\nu_f}$$ (4.33)

In (4.33), the total deflection (D) is equal to:

$$D = \left| D_{//} - D_{\perp} \right|$$

The term (l) is the effective length of the sample, (t) is the thickness, (E) is the elastic Young's modulus, and ν is the Poisson ratio of the film (f) and the substrate (s). The derivation for the deflection has been formulated and improved in several papers. More details on the derivations are available in the cited literature[20, 21, 22, 23].

4.4.3 Determining Sample Length

Eq. (4.33) shows that the deflection of the sample is proportional to the square of the length of the sample. In order to accurately calculate the magnetostriction from the deflection, the length of the sample must be known. For this reason, the sample holder was modified to allow the clamping distance to be determined. This was done by the fabrication of a variable length sample holder that could be adjusted to gain the maximum clamping distance depending on sample geometry. A millimeter scale was placed on the new sample holder to give a reference for the effective length of the sample. In the original setup the clamping distance was not adjustable and was taken to be 38 mm. Introducing the option of changing the clamping distance also required a modification of the software to allow different values for the effective length of the sample, since the deflection is directly dependent on the square of the sample length. There was also the need to determine the actual sample length based on the clamping distance. The scale on

the new sample holder was arbitrarily placed just to give a reference point by which to gauge the length. The actual relationship between the scale positions was determined by measuring the deflection of a reference sample for a variety of scale positions. The plot below shows how the maximum deflection depends on the sample length.
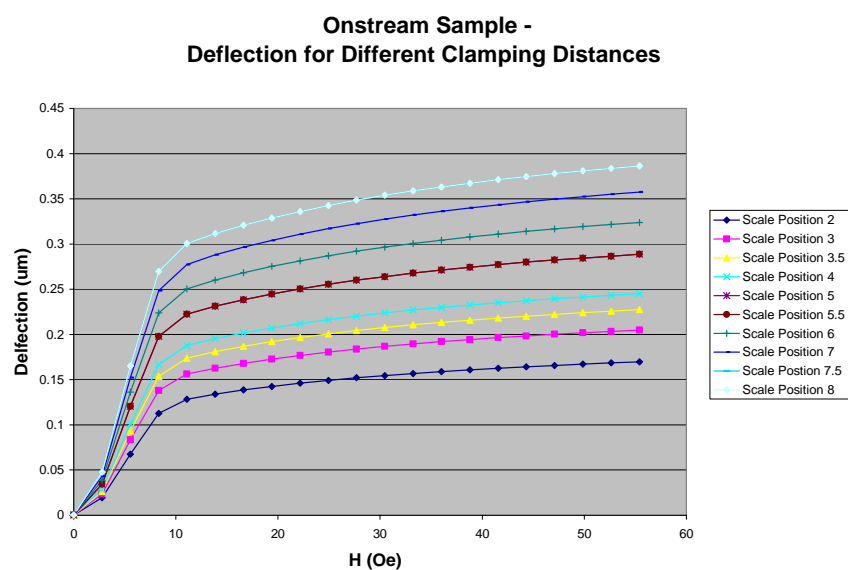
Figure 4.28
Maximum deflection at different scale positions

 Since the measurements were taken at the same field values for each data point, the square root of the maximum deflection at 55.4 Oe was plotted as a function of the scale position.

Square Root of D vs. Scale Position
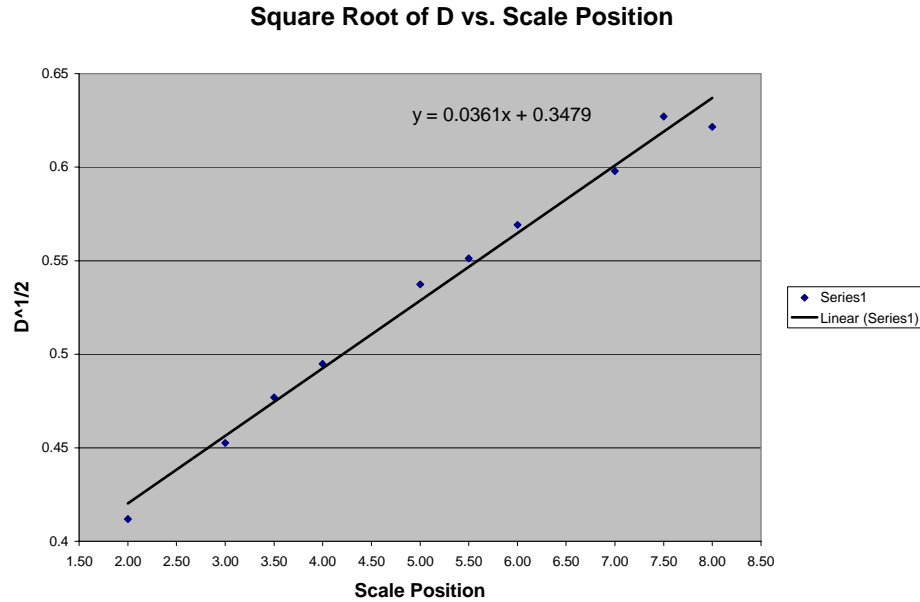
Figure 4.29
Plot of $D^{1/2}$ vs. Scale Position

Since the square root of the deflection is linearly proportional to the effective sample

length, fitting the plot with a linear trend line allows the effective sample length to be

estimated. Assuming the deflection would be zero for a sample length equal to zero, the

x-intercept of the plot would be the scale position for zero deflection. Setting $y = 0$ and

solving for x gives:

$$x = \frac{-0.3479}{0.0361} \approx -9.637$$

This implies that the scale position for (l) and (D) both equal to zero would be -9.637. On

the sample holder scale, there are 2 mm between each integral value, meaning that the

effective sample length (l) would be equal to $(19.274 + 2s)$ mm, where (s) is the position

read from the sample holder scale. This modification was integrated into the LabView

software and the sample length used for the magnetostriction calculations is

automatically determined by entering the scale position for sample length on the control

software front panel.
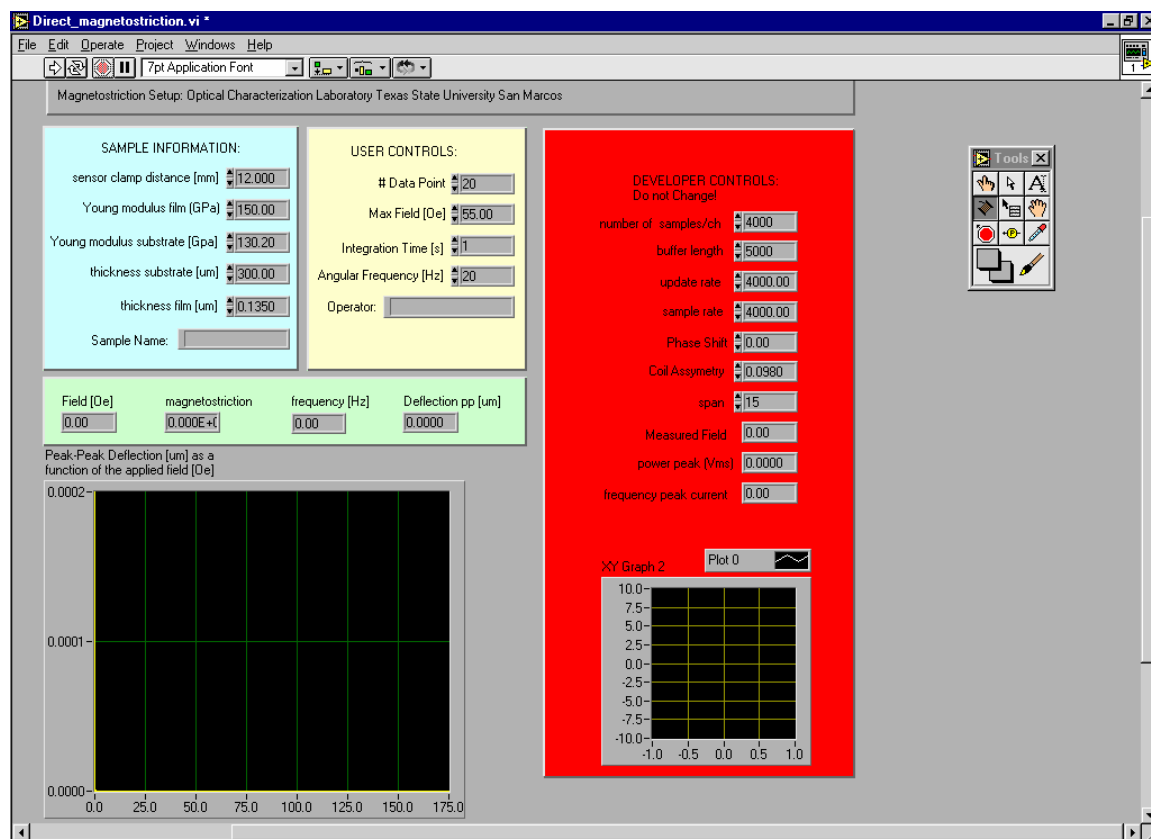
Figure 4.30
LabView front panel for Magnetostrict Program

4.4.4 Capacitance Measurements for Substrate Thickness and Curvature

In addition to the sample length, the thickness of the substrate is also important

for accurate magnetostriction measurements. Previously, the thicknesses of the substrates

were estimated or measured using a regular micrometer. A new method was developed to

more accurately measure the substrate thicknesses using an Agilent 16451B Dielectric

Test Fixture and a 4192A LF Impedance Analyzer. The dielectric test fixture is primarily

used to determine or verify the dielectric constants of materials[24]; however, it was found

that it could be used as a simple thickness monitor.
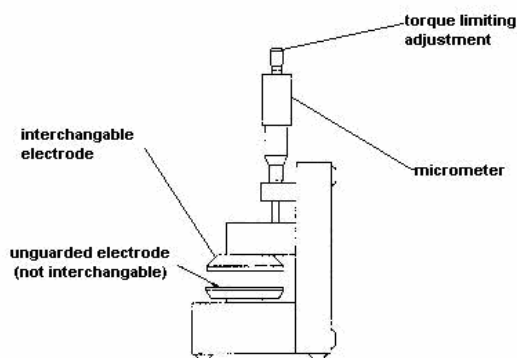
Figure 4.31[24]
Sketch of the Agilent Dielectric Test Fixture

The Agilent 16451B uses two electrodes to form a capacitor. The bottom unguarded

electrode is fixed and is not interchangeable. The top electrode can be interchanged to

select a size appropriate for a given sample. Most of the samples measured in the

magnetostriction setup generally have a width less than 10mm because of the geometry

of the magnetostriction setup sample holder. The 5mm diameter electrode was a suitable

choice for the magnetostriction samples. The dimensions of the unguarded electrode and

the 5 mm electrode are shown in Figure 4.32.
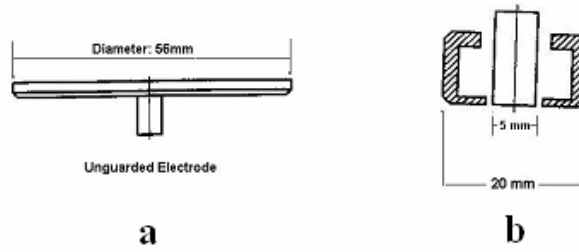
Figure 4.32
Agilent Test fixture electrodes: a) fixed unguarded electrode;
b) interchangeable 5mm guarded electrode[24]

Measuring the capacitance between the test sample and the electrode (C_1) using the impedance analyzer allows the distance between the sample and the electrode to be calculated using Equation (4.34)

$$D_1 = \frac{\varepsilon_0 A}{C_1}$$ (4.34)

where ε_0 is the permittivity of free space and A is the area of the electrode.

Removing the sample and again measuring the capacitance (C_2), allows the distance between the two electrodes (D_2), to be determined via the equation:

$$D_2 = \frac{\varepsilon_0 A}{C_2}$$ (4.35)

The thickness of the sample (T) can then be determined by subtracting D_1 from D_2.

$$T = D_2 - D_1$$ (4.36)

An illustration of the measurement procedure is provided in Figure 4.33.
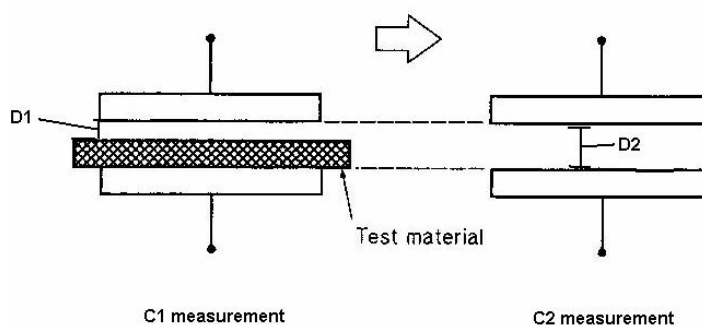
Figure 4.33
Illustration of measurement procedure for C_1 and C_2

The impedance analyzer was used to measure the capacitance between the electrodes for

a wide range of AC frequencies. Initially NiFe45% samples were centered below the 5

mm electrode, and the capacitance was measured and thickness calculated for frequencies

from 100 Hz to 13 MHz. It was noticed that the thickness was dependent on the AC

frequency as indicated from the plot below:
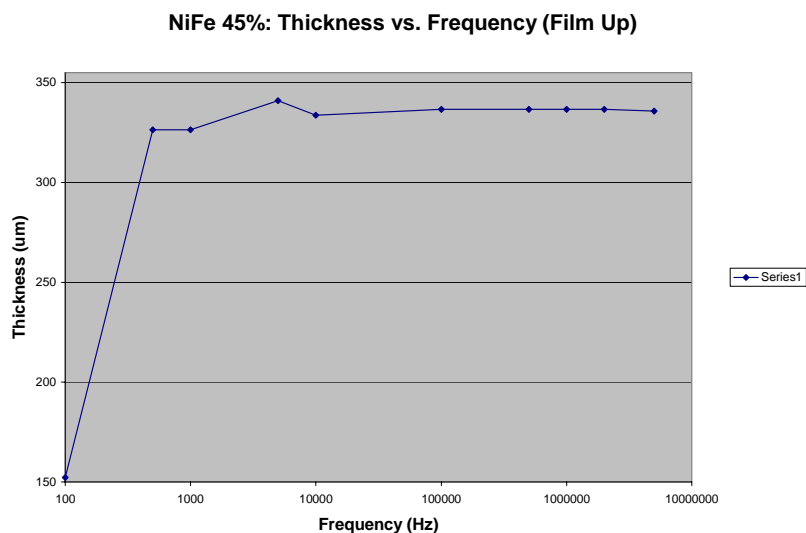
Figure 4.34
Thickness vs. Frequency for NiFe45% sample

Figure 5.16 shows that the measured thickness varies with AC frequency, especially at

the lower (100 Hz to 100 kHz) and upper (> 2MHz) regions of the frequency spectrum,

while the measurements remained relatively constant from 100 kHz to 2 MHz. For the

substrate measurements the thicknesses were calculated for several frequencies in this

ideal measurement range and an average was computed to represent the actual thickness.

In addition to substrate thickness measurements, this technique was also used to

determine the curvature of the samples due to substrate strain induced by film deposition.

Examination of the curvature was proposed when it was observed that slightly different

thicknesses were calculated depending on whether the samples were measured with the

film up or film down, while the thickness measurements were reproducible for each

orientation. The amount of strain induced by the film is directly related to the curvature

of the substrate, and the magnitude of curvature can be gauged by the difference in

measured center thicknesses.

Figure 4.35
Possible orientations of a strained sample

If the thickness is measured in the center of a sample that is convex up, as in Fig

4.35, the calculated thickness will be greater than the actual thickness of the substrate,

whereas if the sample is concave up (Fig 4.35b), the thickness at the center of the sample

is the actual substrate thickness. The difference between the two measurements can be

used to determine the magnitude of strain present on the substrate, and determine whether the strain is compressive or tensile, based on whether the film is up or down during the measurements. For example, if the greater thickness is measured with the film facing down, there is a tensile stress on the film.

The complete measurement data tables for all of the samples measured can be found in Appendix A. The measurement results for two samples are presented in the tables below:

033005#2		
	Film Up	Film Down
Average Capacitance:	4.337E-12	7.805E-12
Average Distance:	40.08567472	22.2743845
Avg thickness:	280.0829648	297.894255
032205#2		
	Film Up	Film Down
Average Capacitance:	3.095E-12	3.7396E-12
Average Distance:	56.17175631	46.4893649
Avg thickness:	273.7925331	283.437335

Table 4.3
Capacitance thickness measurements

CHAPTER 5

MEASUREMENT RESULTS

5.1   VSM Measurements

5.1.1   NiFe35% VSM Measurements

NiFe samples were measured for various orientations with respect to sample geometry and external field intensity (H). The samples were rectangular and the 0 degree measurement was taken with the sample lengthwise between the poles of the electromagnet and the 90 degree measurement was taken with the sample widthwise between the poles. The hysteresis curves for the NiFe35% sample 101901#3 are presented in the figure below:

NiFe35% Sample: 101901#3
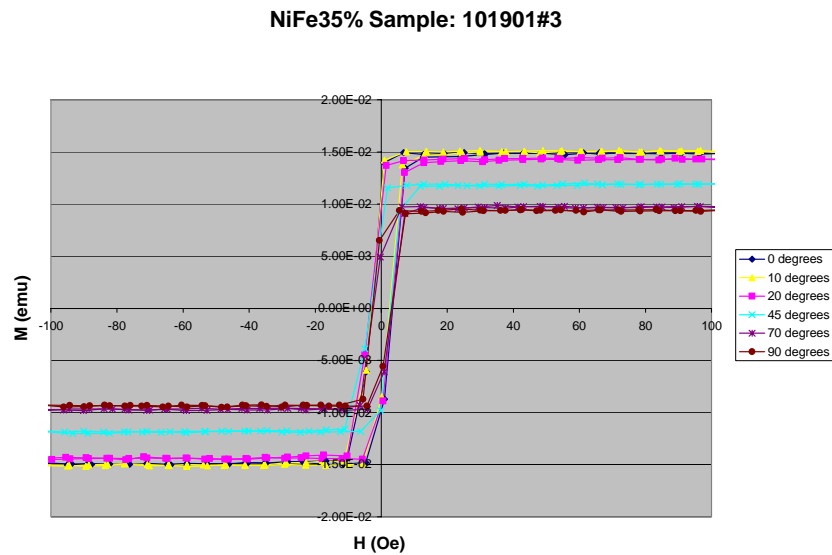
Figure 5.1
VSM measurements: NiFe35% 101901#3

The results of the VSM measurements suggest that the NiFe sample is isotropic because the hysteresis curves are identical for all orientations with the exception of the saturation magnetization. The decrease in saturation magnetization is due to the sample geometry and the measurement technique of the VSM. When the rectangular sample was measured at 0 degrees, the sample was lengthwise between the pickup coils, and the edges were much closer to the coils than when the sample was widthwise between the coils. If the sample is closer to the coils, it will induce a greater EMF resulting in a higher magnetization. The isotropic nature of the samples is seen from the shape of the hysteresis curve, which remains similar as the sample is rotated with respect to the field.

VSM Measurement Results for NiFe35% Sample 101901#3		
Angle (deg)	Hc (Oe)	Hs(Oe)
0	2.9	8
10	2.9	8
20	3.4	8
45	3.25	8
70	2.4	8
90	2.65	8

Table 5.1
VSM measurement results for NiFe35% sample 101901#3

5.1.2 TbFe/FeCo VSM Measurements

TbFe/FeCo samples were also measured using the VSM. The results for sample

033005#2 are presented below:

TbFe/FeCo Sample: 033005#2
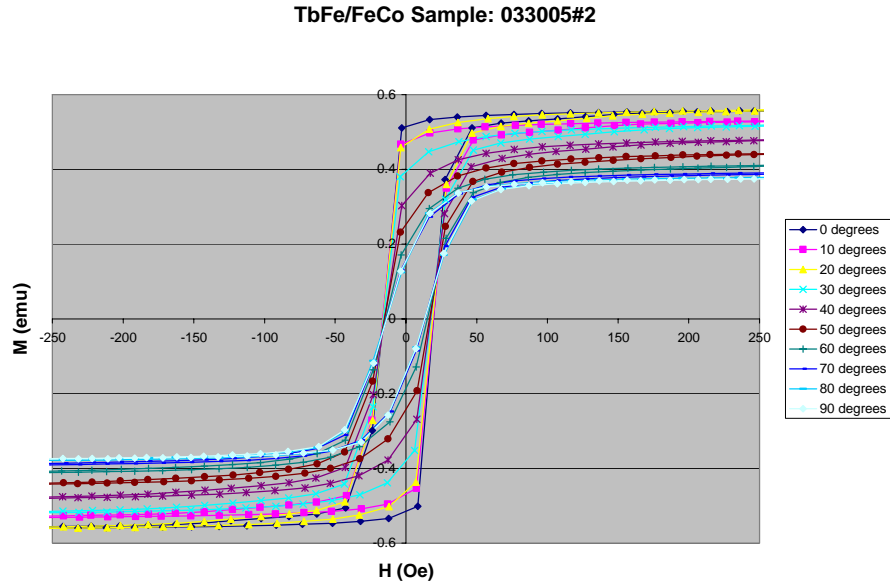
Figure 5.2
VSM hysteresis curves for TbFe/FeCo sample 033005#2
for different sample orientations

VSM Measurement Results for TbFe/FeCo Sample 033005#2		
Angle (deg)	H_c *(Oe)*	H_s*(Oe)*
0	19.4	55
10	19.4	55
20	18.8	55
30	17.5	55
40	17.2	55
50	16.6	55
60	15.1	55
70	13.2	55
80	13.2	55
90	13.2	55

Table 5.2
VSM Measurement Results for TbFe/FeCo Sample 033005#2

The VSM measurements for the multilayer sample suggest that the TbFe/FeCo sample

has a uniaxial anisotropy with an in-plane easy axis along the length of the sample. This

conclusion was based on the apparent change in the shape of the hysteresis curve as the

sample is rotated away from the 0 degree orientation. At 0-20 degrees the hysteresis loop

is generally square shaped, retaining over 85% of its saturation at zero field. As the

sample is rotated farther from its easy axis the magnetic reversal becomes more gradual,

and the sample exhibits a lower remenance, both of which are characteristic of reversal

by rotation of magnetic moments. TbFe/FeCo sample 032205#2 was also measured with

the VSM. The results are given below:

TbFe/FeCo Sample: 032205#2
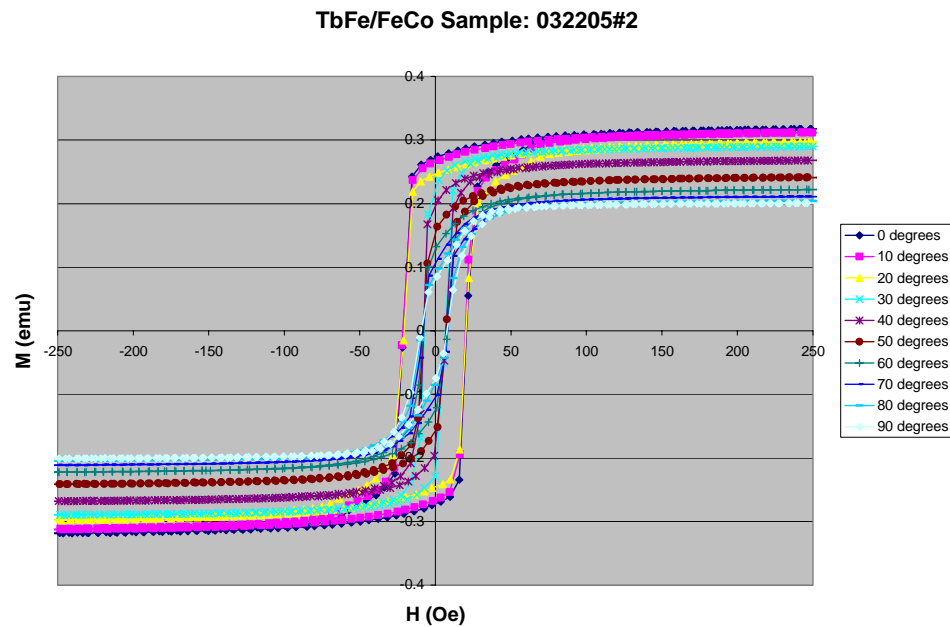
Figure 5.3
VSM hysteresis curves for TbFe/FeCo sample 032205#2
for different sample orientations

Sample 032205#5 is also believed to exhibit a uniaxial anisotropy with an in plane easy

axis along the length of the sample. This conclusion is based on the change in the

hysteresis curves as the sample is rotated away from its apparent easy axis, behaving

similar to the Sample: 033005#2 previously discussed.

VSM Measurement Results for TbFe/FeCo Sample 032205#2		
Angle (deg)	Hc (Oe)	Hs(Oe)
0	20.6	55
10	19.9	55
20	20.4	55
30	6.5	55
40	6.9	55
50	7.1	55
60	7.9	55
70	8	55
80	8.1	55

Table 5.3
VSM measurement results for TbFe/FeCo sample 032205#2

5.2   Kerr Tracer Measurements

5.2.1   NiFe35% Kerr Tracer Measurements

Kerr hysteresis measurements were taken for NiFe35% sample: 101901#3 at different

orientations of the applied field. The 0-degree orientation referred to the sample placed

lengthwise between the poles of the electromagnet, and 90-degrees widthwise between

the poles. The measurements results are presented below:

NiFe35% Sample: 101901#3
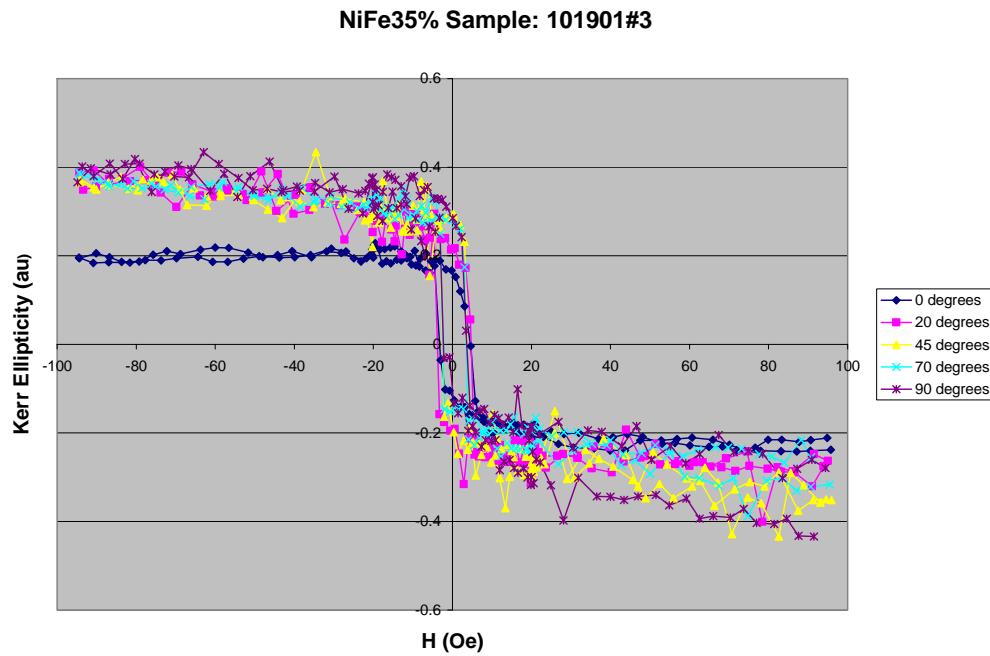
Figure 5.4
Kerr hysteresis curves for 101901#3

The Kerr hysteresis curves measured for NiFe sample: 101901#3 closely resemble the

VSM measurements of the same sample. Here, the difference in Kerr Ellipticity is the

result of adjusting the signal on the LIA. Both measurements suggest the NiFe35%

samples are isotropic on the film surface, preferring no specific magnetocrystalline axis.

Literature supports the isotropic nature of (111) fcc polycrystalline NiFe films[17].

Kerr Tracer Measurement Results for NiFe35% Sample 101901#3		
Angle (deg)	Hc (Oe)	Hs(Oe)
0	4.6	8
20	4.7	8
45	3.7	8
70	3.4	8
90	3.7	8

Table 5.4
Kerr Tracer measurement results for NiFe35% sample 101901#3

5.2.2 TbFe/FeCo Kerr Tracer Measurements

Kerr hysteresis measurements were taken for the TbFe/FeCo multilayers in the same manner as the NiFe sample. The hysteresis curves for the sample: 032205#2 are shown below:
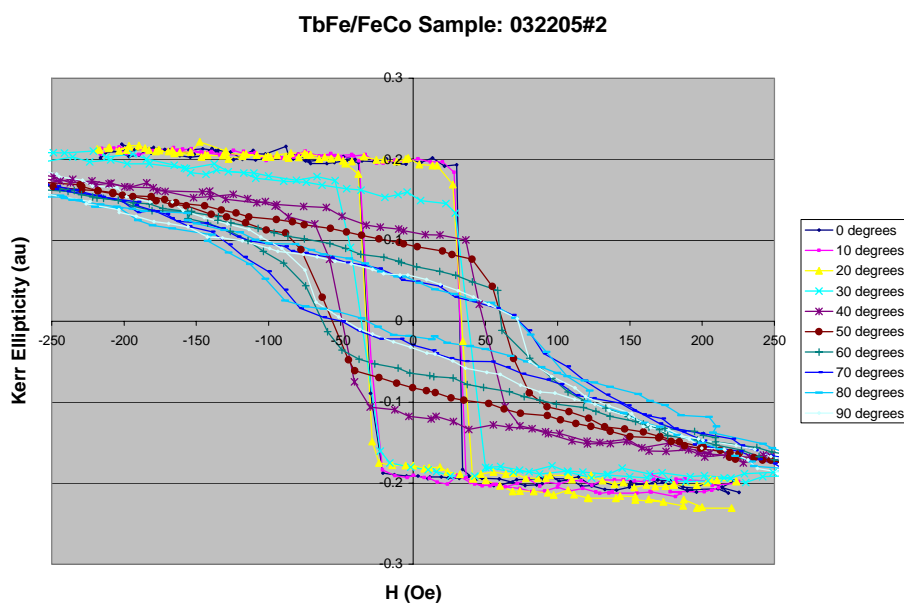
Figure 5.5
Kerr hysteresis measurements TbFe/FeCo sample: 032205#2

The hysteresis curves of the TbFe/FeCo samples suggest an in-plane uniaxial anisotropy with an easy axis along the length of the sample. Figure 5.5 shows that the magnetic

reversal mechanism is strongly dependent on the direction of the applied field. For 0

degrees, the sample was placed lengthwise between the poles of the magnet, and the field

was along the length of the sample. The curves measured for 0, 10, and 20 degrees, show

magnetization dominated by domain wall motion, indicated by the sharp reversal

resulting in square-shaped hysteresis loops. Another indicator of the domain wall motion

is the relatively high remenance. The magnetic properties at low angles suggest that an

in-plane easy axis lies generally along the length of the sample. As the length of the

sample is rotated to higher angles with respect to the field direction, the domain wall

motion becomes less apparent, and it seems that the reversal mechanism is changing. The

initially sharp domain wall transition between saturation states becomes more gradual as

the angle increases, suggesting that the reversal is occurring by rotation of magnetic

moments. The remenance also decreases as the angle increases, which is characteristic of

reversal by rotation of magnetic moments. As the moments are rotated away from their

easy axis, they do so at a cost in anisotropy energy, and as the field decreases and

approaches zero, the moments rotate back to their initial directions and the spontaneous

magnetization decreases back to its value before the application of the field. There also

seems to be a high anisotropy constant for the TbFe/FeCo multilayers, because for higher

orientation angles, the sample no longer saturates as it does for small angles. The

coercivity also seems to be dependent on the direction of the field. The coercivity and

saturation fields vs. angle for several TbFe/FeCo samples are listed in Table 5.5.

Coercivity (Hc) and Saturation (Hs) Data for Measured TbFe/FeCo Samples

032205#2			040205#1			032805#2		
Angle (deg)	**Hc (Oe)**	**Hs (Oe)**	**Angle (deg)**	**Hc (Oe)**	**Hs (Oe)**	**Angle (deg)**	**Hc (Oe)**	**Hs (Oe)**
0	32	39	0	13	40	0	9.5	43
10	32.5	40	45	24	70	45	10.25	20
20	34	40	90	---	---	90	---	---
30	38	50	135	17	30	135	15.25	40
40	49	---	180	13	---	180	14.5	70
50	62	---	**033105#1**					
60	63	---	**Angle (deg)**	**Hc (Oe)**	**Hs (Oe)**			
70	73	---	0	8.5	17			
80	---	---	45	14.5	32			
90	---	---	90	---	---			
130	38	---	135	8.5	14			

Table 5.5
Kerr Tracer measurement results for TbFe/FeCo multilayers

TbFe/FeCo Sample: 032205#2
Coercivity vs. Angle
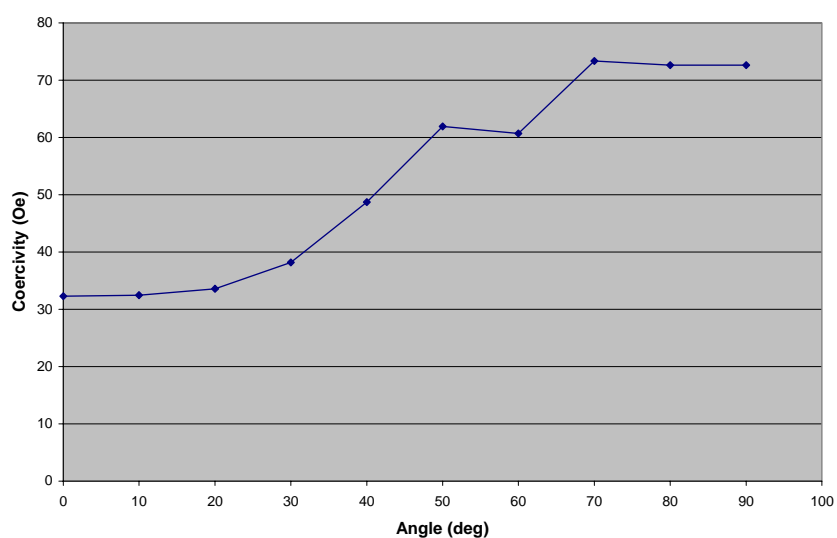
Figure 5.6
Coercivity vs. Angle for 032205#2

Figure 5.6 is a plot of the coercivity vs. angle for several orientations of the sample. It can be seen that the coercivity generally increases as the angle increases, a trend that is present for all of the TbFe/FeCo samples measured with the Kerr Tracer.

5.3   Domain Analysis

5.3.1 NiFe45% Domain Scans

The experimental procedure for mapping the domains of the NiFe45% sample

102701#2 using the Scanning Kerr Microscope involved bringing the sample to positive

saturation at 50 gauss and taking a surface scan in saturation. The field was then stepped

down to zero slowly (2 gauss steps), and then to -4 gauss in 1 gauss field steps. Scans

were then taken at every 0.25 gauss from -4 to -10 gauss. This range contained the entire

magnetic reversal process and was determined by a Kerr Tracer hysteresis curve

generated prior to the scans. 200 lines were scanned, with a 5 micron space between scan

lines. The lines were 1mm long with 250 samples per line. The total area scanned was

1mm x 1mm.The domain images for NiFe45% 102701#2 are given in Figure 5.7.
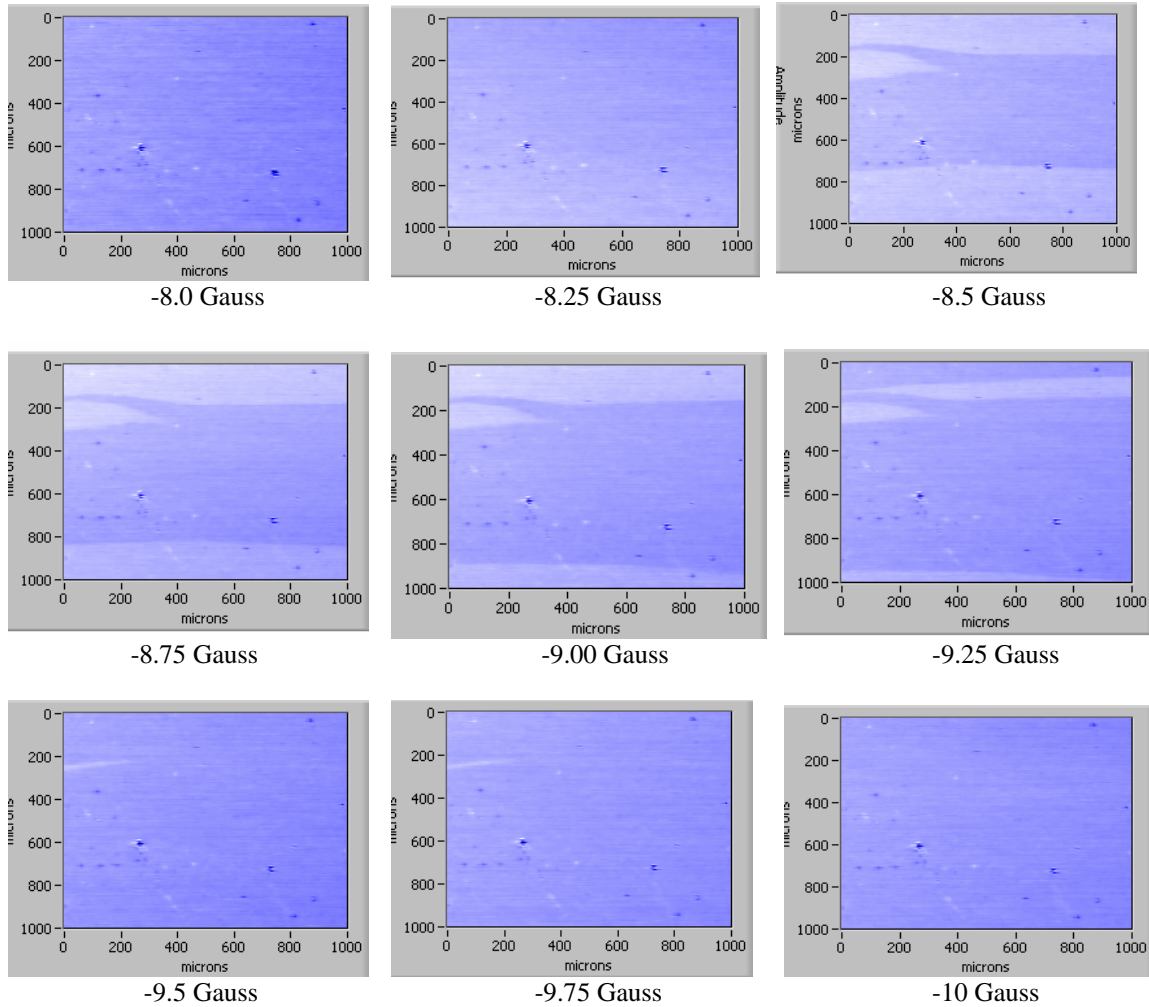
Figure 5.7
Magnetic reversal of NiFe45% sample: 102701#2

It is clear from Figure 5.7 that the magnetic reversal of this sample takes place by domain wall motion. As the field decreases, the motion of the domain wall is clearly visible as the domains oriented in the direction of the field grow at the expense of unfavorably oriented domains, until the sample reaches saturation.

5.3.2 TbFe/FeCo Multilayer Domain Scans

Domain images were obtained for TbFe/FeCo Sample: 032805#2. The samples

were first taken to negative saturation and the field was stepped up to 8.8 Gauss. Scans

were then taken at 0.25 Gauss steps up to 10.6 Gauss. For this sample, a larger area was

scanned. The scan dimensions were 4mm x 2mm. The results are given in Figure 5.8.
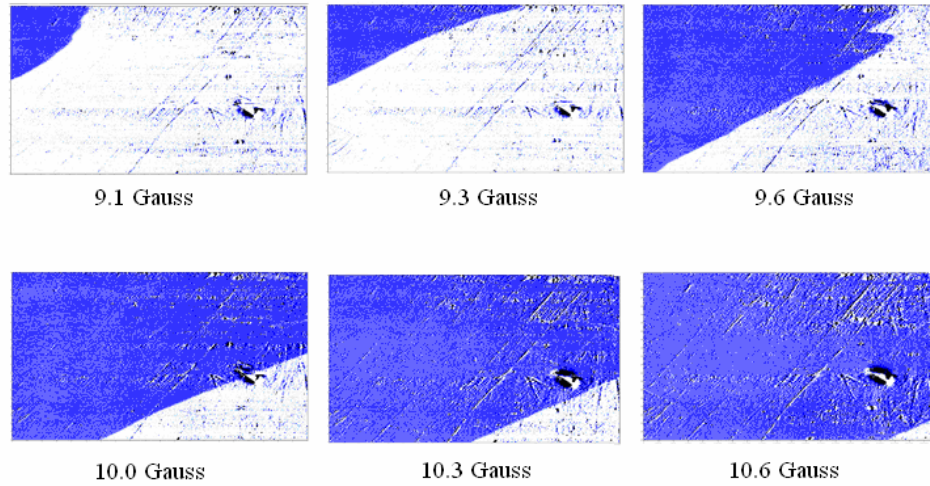
Figure 5.8
Magnetic reversal of TbFe/FeCo sample 032805#2

The contrast of the domain scans in figure 5.8 was enhanced using the *results analyzer*

program written in LabView by Vincent Sombroek. The *results analyzer* has several

useful options to analyze domain scans (see Appendix C). Among these options is the

ability to subtract saturation images from transition scans to increase the contrast of the

domains as done in the scans in fig. 5.8. The domain images for this sample again show

magnetic reversal by domain wall motion. The domain wall can be observed as it moves

from the bottom right corner of the scan area to the upper left corner of the scan area.

5.4   Magnetostriction Measurements

5.4.1   NiFe35% Magnetostriction Measurements

The magnetostriction measurement results for the NiFe35% samples are given

below:
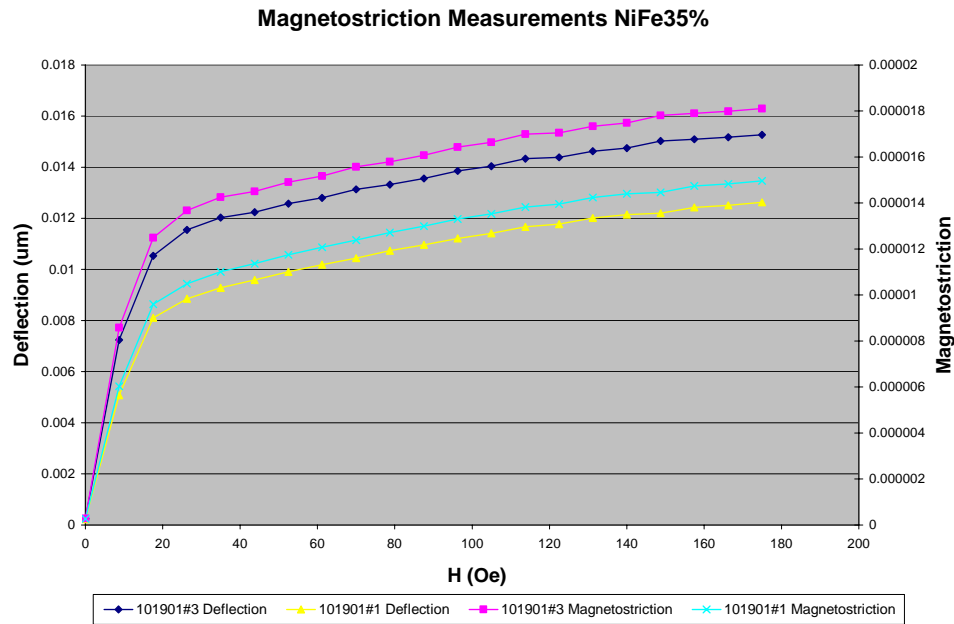
Figure 5.9
Magnetostriction measurements for NiFe35% samples

The Magnetostriction (λ) vs. H plots above were for the two NiFe 35% samples having

the largest magnetostriction: 101901#3 (99.9nm) and 101901#1 (522nm). The left axis is

the maximum deflection measured at field value, and the right axis is the

magnetostriction for the same samples as computed by the LabView program using Eq.

(4.33). Literature suggests[32] saturation magnetostrictions (λ_s) for NiFe35% alloy to be in

the range of 1.08×10^{-5} to 1.47×10^{-5}, in fair agreement with the measurement results.

Overall, the magnetostriction for the NiFe samples was relatively low, as expected for

NiFe, because magnetostriction is an undesirable quality in the primary industrial

applications for NiFe films such as read/write heads and magnetic recording media.

Saturation Magnetostriction and Saturation Magnetization for NiFe		
<u>% Ni</u>	$\underline{\lambda_s}$	<u>M_s (kA/m)</u>
75.1	7.28×10^{-6}	896.52
73	6.97×10^{-6}	922.31
72.4	7.53×10^{-6}	929.68
70.9	8.57×10^{-6}	948.11
70.7	1.08×10^{-5}	950.57
61.9	1.47×10^{-5}	1058.7

Table 5.6
Saturation magnetostriction and saturation magnetization
for NiFe alloy with different Ni %[32]

5.4.2   Single Layer TbFe Magnetostriction Measurements

Magnetostriction measurements were done on single layers of TbFe alloy. The D vs. H

Plot of sample 022305#2 is shown in Figure 5.10.
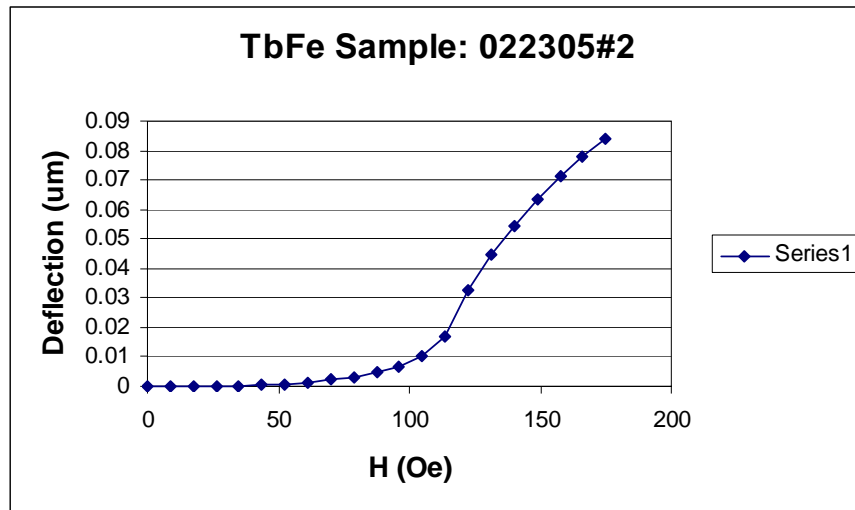
Figure 5.10
Magnetostriction measurement of TbFe sample

The maximum applicable field of 170 Oe was not sufficient to saturate the FeTb layers.

This sample has a VSM coercivity of 180 Oe, a saturation field of 2093 Oe, and a

thickness of 1.2 um. The low field behavior is inherent to a rotation of the magnetization within the material. The high field behavior is originating from the saturation of the magnetization parallel to the applied field that will occur at higher fields.

5.4.3   TbFe/FeCo Magnetostriction Measurements

The magnetostriction of the TbFe/FeCo Multilayers was roughly one order of magnitude higher than that measured for the NiFe samples. Measurement results for the four multilayers having the largest magnetostriction are given below:

Magnetostriction: TbFe/FeCo Samples
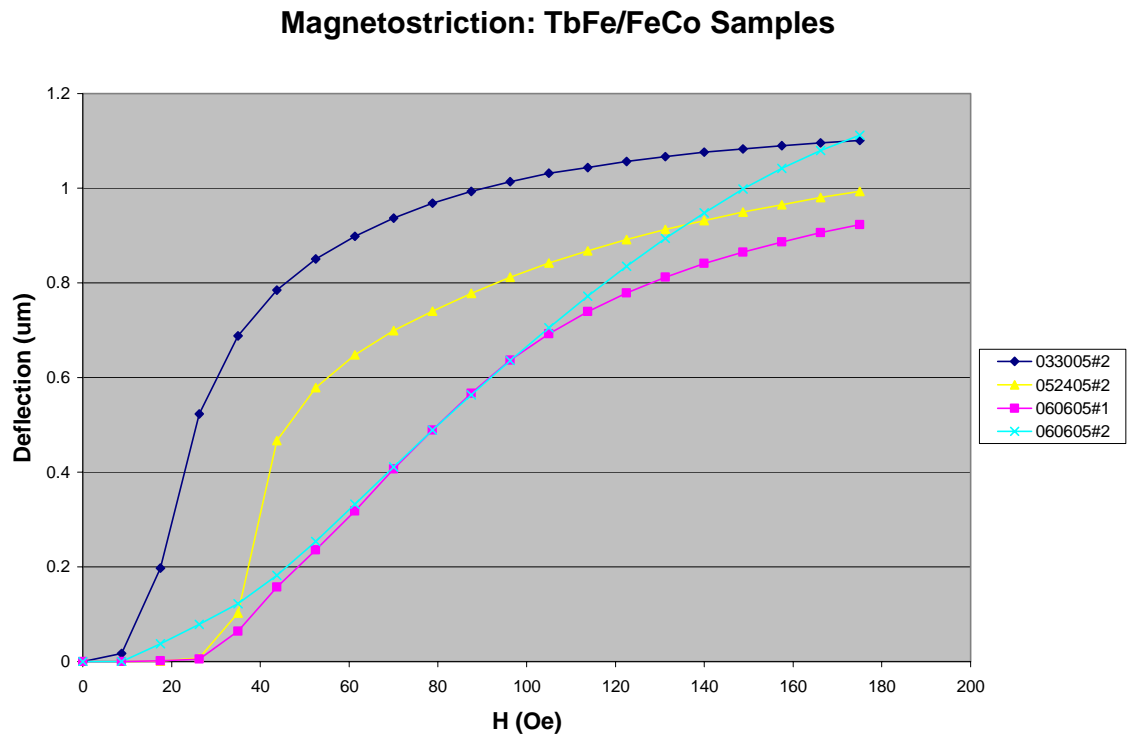
Figure 5.11
Magnetostriction measurements for TbFe/FeCo multilayers

It is clear from Figure 5.11 that while the four samples have a large magnetostriction, the behavior of the individual samples varies considerably. The samples 033005#2 (Spring

series) and 052405#2 (Summer Series) exhibit a large magnetostriction at low fields, indicated by the sharp increases in the magnitude of deflection between measurement points up to ~50 Oe, after which it appears the sample is approaching saturation. In contrast, the magnetostriction of sample 060605# 1 increases more gradually than the previous two samples, and begins to approach saturation at higher fields (~110 Oe). The magnetostriction of sample 060605#2 also increases gradually but shows no signs of saturating, even at the maximum applicable field. For the intended applications of the films, it is clear that the best candidate would be 033005#2, exhibiting a very large magnetostriction, and saturating at relatively low fields. In addition to the high magnetostriction at relatively low fields, VSM data shows 033005#2 to have a coercivity of 19 Oe along the easy axis, another property making it suitable for the specified application.

The table below shows the coercivities as measured by VSM and the field at which the samples begin to show significant magnetostriction (H_i). In addition to the low and high field behavior there seems to be a minimum value of the magnetic field under which the sample does not show any magnetostriction.

Sample	Hc (VSM)	H_i (λ–setup)	Saturated?
033105#1	7/13 Oe		No
031505#3		7.7 Oe	Yes
031705#1	14-17 Oe	8.8 Oe	No
031705#2	91-92 Oe	59 Oe	Almost
031805	38-49 Oe	62 Oe	No
032105#2	16-21 Oe	8.7 Oe	Almost
032105#1	13 Oe	20.9 Oe	No
032205#1	37-38 Oe	9.3 Oe	No
032205#2	12-30 Oe	14.2 Oe	No
032805#1	8.7 Oe	46.5 Oe	No
032805-2	9-11 Oe	10.6 Oe	Almost
032905#1	15-20 Oe	30.2 Oe	No
033005#2	19 Oe	14.9 Oe	Yes
040205#1	12/11 Oe	13.6 Oe	No

Table 5.7
Magnetostriction results for TbFe/FeCo spring samples

The summer series samples were easier to saturate. Some of them had a clear jump below 50 Oe but still showed a slope at high fields (150 Oe). Two samples showed two bending points at low fields (H_{i1} and H_{i2}). An example is shown in Figure 5.12 which shows the magnetostriction curve of sample 06092005#1.
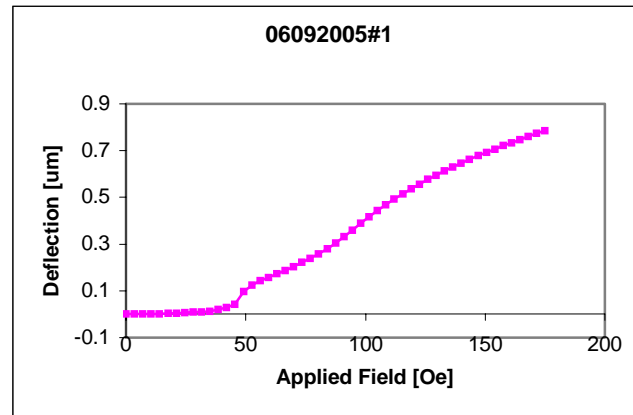
Figure 5.12
D vs. H curve for 06092005#1

Sample	Hc (VSM)	H_{i1}	H_{i2}	Comments
05242005#2		33.7 Oe		High H slope
06062005#1		42.3 Oe		almost sat
06092005#1		43.8 Oe	66.5 Oe	Not saturated
06082005#2		13.5 Oe		Not saturated
06072005#1	40 Oe	15.4 Oe	23.4 Oe	Not saturated
06062005#2		29.2 Oe		Not saturated
06022005#2		66.5 Oe		Not saturated
06012005#2		12.8 Oe		High H slope
05262005#2		12.5 Oe		Saturated
05262005#1	17.8 Oe	18.8 Oe		High H slope
05252005#2		12 Oe		Saturated
05232005toolrun		52 Oe		High H slope

Table 5.8
Magnetostriction results for TbFe/FeCo summer samples

The figure and table below show the magnetostriction for the samples that could be saturated at 170 Oe. The magnetostriction was calculated using equation (4.33) assuming: $v_f=0$, $E_f=50$ GPa, $E_s=130.2$ GPa, and $v_s=0.266$.

Deflection for Saturated Samples
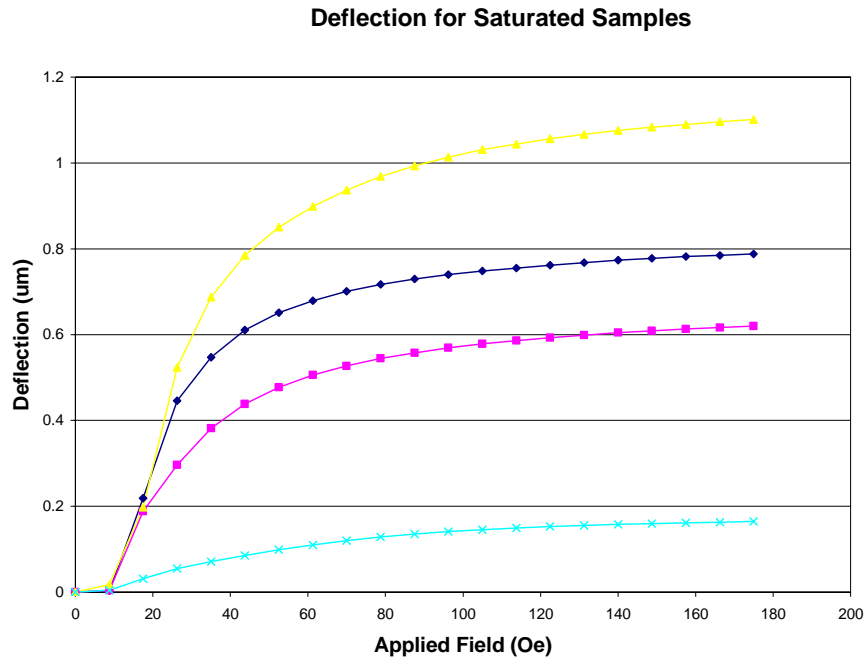
Figure 5.13
D vs. H plots for saturated samples

sample	Deflection @170Oe	λ_s	TbFe Thickness	Film Thickness
031505#3	164.3 nm	289E-6	7*40=280 nm	135 nm
033005#2	1101.2 nm	376E-6	9*160=1440 nm	135 nm
05262005#2	619.6 nm	203E-6	15*100=1500 nm	1500 nm
05252005#2	788.1 nm	257E-6	10*150=1500 nm	1500 nm

Table 5.9
Saturation Magnetostriction for saturated samples

CHAPTER 6

CONCLUSIONS

To conclude, the research conducted proved successful in characterizing the materials investigated. Based on the hysteresis measurements by both VSM and Kerr Tracer, the isotropic nature of the NiFe Samples was revealed. In addition, domain analysis revealed domain patterns in the NiFe samples and allowed the observation of the domain wall motion. Also, magnetoelastic characterization done using the magnetostriction setup was found to be in reasonable agreement with published literature for the saturation magnetostriction for NiFe.

The TbFe/FeCo samples produced results that were not so easily understood. Comparison between the VSM measurements and Kerr Tracer results for TbFe/FeCo Sample: 032205#2 show a discrepancy in the angle dependence of the coercivity. VSM measurements show a decrease in coercivity with an increase in angle. The Kerr Tracer measurements show that the coercivity increases as the sample is rotated with respect to the applied field. It is not clear why the results differ, but one possibility is the difference in the measurement techniques. The VSM measures an average magnetization of the entire sample at a given field. In contrast, the Kerr Tracer measures only the magnetization of the area of the sample directly under the laser spot, and only at the surface of the sample. Hence, if the reversal was not homogeneous everywhere in the

film, differences in the measurement results would be expected. For instance, scratches and defects on the sample surface could likely cause pinning of the domain walls resulting in the higher coercivities measured with the Kerr Tracer. The differences in the measurement results may also be attributed to stress in the film. Capacitance measurements for sample 032205#2 suggest that the film has a residual tensile stress. The magnitude of the stress (σ) was calculated using the Stoney Equation[34], Equation (6.1), which relates the stress of the film to the curvature imposed on the substrate.

$$\sigma = \frac{E_s t_s^2}{6t_f} \frac{1}{R} \qquad (6.1)$$

where E_s is the Young's Modulus of the substrate, and t_s and t_f are the thicknesses of the substrate and film, respectively, and (R) is the radius of curvature of the substrate. The value for (R) was determined from the capacitance measurements.
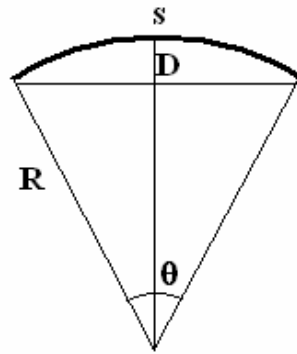
Figure 6.1
Schematic for determining radius of curvature

Figure 6.1 schematically shows how the capacitance measurements were used to determine the radius of curvature of the substrate. The curved substrate forms an arc (s) with a length equal to the length of the sample. The difference in measured thickness for

the film up and film down gives (D), as indicated in Figure 6.1. Since $s = R\theta$ and

$\cos\frac{\theta}{2} = \dfrac{R - D}{R}$, (R) can be found by the equation:

$$\cos\left(\frac{s}{2R}\right) = \frac{R - D}{R} \tag{6.2}$$

Equation (6.2) is a transcendental equation, and the solution must be determined

numerically. Mathematica was used to approximate the radius of curvature using

Equation 6.2. The results for samples 032205#2 and 033005#2 are given in table 6.1,

using $E_s = 130.2$ GPa.

Residual Stress on TbFe/FeCo Films					
Sample	R (cm)	D (um)	t_s (um)	t_f (um)	σ (MPa)
032205#2	654.022	9.645	273.793	2.24	111.036
033005#2	280.725	17.811	280.083	2.93	207.909

Table 6.1
Residual stress on TbFe/FeCo films

For the VSM measurements, the sample was attached to the sample holder using

rubber cement, so it was assumed that the only stress on the film was the residual stress.

For the Kerr tracer measurements, the sample was clamped on the ends using copper

blade springs which would have increased the tensile stress on the film. The increased

coercivities in the Kerr tracer measurements may be attributed to the increased stress

induced by clamping the sample on the ends.

The uniaxial anisotropy observed in the TbFe/FeCo samples can be the result of

either the shape of the sample or the stress, or both. Shape anisotropy in a thin film is the

preference for the magnetization in a given direction of a sample based on its shape. The

shape anisotropy field (H_{shape}) is directly proportional to the difference in

demagnetization fields in two orthogonal directions[35]. The shape anisotropy field is quantified in Equation 6.3.

$$H_{shape} = M_s(N_W - N_L) = M_s \Delta N \qquad (6.3)$$

where N_W and N_L are the demagnetizing factors along the width and length of the samples, respectively. The values of the demagnetizing factors can be determined by:

$$N_W = \frac{2t_f}{\pi W} \qquad (6.4)$$

and

$$N_L = \frac{2t_f}{\pi L} \qquad (6.5)$$

where (W) is the sample width, (L) is the sample length, and t_f is the film thickness. Since the samples measured had dimensions of L = 20mm and W = 5mm, there should certainly be a contribution to the anisotropy resulting from the sample shape. The anisotropy of the samples may also be the resulting from the stress on the film. Stress induced anisotropy H_a^{eff} can be calculated using Equation (6.6).

$$H_a^{eff} = H_a - \frac{3\lambda_s \sigma}{M_s} \qquad (6.6)$$

where H_a is the anisotropy field, λ_s is the saturation magnetostriction, σ is the stress on the film, and M_s is the saturation magnetization. Normally, tension in a positive magnetostriction material facilitates magnetization in the tensile direction[35]. This is in agreement with the easy direction observed in the samples. The tensile strain was along the length of the sample, the same direction as the easy axis, suggesting there was also a contribution to the anisotropy for the residual strain.

Magnetostriction measurements for the TbFe/FeCo samples revealed several samples that had desirable qualities for the intended application, namely a large magnetostriction (λ_s) and large λ_s/H_s ratio, and also a low coercivity.

In addition to the magnetic and magnetoelastic characterization of the NiFe and TbFe/FeCo samples, the research was also successful in facilitating the improvement and optimization of the measurement equipment. The magnetostriction measurement system received a Fotonic Sensor upgrade resulting in increased the sensitivity and power supplies that allowed higher achievable fields. Also, methods were developed for varying and accurately determining the sample length, as well as measuring the thickness and curvature of the samples. The Kerr Tracer and Scanning Kerr Microscope both received new control software, improved field setting resolution, and a more robust setup that is less sensitive to beam alignment variations. The new control software is very user friendly and is simple enough for an undergraduate to operate. Finally, through the use of an infinity corrected objective, the resolution of the scanning Kerr microscope was improved to ~3μm, a resolution that is comparable to high end commercially available Kerr magnetometers. The only known improvement needed at this point is the possible implementation of a Faraday isolator to prevent back reflection into the laser resulting from the beam reflecting from the objective (it has no Anti-Reflection coating).

APPENDICES

Appendix A: Sample Characteristics and Measurement Data

NiFe Samples

Sample ID	Sputter Time	Composition	M (emu)	H (Oe)	Estimated Thickness (nm)
102601-03	2:36	NiFe-35%	2.75×10^{-2}	2.94	51.54
102601-02	3:56	NiFe-35%	3.98×10^{-2}	1.95	74.59
102601-04	5:55	NiFe-35%	5.797×10^{-2}	2.90	108.6
102501-03	8:35	NiFe-35%	9.025×10^{-2}	1.621	169.1
102501-01	13:20	NiFe-35%	13.14×10^{-2}	1.22	246.3
102501-04	20:00	NiFe-35%	21.95×10^{-2}	0.7095	411.4
102501-02	30:00	NiFe-35%	29.26×10^{-2}	0.545	548.4
102601-01	46:24	NiFe-35%	45.76×10^{-2}	0.488	857.6
102801-04	2:36	NiFe-45%	2.39×10^{-2}	15.14	39.42
102801-01	3:56	NiFe-45%	3.67×10^{-2}	22.65	60.53
102801-02	5:55	NiFe-45%	5.684×10^{-2}	13.95	93.76
102701-01	16:30	NiFe-45%	17.48×10^{-2}	2.26	288.3
102701-04	21:00	NiFe-45%	24.10×10^{-2}	1.26	397.5
102701-03	31:00	NiFe-45%	35.01×10^{-2}	1.32	577.5
102701-02	46:00	NiFe-45%	48.74×10^{-2}	4.14	803.4

Table A-1
NiFe sample characteristics

Sample ID	Sputter Time (min:sec)	Film Thickness
101601-02	12:31	225.3 nm
101901-01	29:00	522 nm
101901-03	5:33	99.9 nm
101701-03	7:30	135 nm
101901-02	5:33	100 nm
101701-04	7:30	135 nm

Table A-2
NiFe sample characteristics(2)

TbFe/FeCo Samples

	Multilayer Depositions							
ID#	**Substrate**	**Tot Press**	**Base Press**	**Flow**	**Repeat#**	**Pre-Sput**	**Ti Sputter**	
		(mtorr)	(torr)	(sccm)		(min)	Seed	Cap
40205(#1)	Alp/K/G/Si	2	4.50E-08	67.00	160x	3	Get	30s
33105(#1)	Alp/K/G/Si	0.5(IG)	8.60E-08	24.00	320x	3	Get	30s
33105(#2)	Ti(1x1 cm)	0.5(IG)	7.20E-07	24.00	80x	3	Get	30s
33005(#1)	Alp/K/G/Si	0.5(IG)	7.50E-08	24.00	170x	3	Get	30s
33005(#2)	Alp/K/G/Si	0.5(IG)	6.00E-07	24.00	160x	3	Get	30s
32905(#1)	Alp/K/G/Si	3	8.50E-08	85.00	160x	3	Get	30s
32805(#1)	Alp/K/G/Si	2	6.20E-07	67.00	160x	3	Get	30s
32805(#2)	Alp/K/G/Si					3	Get	30s
32505(#1)	Alp/K/G/Si	0.3	9.40E-07	14.4-16	160x	3	Get	30s
32305(#1)	Alp/K/G/Si	0.3 (IG)	6.00E-07	15.30	160x	3	Get	30s
32205(#2)	Alp/K/G/Si	0.3 (IG)	7.00E-07	15.30	160x	2	Get	30s
32205(#1)	Alp/K/G/Si	0.3 (IG)	8.90E-08	14.50	160x	2	Get	30s
32105(#2)	Alp/K/G/Si	0.5 (IG)	6.10E-07	24.10	160x	2	Get	30s
32105(#1)	Alp/K/G/Si	0.5 (IG)	5.00E-08	1.80	160x	2	Get	30s
31805	Alp/K/G/Si	0.5 (IG)	8.70E-08	1.80	50x *	2		
31705(#2)	Alp/K/G/Si	0.5 (IG)	4.50E-07	2.00	160x	2	Get	30s
31705(#1)	Alp/K/G/Si	3	7.50E-08	4.50	160x	2	Get	30s
31605	Alp/K/G/Si	0.5 (IG)	9.30E-08	1.8-2.1	80x	2	Get	30s
31505	Alp/K/G/Si	0.5(IG)		?	40x			
31105	Alp/K/G/Si	0.32(IG)		20.00		2		30s

Table A-3
TbFe/FeCo sample sputtering parameters (spring series)

ID#	Substrate	Soft Layer					
		Thickness (sec (nm))			Voltage	Power	AOI
		Fe	Fe-Co	Fe-Co-V	(V)	(W)	(deg)
40205(#1)	Alp/K/G/Si		9(11)		402	390	0
33105(#1)	Alp/K/G/Si		5(5)		463	390	0
33105(#2)	Ti(1x1 cm)		6(7)		479	390	0
33005(#1)	Alp/K/G/Si		5(5)		457	390	0
33005(#2)	Alp/K/G/Si		14(15)		466	390	0
32905(#1)	Alp/K/G/Si		9(11)		383	390	0
32805(#1)	Alp/K/G/Si		9(11)		401	390	0
32805(#2)	Alp/K/G/Si					390	0
32505(#1)	Alp/K/G/Si		8(9)		528	390	0
32305(#1)	Alp/K/G/Si		8(9)		516	390	0
32205(#2)	Alp/K/G/Si		8(9)		504	390	0
32205(#1)	Alp/K/G/Si		6(7)		523	390	0
32105(#2)	Alp/K/G/Si		10(11)		468	390	0
32105(#1)	Alp/K/G/Si		10(11)		462	390	0
31805	Alp/K/G/Si		10(11)				0
31705(#2)	Alp/K/G/Si		8(9)		438	390	0
31705(#1)	Alp/K/G/Si		9(9)		384	390	0
31605	Alp/K/G/Si		9(9)		471	390	0
31505	Alp/K/G/Si		9(9)				0
31105	Alp/K/G/Si		9(9)		507	390	0

Table A-4
TbFe/FeCo samples - soft layer (FeCo) (spring series)

ID#	Substrate	Hard (Fe-Tb) Layer					
		Tile	Thick	Voltage	Power	RF Bias	AOI
		(dia-in)	sec(nm)	(V)	(W)	V (W)	(deg)
40205(#1)	Alp/K/G/Si	2.5"Fe	4(5)	241	420	190(38)	0
33105(#1)	Alp/K/G/Si	2.5"Fe	3(3)	268	420	160(26)	0
33105(#2)	Ti(1x1 cm)	2.5"Fe	4(4)	271	420	160(30)	0
33005(#1)	Alp/K/G/Si	2.5"Fe	3(3)	267	420	160(26)	0
33005(#2)	Alp/K/G/Si	2.5"Fe	10(9)	272	420	160(26)	0
32905(#1)	Alp/K/G/Si	2.5"Fe	4(5)	232	420	190(41)	0
32805(#1)	Alp/K/G/Si	2.5"Fe	4(5)	237	420	190(41)	0
32805(#2)	Alp/K/G/Si	2.5"Fe			420		0
32505(#1)	Alp/K/G/Si	2.5"Fe	3(4)	287	420	130(34)	0
32305(#1)	Alp/K/G/Si	2.5"Fe	7(4)	277	420	120(30)	0
32205(#2)	Alp/K/G/Si	2.5"Fe	4(4)	275	420	N+	0
32205(#1)	Alp/K/G/Si	2.5"Fe	4(4)	273	420	160(33)	0
32105(#2)	Alp/K/G/Si	2.5"Fe	5(5)	252	420	160(33)	0
32105(#1)	Alp/K/G/Si	2.5"Fe	5(5)	247	420	160(20)	0
31805	Alp/K/G/Si	2.5"Fe	5(5)			160(31)	0
31705(#2)	Alp/K/G/Si	2.5"Fe	7(7)	238	420	N	0
31705(#1)	Alp/K/G/Si	2.5"Fe	9(7)	217	420	160(33)	0
31605	Alp/K/G/Si	2.5"Fe	9(7)	234	420	150 (37)	0
31505	Alp/K/G/Si	2.5"Fe	9(7)			140(22)	0
31105	Alp/K/G/Si	2.5"Fe	9(7)	259	240	150(25)	0

Table A-5
TbFe/FeCo samples - hard layer (TbFe) (spring series)

ID#	Substrate	Results			
		Stress	Thickness	Hc	Ms
		(ksi)	(kA)	(Oe)	(emu/cc)
40205(#1)	Alp/K/G/Si		26.3/27.8	12/11	1297/1270
33105(#1)	Alp/K/G/Si		30.7/34.4	7/13	1056/1065
33105(#2)	Ti(1x1 cm)		10.0/10.9	27/38	1030/1070
33005(#1)	Alp/K/G/Si		20.0/16.3	11/10	1011/1010
33005(#2)	Alp/K/G/Si		47.0/43.1	22	1120/1097
32905(#1)	Alp/K/G/Si		27.1	15-20	1177-1274
32805(#1)	Alp/K/G/Si		3.21	19-25	1120-1179
32805(#2)	Alp/K/G/Si		22.5	9-11	1353-1383
32505(#1)	Alp/K/G/Si		20.4	11	1285-1383
32305(#1)	Alp/K/G/Si				
32205(#2)	Alp/K/G/Si		2.93	12-30	1266-1308
32205(#1)	Alp/K/G/Si	Hi C	20.8	37-38	1285-1293
32105(#2)	Alp/K/G/Si	Hi C	11.1	16-21	1579-1661
32105(#1)	Alp/K/G/Si	Mod C	24.7	13	1550-1579
31805	Alp/K/G/Si	Mod C	8.88	38-49	1010-1065
31705(#2)	Alp/K/G/Si	Sl C	27.36	91-92	540-648
31705(#1)	Alp/K/G/Si	Hi C	25.8	14-17	877-999
31605	Alp/K/G/Si	Hi C	18.6	12-14	1140-1227
31505	Alp/K/G/Si		7.66	13-19	1504-1570
31105	Alp/K/G/Si				

Table A-6
TbFe/FeCo samples sputtering results (spring series)

sample ID	ML #	FeCo (sec(nm))	FeTb (sec(nm))	MsS w/mag (mV)	MsS w/o mag (mV)	Total Thickness FeTb [um]
6/9/2005 #1	175X	20(10)	3(7)	103	5	1.225
6/8/2005 #2	175X	20(10)	6(7)	402	12	1.225
6/7/2005 #1	187X	22(10)	4(5)	242	5	0.935
6/6/2005 #2	235X	20(10)	6(7)	220	5	1.645
6/6/2005 #1	150X	20(10)	9(10)	180	5	1.5
6/3/2005 #2	165X	20(10)	6(7)	370	5	
6/3/2005 #1	165X	20(10)	6(7)	241	25	
6/2/2005 #2	165X	20(10)	6(7)	96	16	1.155
6/1/2005	165X	31(15)	8(9)	145	55	1.485
5/27/2005 #2	110X	22(15)	8(9)	NR	NR	
5/27/2005 #1	175X	14(10)	6(7)	NR	NR	
5/26/2005 #2	100X	22(15)	13(15)	NR	NR	1.5
5/26/2005 #1	175X	10(7)	9(10)	NR	NR	1.75
5/25/2005 #2	150X	14(10)	9(10)	NR	NR	1.5
5/24/2005 #2	175X	10(7)	13(10)	NR*	NR*	1.75
5/24/2005 #1	230X	4(3)	13(10)	NR	NR	
5/23/2005 #2	175X	10(7)	13(10)	NR*	NR*	
5/20/2005 #1	150X	20(10)	12(10)	169	28	
5/19/2005 #2	215X	5(7)	8(7)	186	15	
5/19/2005 #1	160X	8(10)	12(10)	NR	NR	
5/18/2005 #1	120X	8(10)	12(10)	NR	NR	
5/17/2005 #2	160X	8(10)	8(7)	226	27	

Table A-7
Sputtering results (summer series)

VSM Measurements:

TbFe/FeCo 033005#2

033005#2 - 80 degrees

033005#2 - 90 degrees

TbFe/FeCo 032205#2

032205#2 - 0 degrees

032205#2 - 10 degrees

032205#2 - 20 degrees

032205#2 - 30 degrees

032205#2 - 40 degrees

032205#2 - 50 degrees

032205#2 - 60 degrees

M (emu)

H (Oe)

Series1

032205#2 -70 degrees

M (emu)

H (Oe)

Series1

032205#2 - 80 degrees

M (emu)

H (Oe)

Series1

032205#2 - 90 degrees

M (emu)

H (Oe)

Series1
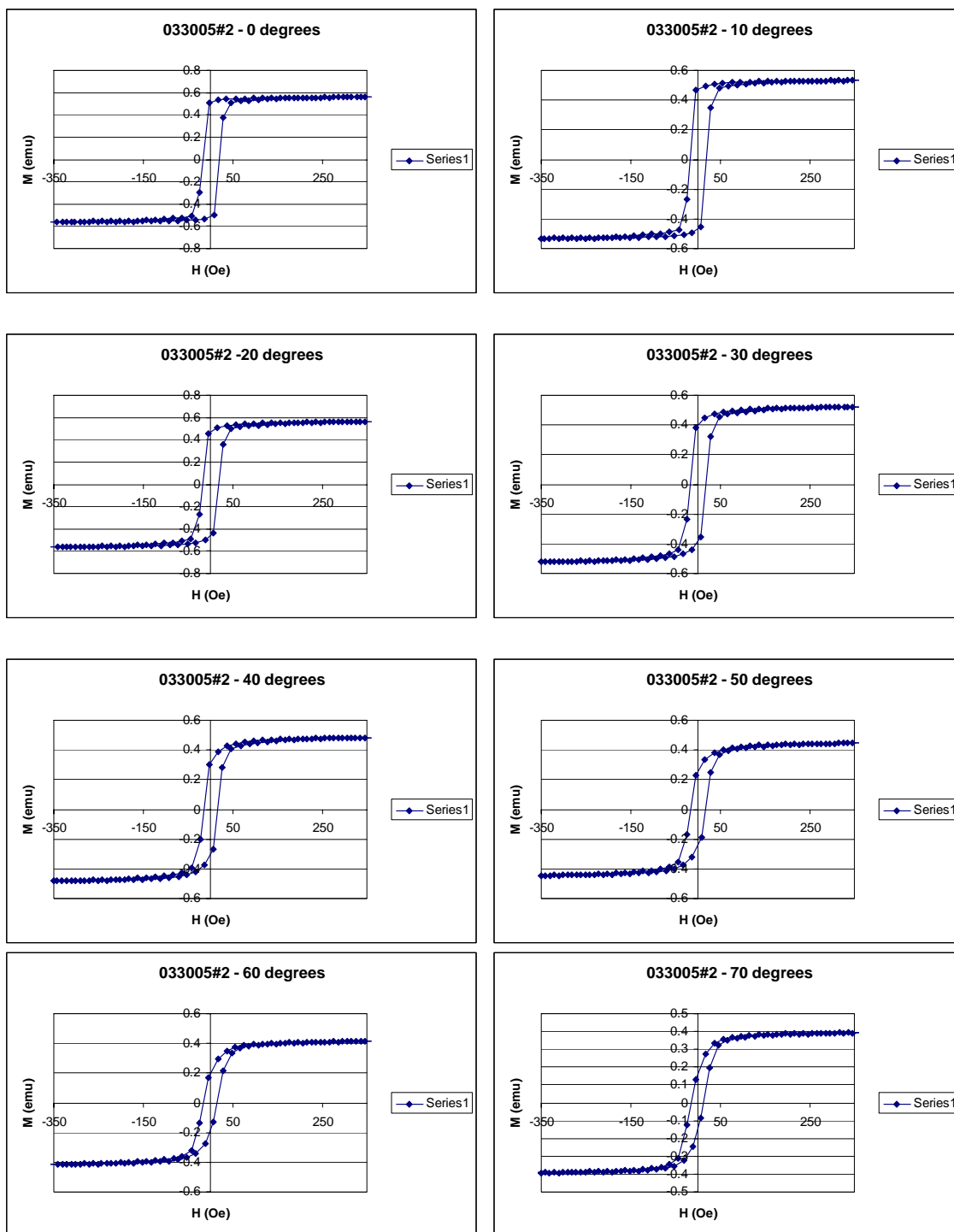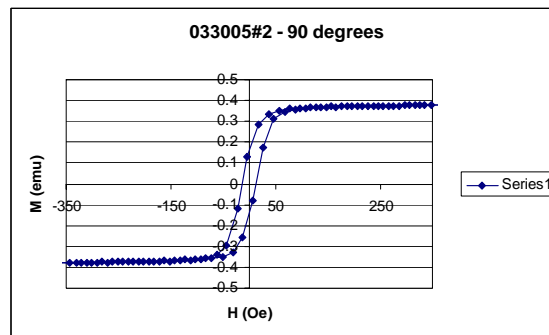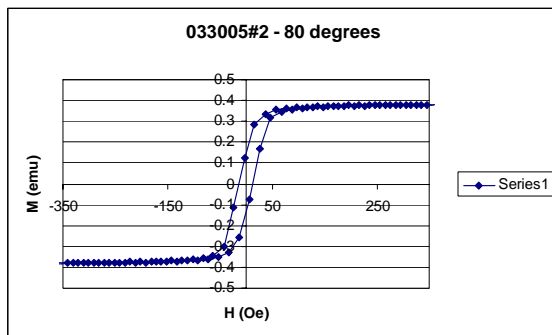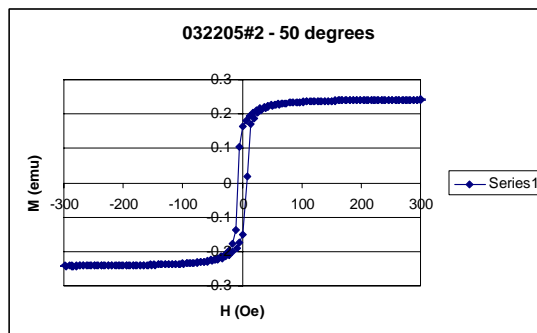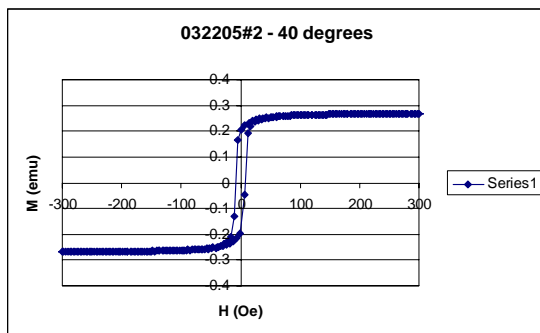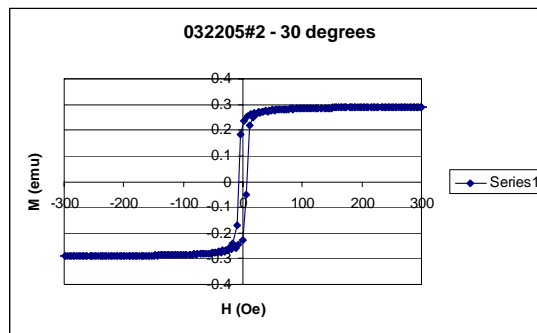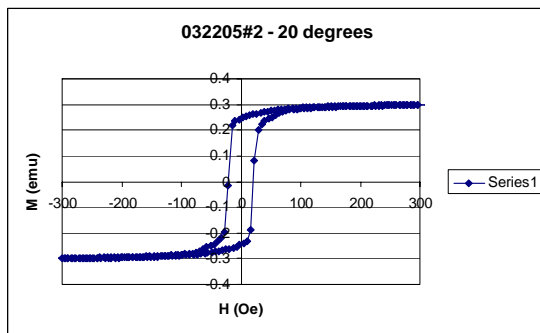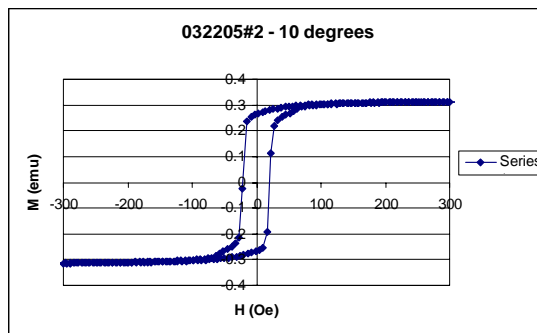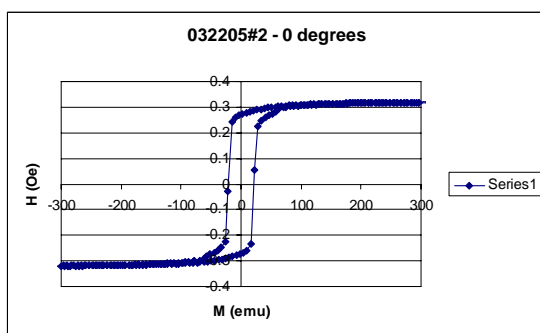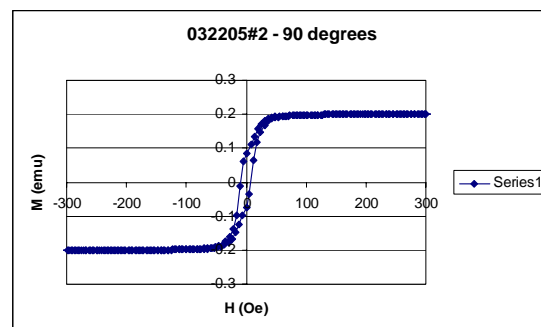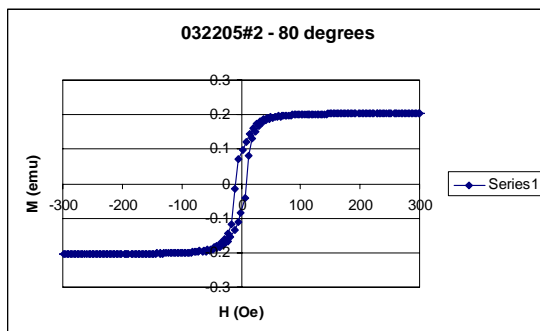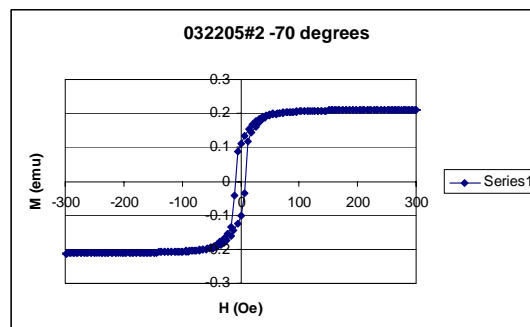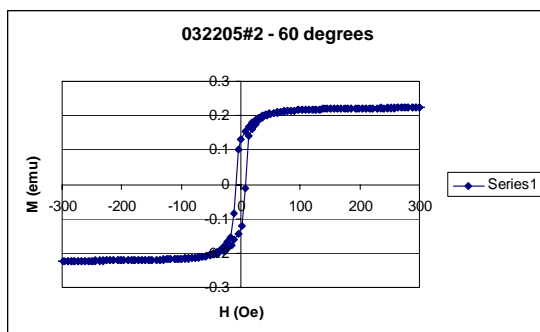
Kerr Tracer Measurements

Information Regarding Kerr Measurements of FeTb/FeCo Samples

The following samples are FeTb/FeCo multilayers deposited on silicon substrates. The samples were obtained from Southwest Research Institute.

The hysteresis curves were measured using a Kerr Tracer Setup. The curves were centered at zero on the y-axis by calculating an average Magneto-Optical signal for each curve and subtracting that average value from each individual data point for the measured signal.

Samples were measured at different orientations to identify a possible anisotropy. The orientation of the sample was taken to be 0 degrees when positioned lengthwise parallel to the applied positive field and rotated counterclockwise as in the diagram below.

TbFe/FeCo 032205#2

Sample 032205#2 - 80 degrees

Sample 032205#2 -90 degrees

Sample 032205#2 - 135 degrees

TbFe/FeCo: 033105#1

033105#1 - 0 degrees

033105#1 - 45 degrees

033105#1 - 90 degrees

033105#1 - 135 degrees

033105#1 - 180 degrees

TbFe/FeCo: 040305#1

040205#1 - 0 degrees

040205#1 - 45 degrees

040205#1 - 90 degrees

040205#1 - 135 degrees

040205#1 - 180 degrees
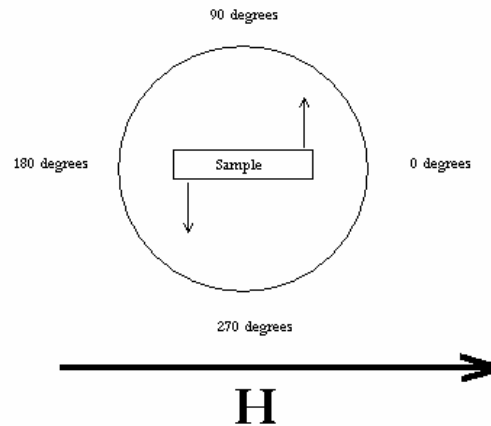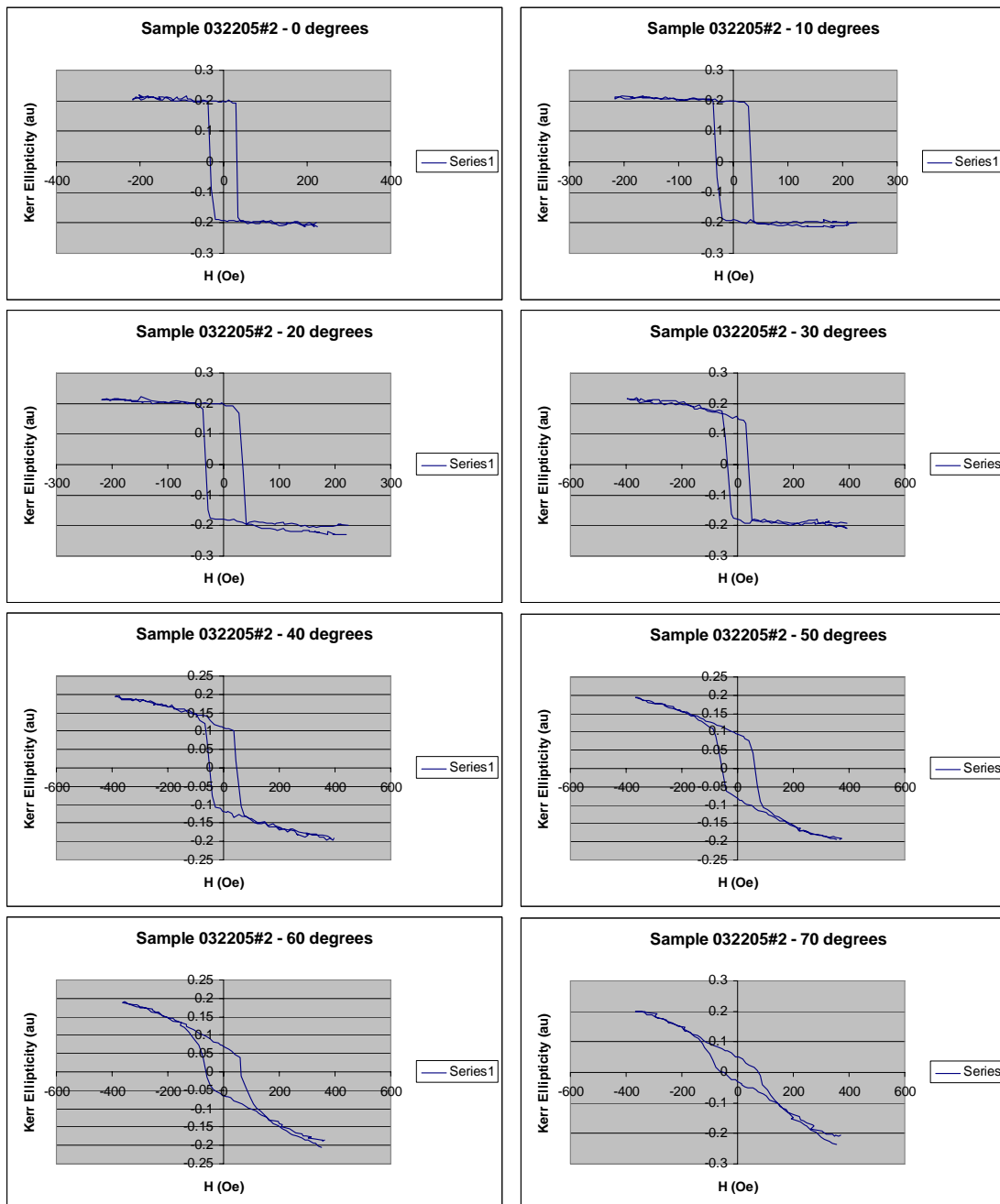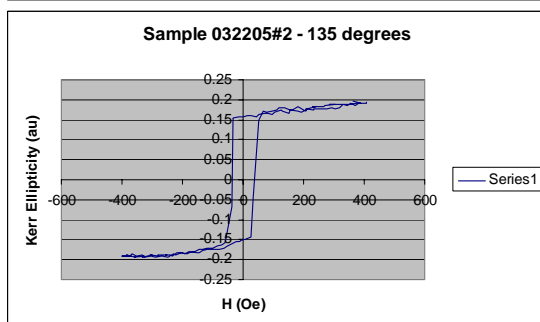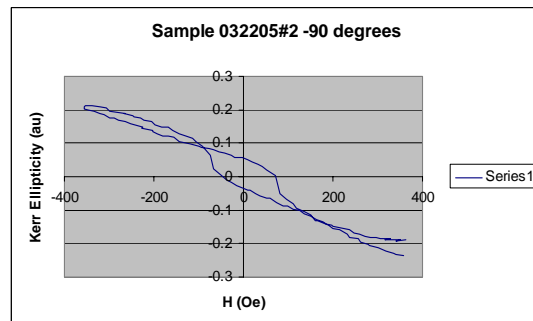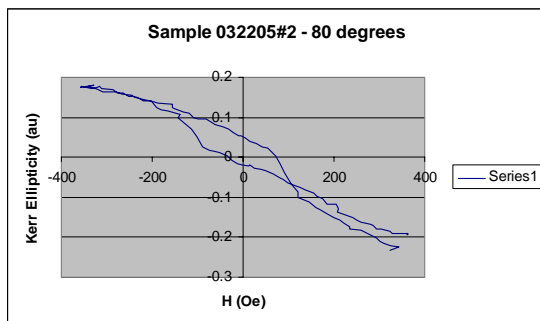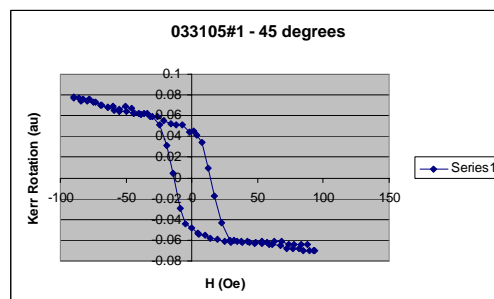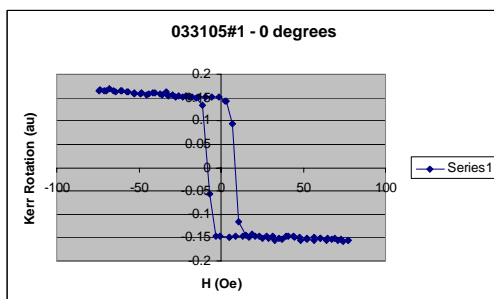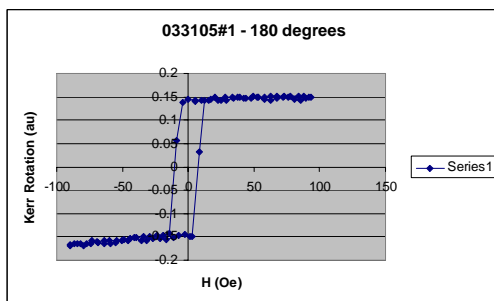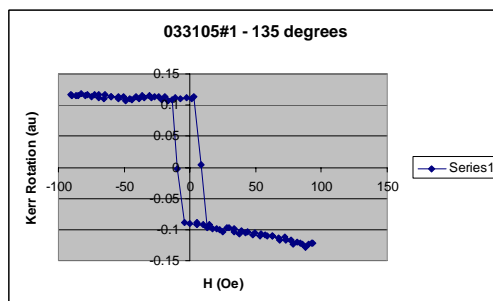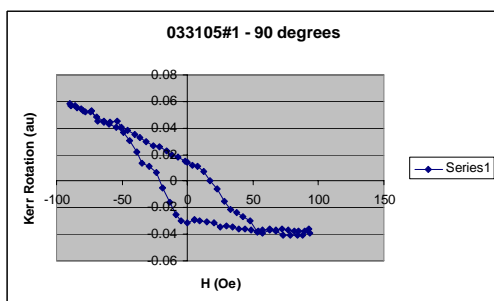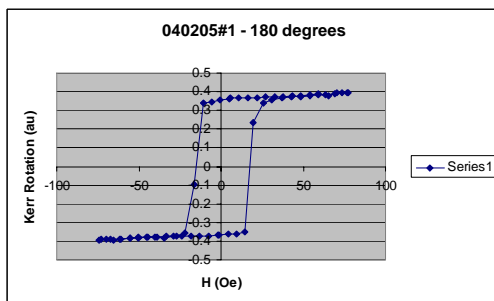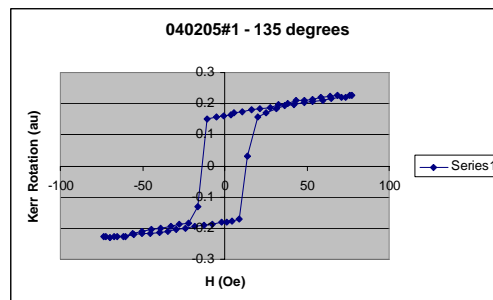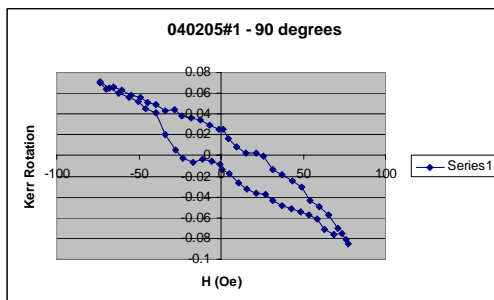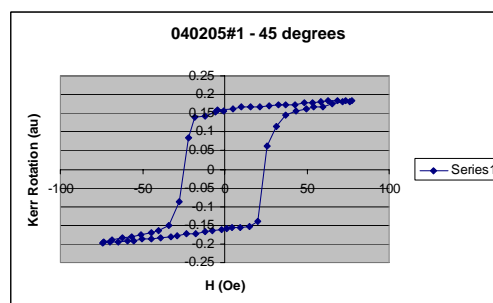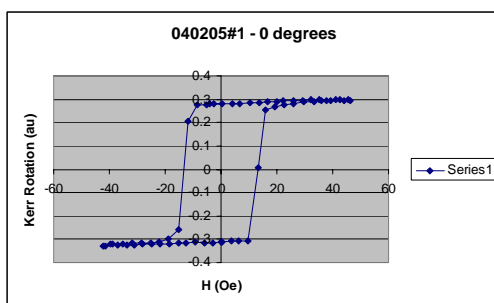
Magnetostriction Measurements

TbFe/FeCo Spring Samples:

032505

Deflection [um] vs H [Oe]

032805#1

Deflection [um] vs H [Oe]

032805#2

Deflection [um] vs H [Oe]

032905#1

Deflection [um] vs H [Oe]

TbFe022205#1

Deflection [um] vs H [Oe]

TbFe022305#2

Deflection [um] vs H [Oe]

033005#2

Deflection [um] vs H [Oe]

033105#1

Deflection [um] vs H [Oe]

040205#1

Deflection [um] vs H [Oe]
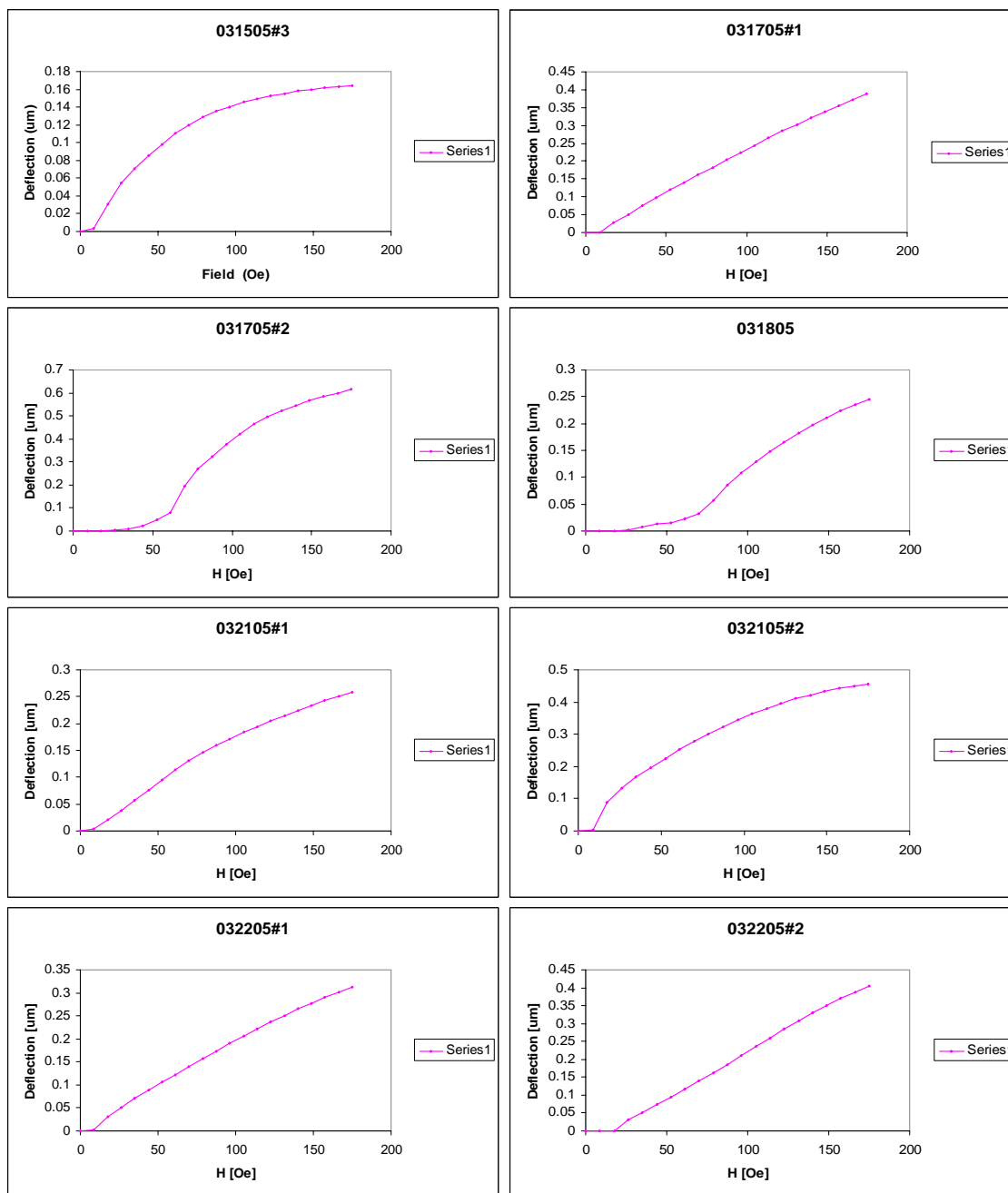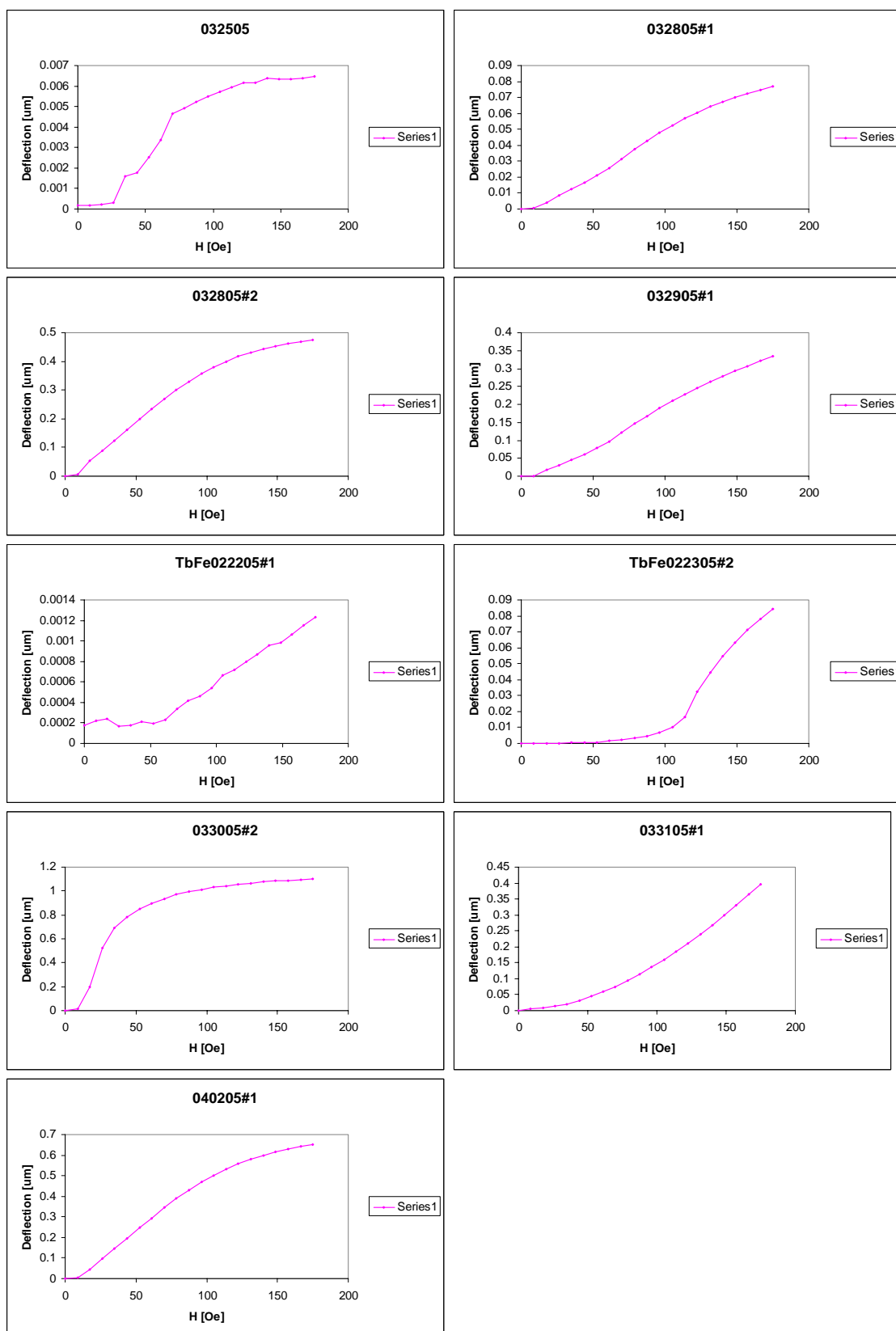
TbFe/FeCo Summer Samples:

NiFe35% Samples

101601#2

101701#4

101601#3

101901#1

101901#2

101901#3
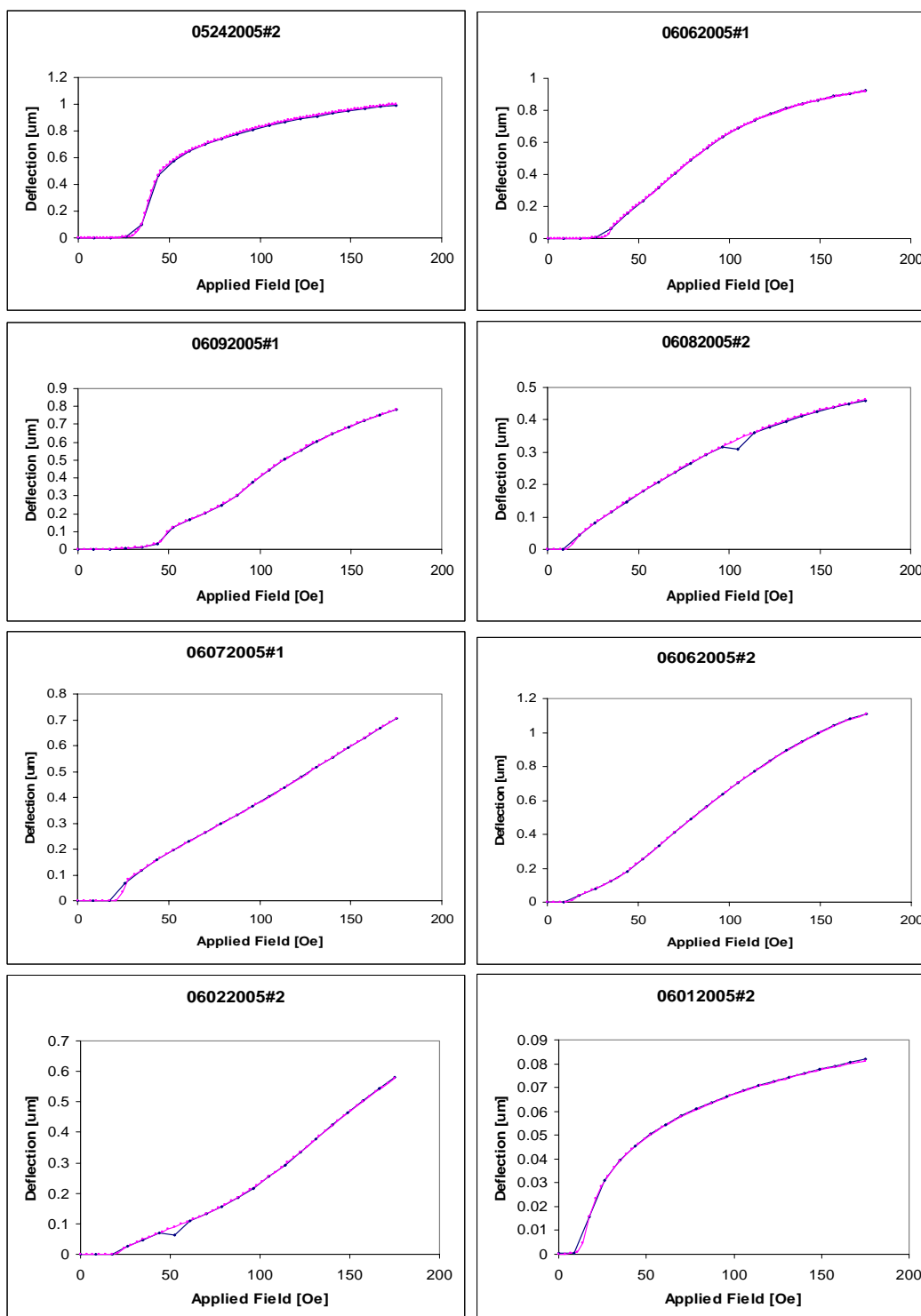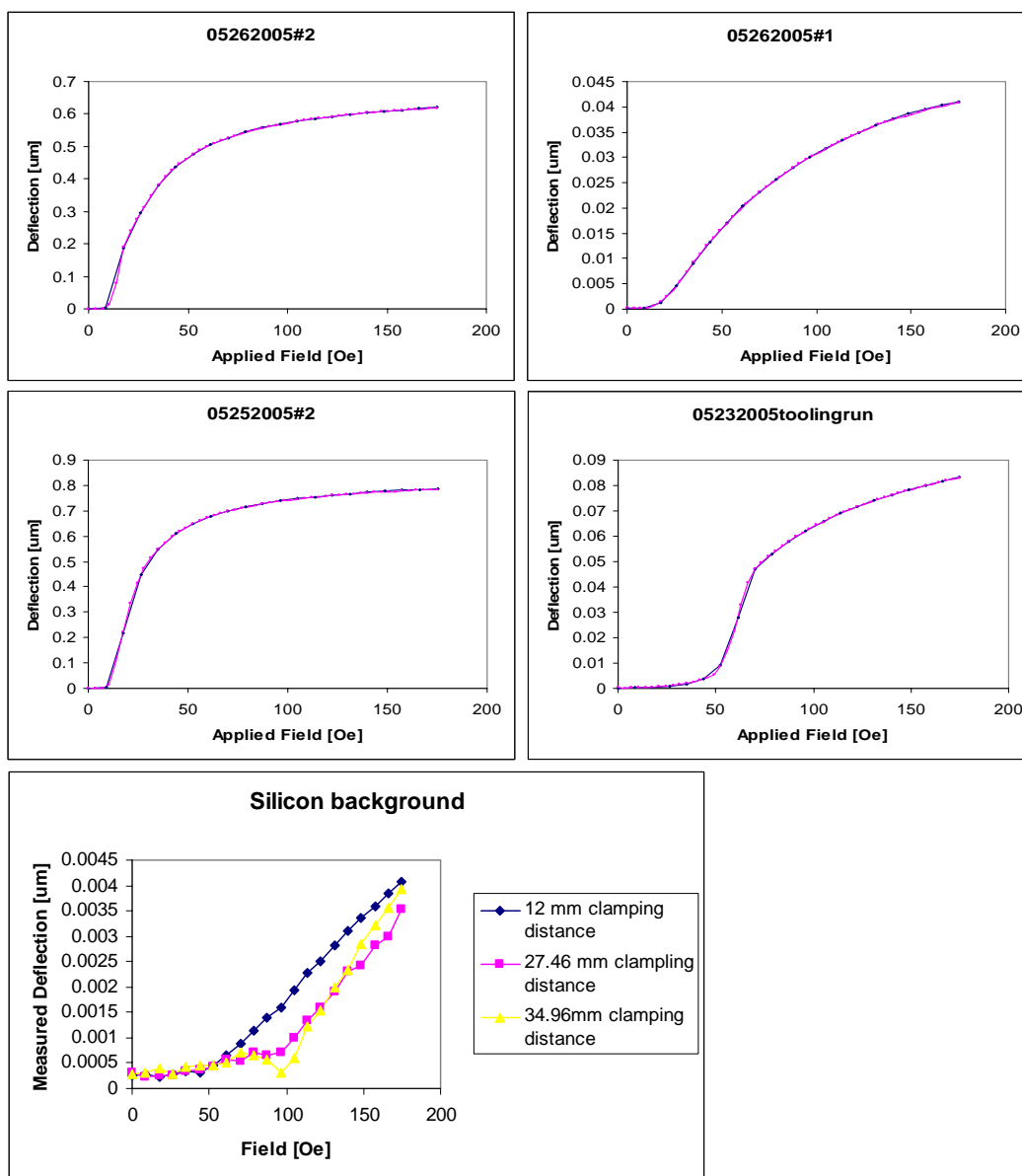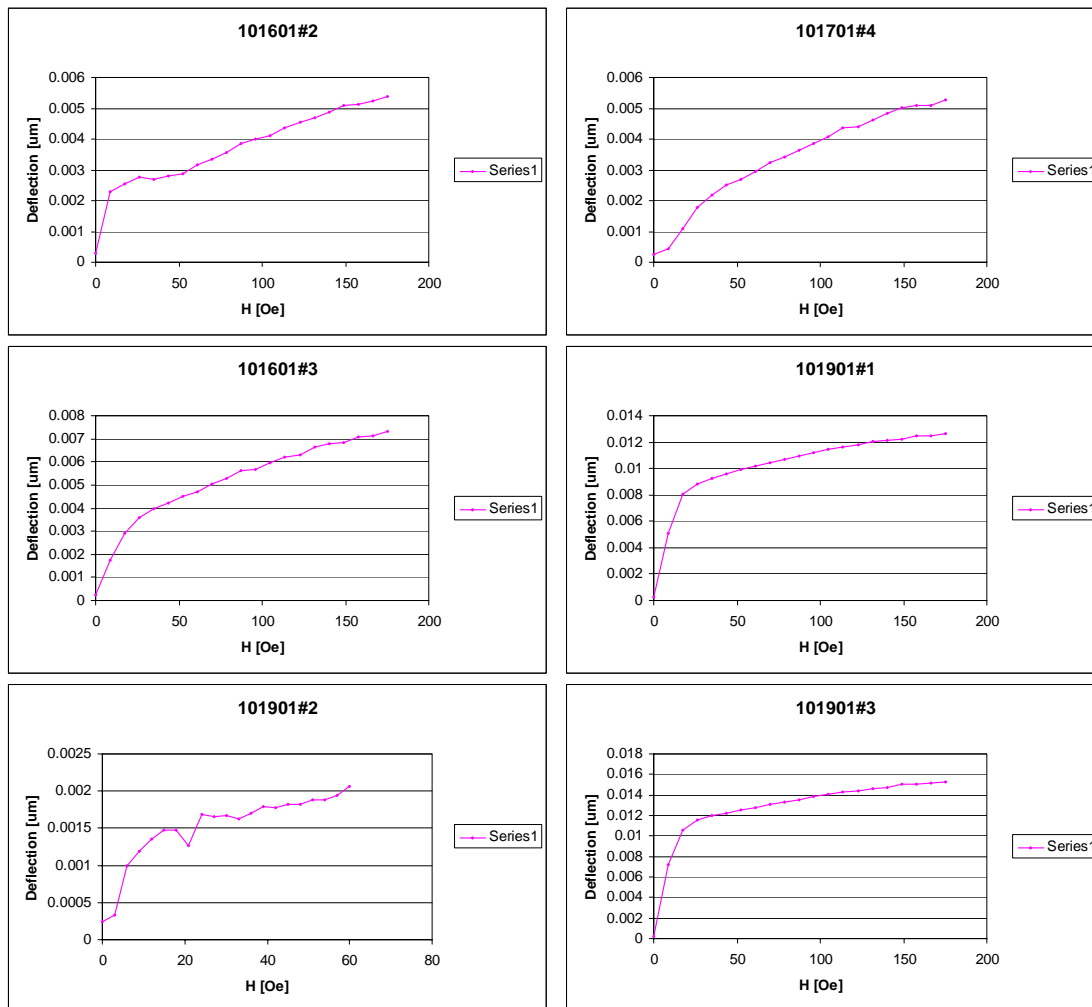
Capacitance Thickness Measurements:

NiFe45%

Frequency (kHz)	C1 (pF)	C2 (pF)	D1 (um)	D2 (um)	Ts1 (um)	R1 (kOhm)	R2 (kOhm)
			8.19E+2		8.19E+2		
10	0.36	1.21	0	143.679	0		
25	0.36	1.21	482.921	143.679	339.242		
50	0.36	1.21	482.921	143.679	339.242		
100	0.3605	1.207	482.2512	144.0361	338.2151		
250	0.361	1.206	481.5833	144.1555	337.4278		
500	0.361	1.206	481.5833	144.1555	337.4278		
1000	0.3602	1.2056	482.6529	144.2034	338.4495		
2500	0.36	1.2055	482.921	144.2153	338.7057		
5000	0.361	1.208	481.5833	143.9169	337.6664	-0.16	-0.03
7500	0.3632	1.2152	478.6662	143.0642	335.6021	-0.18	-0.03
10000	0.3658	1.2244	475.264	141.9892	333.2748	-0.2	-0.04
11500	0.3674	1.2297	473.1943	141.3772	331.817	-0.23	-0.05
13000	0.3679	1.2314	472.5512	141.182	331.3691	-0.29	-0.07

Avg Thickness:	6.3E+19
	3.06879
St. Dev:	1

Si

Frequency (kHz)	C1 (pF)	C2 (pF)	D1 (um)	D2 (um)	Ts1 (um)	R1 (kOhm)	R2 (kOhm)
10	0.44	1.39	395.1172	125.0731	270.0441		
25	0.44	1.39	395.1172	125.0731	270.0441		
50	0.44	1.39	395.1172	125.0731	270.0441		
100	0.437	1.393	397.8297	124.8037	273.026		
250	0.437	1.392	397.8297	124.8934	272.9363		
500	0.437	1.392	397.8297	124.8934	272.9363		
1000	0.4369	1.39	397.9207	125.0731	272.8477		

				125.073			
2500	0.437	1.39	397.8297	1	272.7566	-0.12	0.28
				125.073			
5000	0.438	1.39	396.9214	1	271.8483	-0.12	0.24
				124.714			
7500	0.4404	1.394	394.7583	2	270.0442	-0.14	0.21
				124.091			
10000	0.4436	1.401	391.9107	1	267.8196	-0.16	0.18
				123.781			
11500	0.4455	1.4045	390.2392	8	266.4574	-0.18	0.16
				123.799			
13000	0.4462	1.4043	389.627	5	265.8276	-0.23	0.13

Avg Thickness:	270.510 2
St. Dev:	2.86856 1

NiFe45%

<u>Polished Side Down</u>   Convex up

Frequency (Hz)	C1 (pF)	C2 (pF)	D1	D2	T	<u>Difference in Thickness</u>
500	15	1	11.5901	173.852	162.2615	10.14134
1000	13.6	0.5	12.7832	347.703	334.9199	9.649257
5000	13.4	0.5	12.974	347.703	334.7291	9.314665
10000	13.33	0.485	13.0421	358.457	345.4147	9.390332
100000	13.17	0.484	13.2006	359.197	345.9969	9.289926
500000	13.14	0.484	13.2307	359.197	345.9667	9.28892
1000000	13.111	0.484	13.26	359.197	345.9375	8.885283
2000000	13.09	0.484	13.2813	359.197	345.9162	9.238383
5000000	13.09	0.486	13.2813	357.719	344.438	8.471685

Average difference   9.296644
StDev: 0.461008

<u>Polished Side Up</u>   Concave up

Frequency (Hz)	C1 (pF)	C2 (pF)	D1	D2	T
500	8	1	21.7314	173.852	152.1201
1000	7.75	0.5	22.4325	347.703	325.2707
5000	7.8	0.5	22.2887	347.703	325.4145
10000	7.75	0.485	22.4325	358.457	336.0244
100000	7.73	0.484	22.4905	359.197	336.707
500000	7.72	0.484	22.5196	359.197	336.6778
1000000	7.721	0.4835	22.5167	359.569	337.0522
2000000	7.72	0.484	22.5196	359.197	336.6778
5000000	7.73	0.485	22.4905	358.457	335.9663

TbFe/FeCo Samples:

032805#2

Film UP			Film Down			C2		
FREQUENCY	C	R_G	FREQUENCY	C	R_G	FREQUENCY	C	R_G
1.00E+05	5.61E-12	1.00E-07	1.00E+05	4.67E-12	2.00E+04	1.00E+05	5.60E-13	4.80E+05
1.79E+05	5.53E-12	0.00E+00	1.79E+05	4.60E-12	2.00E+04	1.79E+05	5.30E-13	0.00E+00
2.58E+05	5.53E-12	0.00E+00	2.58E+05	4.45E-12	1.00E+04	2.58E+05	5.30E-13	-1.00E+04
3.37E+05	5.53E-12	0.00E+00	3.37E+05	4.34E-12	1.00E+04	3.37E+05	5.30E-13	0.00E+00
4.17E+05	5.50E-12	0.00E+00	4.17E+05	4.27E-12	1.00E+04	4.17E+05	5.30E-13	0.00E+00
4.96E+05	5.50E-12	0.00E+00	4.96E+05	4.20E-12	5.70E+03	4.96E+05	5.40E-13	0.00E+00
5.75E+05	5.50E-12	0.00E+00	5.75E+05	4.20E-12	4.50E+03	5.75E+05	5.30E-13	0.00E+00
6.54E+05	5.50E-12	0.00E+00	6.54E+05	4.20E-12	3.70E+03	6.54E+05	5.30E-13	0.00E+00
7.33E+05	5.53E-12	0.00E+00	7.33E+05	4.13E-12	3.00E+03	7.33E+05	5.32E-13	0.00E+00
8.13E+05	5.53E-12	0.00E+00	8.13E+05	4.12E-12	2.60E+03	8.13E+05	5.32E-13	0.00E+00
8.92E+05	5.53E-12	0.00E+00	8.92E+05	4.11E-12	2.20E+03	8.92E+05	5.33E-13	0.00E+00
9.71E+05	5.53E-12	0.00E+00	9.71E+05	4.09E-12	1.80E+03	9.71E+05	5.33E-13	0.00E+00
1.05E+06	5.53E-12	0.00E+00	1.05E+06	4.09E-12	1.60E+03	1.05E+06	5.33E-13	0.00E+00
1.13E+06	5.53E-12	0.00E+00	1.13E+06	4.08E-12	1.40E+03	1.13E+06	5.34E-13	0.00E+00
1.21E+06	5.53E-12	0.00E+00	1.21E+06	4.08E-12	1.30E+03	1.21E+06	5.34E-13	0.00E+00
1.29E+06	5.53E-12	0.00E+00	1.29E+06	4.07E-12	1.10E+03	1.29E+06	5.33E-13	0.00E+00
1.37E+06	5.53E-12	0.00E+00	1.37E+06	4.07E-12	1.00E+03	1.37E+06	5.34E-13	0.00E+00
1.45E+06	5.53E-12	0.00E+00	1.45E+06	4.07E-12	9.00E+02	1.45E+06	5.33E-13	0.00E+00
1.52E+06	5.53E-12	0.00E+00	1.52E+06	4.06E-12	8.00E+02	1.52E+06	5.33E-13	0.00E+00
1.60E+06	5.53E-12	0.00E+00	1.60E+06	4.06E-12	7.00E+02	1.60E+06	5.33E-13	0.00E+00
1.68E+06	5.53E-12	0.00E+00	1.68E+06	4.06E-12	7.00E+02	1.68E+06	5.32E-13	0.00E+00
1.76E+06	5.53E-12	0.00E+00	1.76E+06	4.06E-12	6.00E+02	1.76E+06	5.34E-13	0.00E+00
1.84E+06	5.53E-12	0.00E+00	1.84E+06	4.06E-12	6.00E+02	1.84E+06	5.34E-13	0.00E+00
1.92E+06	5.53E-12	0.00E+00	1.92E+06	4.05E-12	5.00E+02	1.92E+06	5.33E-13	0.00E+00
2.00E+06	5.53E-12	0.00E+00	2.00E+06	4.05E-12	5.00E+02	2.00E+06	5.33E-13	0.00E+00
2.08E+06	5.53E-12	0.00E+00	2.08E+06	4.05E-12	5.00E+02	2.08E+06	5.30E-13	0.00E+00

31805

Film Up			Film Down			C2		
FREQUENCY	C	R_G	FREQUENCY	C	R_G	FREQUENCY	C	R_G
1.00E+05	6.57E-12	3.00E+04	1.00E+05	6.75E-12	0.00E+00	1.00E+05	5.50E-13	-3.40E+05
1.79E+05	6.17E-12	2.00E+04	1.79E+05	9.30E-12	5.00E+04	1.79E+05	5.80E-13	0.00E+00
2.58E+05	5.90E-12	1.00E+04	2.58E+05	6.67E-12	0.00E+00	2.58E+05	5.80E-13	0.00E+00
3.37E+05	5.73E-12	1.00E+04	3.37E+05	6.70E-12	0.00E+00	3.37E+05	5.80E-13	0.00E+00
4.17E+05	5.60E-12	7.00E+03	4.17E+05	6.70E-12	0.00E+00	4.17E+05	5.80E-13	0.00E+00
4.96E+05	5.60E-12	5.40E+03	4.96E+05	6.70E-12	0.00E+00	4.96E+05	5.80E-13	0.00E+00
5.75E+05	5.50E-12	4.20E+03	5.75E+05	6.70E-12	0.00E+00	5.75E+05	5.80E-13	0.00E+00
6.54E+05	5.50E-12	3.40E+03	6.54E+05	6.70E-12	1.00E+02	6.54E+05	5.80E-13	0.00E+00
7.33E+05	5.43E-12	2.80E+03	7.33E+05	6.67E-12	0.00E+00	7.33E+05	5.80E-13	0.00E+00
8.13E+05	5.41E-12	2.30E+03	8.13E+05	6.67E-12	0.00E+00	8.13E+05	5.80E-13	0.00E+00
8.92E+05	5.39E-12	2.00E+03	8.92E+05	6.67E-12	0.00E+00	8.92E+05	5.81E-13	0.00E+00
9.71E+05	5.38E-12	1.70E+03	9.71E+05	6.68E-12	0.00E+00	9.71E+05	5.80E-13	0.00E+00
1.05E+06	5.37E-12	1.40E+03	1.05E+06	6.68E-12	0.00E+00	1.05E+06	5.80E-13	0.00E+00
1.13E+06	5.36E-12	1.30E+03	1.13E+06	6.68E-12	0.00E+00	1.13E+06	5.80E-13	0.00E+00
1.21E+06	5.35E-12	1.10E+03	1.21E+06	6.68E-12	0.00E+00	1.21E+06	5.80E-13	0.00E+00
1.29E+06	5.35E-12	1.00E+03	1.29E+06	6.68E-12	0.00E+00	1.29E+06	5.80E-13	0.00E+00
1.37E+06	5.35E-12	9.00E+02	1.37E+06	6.68E-12	0.00E+00	1.37E+06	5.80E-13	0.00E+00
1.45E+06	5.34E-12	8.00E+02	1.45E+06	6.68E-12	0.00E+00	1.45E+06	5.81E-13	0.00E+00
1.52E+06	5.34E-12	7.00E+02	1.52E+06	6.68E-12	0.00E+00	1.52E+06	5.81E-13	0.00E+00
1.60E+06	5.33E-12	7.00E+02	1.60E+06	6.68E-12	0.00E+00	1.60E+06	5.81E-13	0.00E+00
1.68E+06	5.33E-12	6.00E+02	1.68E+06	6.68E-12	0.00E+00	1.68E+06	5.79E-13	0.00E+00
1.76E+06	5.33E-12	6.00E+02	1.76E+06	6.68E-12	0.00E+00	1.76E+06	5.79E-13	0.00E+00
1.84E+06	5.33E-12	5.00E+02	1.84E+06	6.68E-12	0.00E+00	1.84E+06	5.82E-13	0.00E+00
1.92E+06	5.33E-12	5.00E+02	1.92E+06	6.68E-12	0.00E+00	1.92E+06	5.81E-13	0.00E+00
2.00E+06	5.32E-12	4.00E+02	2.00E+06	6.68E-12	0.00E+00	2.00E+06	5.81E-13	0.00E+00
2.08E+06	5.32E-12	4.00E+02	2.08E+06	6.68E-12	0.00E+00	2.08E+06	5.80E-13	1.00E+02

032105#2

Film Up			Film Down			C2		
FREQUENCY	C	R_G	FREQUENCY	C	R_G	FREQUENCY	C	R_G
1.00E+05	7.16E-12	1.00E+04	1.00E+05	6.40E-12	1.00E+04	1.00E+05	6.00E-13	4.20E+05
1.79E+05	7.20E-12	0.00E+00	1.79E+05	6.47E-12	0.00E+00	1.79E+05	5.70E-13	0.00E+00
2.58E+05	7.20E-12	0.00E+00	2.58E+05	6.49E-12	0.00E+00	2.58E+05	5.70E-13	0.00E+00
3.37E+05	7.20E-12	3.00E+02	3.37E+05	6.50E-12	1.00E+03	3.37E+05	5.70E-13	0.00E+00
4.17E+05	7.20E-12	1.00E+02	4.17E+05	6.50E-12	5.00E+02	4.17E+05	5.70E-13	0.00E+00
4.96E+05	7.20E-12	0.00E+00	4.96E+05	6.50E-12	4.00E+02	4.96E+05	5.70E-13	0.00E+00
5.75E+05	7.30E-12	0.00E+00	5.75E+05	6.50E-12	3.00E+02	5.75E+05	5.70E-13	0.00E+00
6.54E+05	7.30E-12	0.00E+00	6.54E+05	6.50E-12	4.00E+02	6.54E+05	5.70E-13	0.00E+00
7.33E+05	7.26E-12	0.00E+00	7.33E+05	6.49E-12	3.00E+02	7.33E+05	5.70E-13	0.00E+00
8.13E+05	7.26E-12	0.00E+00	8.13E+05	6.49E-12	2.00E+02	8.13E+05	5.71E-13	0.00E+00
8.92E+05	7.27E-12	0.00E+00	8.92E+05	6.49E-12	2.00E+02	8.92E+05	5.69E-13	0.00E+00
9.71E+05	7.26E-12	0.00E+00	9.71E+05	6.49E-12	1.00E+02	9.71E+05	5.71E-13	0.00E+00
1.05E+06	7.27E-12	0.00E+00	1.05E+06	6.50E-12	1.00E+02	1.05E+06	5.70E-13	0.00E+00
1.13E+06	7.27E-12	0.00E+00	1.13E+06	6.50E-12	1.00E+02	1.13E+06	5.68E-13	0.00E+00
1.21E+06	7.27E-12	0.00E+00	1.21E+06	6.50E-12	1.00E+02	1.21E+06	5.70E-13	0.00E+00
1.29E+06	7.27E-12	0.00E+00	1.29E+06	6.50E-12	1.00E+02	1.29E+06	5.69E-13	0.00E+00
1.37E+06	7.27E-12	0.00E+00	1.37E+06	6.50E-12	1.00E+02	1.37E+06	5.70E-13	0.00E+00
1.45E+06	7.27E-12	0.00E+00	1.45E+06	6.50E-12	1.00E+02	1.45E+06	5.71E-13	0.00E+00
1.52E+06	7.27E-12	0.00E+00	1.52E+06	6.50E-12	1.00E+02	1.52E+06	5.70E-13	0.00E+00
1.60E+06	7.27E-12	0.00E+00	1.60E+06	6.50E-12	0.00E+00	1.60E+06	5.71E-13	0.00E+00
1.68E+06	7.27E-12	0.00E+00	1.68E+06	6.50E-12	0.00E+00	1.68E+06	5.69E-13	0.00E+00
1.76E+06	7.27E-12	0.00E+00	1.76E+06	6.50E-12	0.00E+00	1.76E+06	5.71E-13	0.00E+00
1.84E+06	7.27E-12	0.00E+00	1.84E+06	6.50E-12	0.00E+00	1.84E+06	5.70E-13	0.00E+00
1.92E+06	7.26E-12	0.00E+00	1.92E+06	6.50E-12	0.00E+00	1.92E+06	5.70E-13	0.00E+00
2.00E+06	7.27E-12	0.00E+00	2.00E+06	6.50E-12	0.00E+00	2.00E+06	5.70E-13	0.00E+00
2.08E+06	7.26E-12	0.00E+00	2.08E+06	6.50E-12	0.00E+00	2.08E+06	5.70E-13	-1.00E+02

32505

Film Up			Film Down			C2		
FREQUENCY	C	R_G	FREQUENCY	C	R_G	FREQUENCY	C	R_G
1.00E+05	2.54E-12	2.00E+04	1.00E+05	2.32E-12	-1.00E+04	1.00E+05	5.80E-13	6.00E+04
1.79E+05	2.59E-12	0.00E+00	1.79E+05	2.38E-12	0.00E+00	1.79E+05	5.00E-13	0.00E+00
2.58E+05	2.58E-12	0.00E+00	2.58E+05	2.38E-12	0.00E+00	2.58E+05	5.00E-13	-1.00E+04
3.37E+05	2.59E-12	0.00E+00	3.37E+05	2.38E-12	0.00E+00	3.37E+05	5.00E-13	0.00E+00
4.17E+05	2.58E-12	0.00E+00	4.17E+05	2.38E-12	0.00E+00	4.17E+05	5.00E-13	0.00E+00
4.96E+05	2.58E-12	0.00E+00	4.96E+05	2.38E-12	0.00E+00	4.96E+05	5.00E-13	0.00E+00
5.75E+05	2.58E-12	0.00E+00	5.75E+05	2.38E-12	0.00E+00	5.75E+05	5.00E-13	0.00E+00
6.54E+05	2.58E-12	0.00E+00	6.54E+05	2.38E-12	0.00E+00	6.54E+05	5.00E-13	0.00E+00
7.33E+05	2.58E-12	0.00E+00	7.33E+05	2.38E-12	0.00E+00	7.33E+05	5.01E-13	0.00E+00
8.13E+05	2.58E-12	0.00E+00	8.13E+05	2.38E-12	0.00E+00	8.13E+05	5.02E-13	0.00E+00
8.92E+05	2.58E-12	0.00E+00	8.92E+05	2.38E-12	0.00E+00	8.92E+05	5.00E-13	0.00E+00
9.71E+05	2.58E-12	0.00E+00	9.71E+05	2.38E-12	0.00E+00	9.71E+05	5.01E-13	0.00E+00
1.05E+06	2.58E-12	1.00E+02	1.05E+06	2.38E-12	1.00E+02	1.05E+06	5.01E-13	0.00E+00
1.13E+06	2.58E-12	0.00E+00	1.13E+06	2.38E-12	0.00E+00	1.13E+06	5.01E-13	0.00E+00
1.21E+06	2.58E-12	0.00E+00	1.21E+06	2.38E-12	0.00E+00	1.21E+06	5.02E-13	0.00E+00
1.29E+06	2.58E-12	0.00E+00	1.29E+06	2.38E-12	0.00E+00	1.29E+06	5.03E-13	0.00E+00
1.37E+06	2.58E-12	0.00E+00	1.37E+06	2.38E-12	0.00E+00	1.37E+06	5.00E-13	0.00E+00
1.45E+06	2.58E-12	0.00E+00	1.45E+06	2.38E-12	0.00E+00	1.45E+06	5.01E-13	0.00E+00
1.52E+06	2.58E-12	0.00E+00	1.52E+06	2.38E-12	0.00E+00	1.52E+06	5.01E-13	0.00E+00
1.60E+06	2.58E-12	0.00E+00	1.60E+06	2.38E-12	0.00E+00	1.60E+06	5.01E-13	0.00E+00
1.68E+06	2.58E-12	0.00E+00	1.68E+06	2.38E-12	0.00E+00	1.68E+06	5.02E-13	0.00E+00
1.76E+06	2.58E-12	0.00E+00	1.76E+06	2.38E-12	0.00E+00	1.76E+06	5.01E-13	0.00E+00
1.84E+06	2.58E-12	0.00E+00	1.84E+06	2.38E-12	0.00E+00	1.84E+06	5.01E-13	0.00E+00
1.92E+06	2.58E-12	0.00E+00	1.92E+06	2.38E-12	0.00E+00	1.92E+06	5.01E-13	0.00E+00
2.00E+06	2.58E-12	0.00E+00	2.00E+06	2.38E-12	0.00E+00	2.00E+06	5.01E-13	0.00E+00
2.08E+06	2.58E-12	0.00E+00	2.08E+06	2.38E-12	0.00E+00	2.08E+06	5.00E-13	-1.00E+02

032205#1

Film Up			Film Down			C2		
FREQUENCY	C	R_G	FREQUENCY	C	R_G	FREQUENCY	C	R_G
1.00E+05	7.59E-12	0.00E+00	1.00E+05	5.31E-12	0.00E+00	1.00E+05	4.80E-13	-9.00E+04
1.79E+05	7.59E-12	0.00E+00	1.79E+05	5.23E-12	0.00E+00	1.79E+05	5.60E-13	1.00E+04
2.58E+05	7.60E-12	0.00E+00	2.58E+05	5.23E-12	0.00E+00	2.58E+05	5.60E-13	0.00E+00
3.37E+05	7.60E-12	4.00E+02	3.37E+05	5.23E-12	0.00E+00	3.37E+05	5.50E-13	0.00E+00
4.17E+05	7.60E-12	3.00E+02	4.17E+05	5.20E-12	0.00E+00	4.17E+05	5.50E-13	0.00E+00
4.96E+05	7.60E-12	1.00E+02	4.96E+05	5.20E-12	0.00E+00	4.96E+05	5.60E-13	0.00E+00
5.75E+05	7.60E-12	1.00E+02	5.75E+05	5.20E-12	0.00E+00	5.75E+05	5.50E-13	0.00E+00
6.54E+05	7.60E-12	1.00E+02	6.54E+05	5.20E-12	0.00E+00	6.54E+05	5.60E-13	0.00E+00
7.33E+05	7.59E-12	1.00E+02	7.33E+05	5.23E-12	0.00E+00	7.33E+05	5.53E-13	0.00E+00
8.13E+05	7.60E-12	1.00E+02	8.13E+05	5.23E-12	0.00E+00	8.13E+05	5.54E-13	0.00E+00
8.92E+05	7.60E-12	1.00E+02	8.92E+05	5.23E-12	0.00E+00	8.92E+05	5.54E-13	0.00E+00
9.71E+05	7.60E-12	0.00E+00	9.71E+05	5.23E-12	0.00E+00	9.71E+05	5.55E-13	0.00E+00
1.05E+06	7.60E-12	0.00E+00	1.05E+06	5.23E-12	0.00E+00	1.05E+06	5.55E-13	0.00E+00
1.13E+06	7.60E-12	0.00E+00	1.13E+06	5.23E-12	0.00E+00	1.13E+06	5.54E-13	0.00E+00
1.21E+06	7.60E-12	0.00E+00	1.21E+06	5.23E-12	0.00E+00	1.21E+06	5.56E-13	0.00E+00
1.29E+06	7.60E-12	0.00E+00	1.29E+06	5.23E-12	0.00E+00	1.29E+06	5.55E-13	0.00E+00
1.37E+06	7.60E-12	0.00E+00	1.37E+06	5.23E-12	0.00E+00	1.37E+06	5.53E-13	0.00E+00
1.45E+06	7.60E-12	0.00E+00	1.45E+06	5.23E-12	0.00E+00	1.45E+06	5.53E-13	0.00E+00
1.52E+06	7.60E-12	0.00E+00	1.52E+06	5.23E-12	0.00E+00	1.52E+06	5.53E-13	0.00E+00
1.60E+06	7.60E-12	0.00E+00	1.60E+06	5.23E-12	0.00E+00	1.60E+06	5.54E-13	0.00E+00
1.68E+06	7.60E-12	0.00E+00	1.68E+06	5.23E-12	0.00E+00	1.68E+06	5.55E-13	0.00E+00
1.76E+06	7.60E-12	0.00E+00	1.76E+06	5.23E-12	0.00E+00	1.76E+06	5.54E-13	0.00E+00
1.84E+06	7.60E-12	0.00E+00	1.84E+06	5.23E-12	0.00E+00	1.84E+06	5.54E-13	0.00E+00
1.92E+06	7.60E-12	0.00E+00	1.92E+06	5.23E-12	0.00E+00	1.92E+06	5.55E-13	0.00E+00
2.00E+06	7.60E-12	0.00E+00	2.00E+06	5.23E-12	0.00E+00	2.00E+06	5.54E-13	0.00E+00
2.08E+06	7.60E-12	0.00E+00	2.08E+06	5.23E-12	0.00E+00	2.08E+06	5.60E-13	0.00E+00

031705#2

Film Up			Film Down			C2		
FREQUENCY	C	R_G	FREQUENCY	C	R_G	FREQUENCY	C	R_G
1.00E+05	5.39E-12	0.00E+00	1.00E+05	4.05E-12	1.00E+04	1.00E+05	5.40E-13	-3.70E+05
1.79E+05	5.37E-12	0.00E+00	1.79E+05	3.99E-12	0.00E+00	1.79E+05	5.60E-13	0.00E+00
2.58E+05	5.37E-12	0.00E+00	2.58E+05	3.98E-12	0.00E+00	2.58E+05	5.50E-13	0.00E+00
3.37E+05	5.37E-12	0.00E+00	3.37E+05	3.99E-12	0.00E+00	3.37E+05	5.50E-13	0.00E+00
4.17E+05	5.40E-12	0.00E+00	4.17E+05	3.98E-12	0.00E+00	4.17E+05	5.50E-13	0.00E+00
4.96E+05	5.40E-12	0.00E+00	4.96E+05	3.98E-12	0.00E+00	4.96E+05	5.50E-13	0.00E+00
5.75E+05	5.40E-12	0.00E+00	5.75E+05	4.00E-12	0.00E+00	5.75E+05	5.60E-13	0.00E+00
6.54E+05	5.40E-12	0.00E+00	6.54E+05	4.00E-12	0.00E+00	6.54E+05	5.50E-13	0.00E+00
7.33E+05	5.37E-12	0.00E+00	7.33E+05	3.98E-12	0.00E+00	7.33E+05	5.52E-13	0.00E+00
8.13E+05	5.37E-12	0.00E+00	8.13E+05	3.98E-12	0.00E+00	8.13E+05	5.55E-13	0.00E+00
8.92E+05	5.36E-12	0.00E+00	8.92E+05	3.98E-12	0.00E+00	8.92E+05	5.53E-13	0.00E+00
9.71E+05	5.37E-12	0.00E+00	9.71E+05	3.98E-12	0.00E+00	9.71E+05	5.54E-13	0.00E+00
1.05E+06	5.37E-12	0.00E+00	1.05E+06	3.98E-12	0.00E+00	1.05E+06	5.55E-13	0.00E+00
1.13E+06	5.37E-12	0.00E+00	1.13E+06	3.98E-12	0.00E+00	1.13E+06	5.53E-13	0.00E+00
1.21E+06	5.37E-12	0.00E+00	1.21E+06	3.98E-12	0.00E+00	1.21E+06	5.54E-13	0.00E+00
1.29E+06	5.37E-12	0.00E+00	1.29E+06	3.98E-12	0.00E+00	1.29E+06	5.54E-13	0.00E+00
1.37E+06	5.37E-12	0.00E+00	1.37E+06	3.98E-12	0.00E+00	1.37E+06	5.54E-13	0.00E+00
1.45E+06	5.36E-12	0.00E+00	1.45E+06	3.98E-12	0.00E+00	1.45E+06	5.53E-13	0.00E+00
1.52E+06	5.36E-12	0.00E+00	1.52E+06	3.98E-12	0.00E+00	1.52E+06	5.54E-13	0.00E+00
1.60E+06	5.36E-12	0.00E+00	1.60E+06	3.98E-12	0.00E+00	1.60E+06	5.54E-13	0.00E+00
1.68E+06	5.36E-12	0.00E+00	1.68E+06	3.98E-12	0.00E+00	1.68E+06	5.54E-13	0.00E+00
1.76E+06	5.36E-12	0.00E+00	1.76E+06	3.98E-12	0.00E+00	1.76E+06	5.53E-13	0.00E+00
1.84E+06	5.36E-12	0.00E+00	1.84E+06	3.98E-12	0.00E+00	1.84E+06	5.54E-13	0.00E+00
1.92E+06	5.36E-12	0.00E+00	1.92E+06	3.98E-12	0.00E+00	1.92E+06	5.54E-13	0.00E+00
2.00E+06	5.36E-12	0.00E+00	2.00E+06	3.98E-12	0.00E+00	2.00E+06	5.54E-13	0.00E+00
2.08E+06	5.36E-12	0.00E+00	2.08E+06	3.98E-12	0.00E+00	2.08E+06	5.60E-13	0.00E+00

031705#1

Film Up			Film Down			C2		
FREQUENCY	C	R_G	FREQUENCY	C	R_G	FREQUENCY	C	R_G
1.00E+05	6.75E-12	4.00E+04	1.00E+05	5.39E-12	1.00E+04	1.00E+05	5.70E-13	3.90E+05
1.79E+05	6.58E-12	2.00E+04	1.79E+05	5.23E-12	0.00E+00	1.79E+05	5.80E-13	1.00E+04
2.58E+05	6.53E-12	1.00E+04	2.58E+05	5.23E-12	0.00E+00	2.58E+05	5.80E-13	0.00E+00
3.37E+05	6.50E-12	4.50E+03	3.37E+05	5.22E-12	0.00E+00	3.37E+05	5.80E-13	0.00E+00
4.17E+05	6.50E-12	3.00E+03	4.17E+05	5.20E-12	3.00E+02	4.17E+05	5.80E-13	0.00E+00
4.96E+05	6.50E-12	2.20E+03	4.96E+05	5.20E-12	2.00E+02	4.96E+05	5.80E-13	0.00E+00
5.75E+05	6.50E-12	1.70E+03	5.75E+05	5.20E-12	2.00E+02	5.75E+05	5.80E-13	0.00E+00
6.54E+05	6.50E-12	1.40E+03	6.54E+05	5.20E-12	2.00E+02	6.54E+05	5.80E-13	0.00E+00
7.33E+05	6.49E-12	1.00E+03	7.33E+05	5.22E-12	2.00E+02	7.33E+05	5.77E-13	0.00E+00
8.13E+05	6.49E-12	9.00E+02	8.13E+05	5.22E-12	1.00E+02	8.13E+05	5.78E-13	0.00E+00
8.92E+05	6.49E-12	7.00E+02	8.92E+05	5.22E-12	1.00E+02	8.92E+05	5.77E-13	0.00E+00
9.71E+05	6.49E-12	6.00E+02	9.71E+05	5.22E-12	1.00E+02	9.71E+05	5.79E-13	0.00E+00
1.05E+06	6.48E-12	5.00E+02	1.05E+06	5.23E-12	1.00E+02	1.05E+06	5.78E-13	0.00E+00
1.13E+06	6.49E-12	4.00E+02	1.13E+06	5.22E-12	1.00E+02	1.13E+06	5.77E-13	0.00E+00
1.21E+06	6.49E-12	4.00E+02	1.21E+06	5.22E-12	1.00E+02	1.21E+06	5.77E-13	0.00E+00
1.29E+06	6.49E-12	4.00E+02	1.29E+06	5.22E-12	1.00E+02	1.29E+06	5.79E-13	0.00E+00
1.37E+06	6.49E-12	3.00E+02	1.37E+06	5.23E-12	0.00E+00	1.37E+06	5.78E-13	0.00E+00
1.45E+06	6.49E-12	3.00E+02	1.45E+06	5.22E-12	0.00E+00	1.45E+06	5.78E-13	0.00E+00
1.52E+06	6.49E-12	3.00E+02	1.52E+06	5.22E-12	0.00E+00	1.52E+06	5.77E-13	0.00E+00
1.60E+06	6.48E-12	2.00E+02	1.60E+06	5.22E-12	0.00E+00	1.60E+06	5.78E-13	0.00E+00
1.68E+06	6.48E-12	2.00E+02	1.68E+06	5.22E-12	0.00E+00	1.68E+06	5.78E-13	0.00E+00
1.76E+06	6.48E-12	2.00E+02	1.76E+06	5.22E-12	0.00E+00	1.76E+06	5.76E-13	0.00E+00
1.84E+06	6.48E-12	2.00E+02	1.84E+06	5.22E-12	0.00E+00	1.84E+06	5.77E-13	0.00E+00
1.92E+06	6.48E-12	2.00E+02	1.92E+06	5.22E-12	0.00E+00	1.92E+06	5.76E-13	0.00E+00
2.00E+06	6.48E-12	1.00E+02	2.00E+06	5.22E-12	0.00E+00	2.00E+06	5.77E-13	0.00E+00
2.08E+06	6.48E-12	1.00E+02	2.08E+06	5.22E-12	0.00E+00	2.08E+06	5.80E-13	0.00E+00

032105#1

| Film Up | | | Film Down | | | C2 | | |
FREQUENCY	C	R_G	FREQUENCY	C	R_G	FREQUENCY	C	R_G
1.00E+05	5.34E-12	0.00E+00	1.00E+05	5.08E-12	1.00E+04	1.00E+05	5.30E-13	-3.00E+05
1.79E+05	5.26E-12	0.00E+00	1.79E+05	5.07E-12	0.00E+00	1.79E+05	5.80E-13	-1.00E+04
2.58E+05	5.26E-12	0.00E+00	2.58E+05	5.07E-12	0.00E+00	2.58E+05	5.80E-13	0.00E+00
3.37E+05	5.26E-12	0.00E+00	3.37E+05	5.08E-12	0.00E+00	3.37E+05	5.80E-13	0.00E+00
4.17E+05	5.30E-12	0.00E+00	4.17E+05	5.10E-12	1.00E+02	4.17E+05	5.80E-13	0.00E+00
4.96E+05	5.30E-12	0.00E+00	4.96E+05	5.10E-12	1.00E+02	4.96E+05	5.80E-13	0.00E+00
5.75E+05	5.30E-12	0.00E+00	5.75E+05	5.10E-12	1.00E+02	5.75E+05	5.80E-13	0.00E+00
6.54E+05	5.30E-12	0.00E+00	6.54E+05	5.10E-12	1.00E+02	6.54E+05	5.80E-13	0.00E+00
7.33E+05	5.26E-12	0.00E+00	7.33E+05	5.08E-12	0.00E+00	7.33E+05	5.77E-13	0.00E+00
8.13E+05	5.26E-12	0.00E+00	8.13E+05	5.08E-12	0.00E+00	8.13E+05	5.77E-13	0.00E+00
8.92E+05	5.26E-12	0.00E+00	8.92E+05	5.09E-12	0.00E+00	8.92E+05	5.78E-13	0.00E+00
9.71E+05	5.25E-12	0.00E+00	9.71E+05	5.09E-12	0.00E+00	9.71E+05	5.76E-13	0.00E+00
1.05E+06	5.25E-12	0.00E+00	1.05E+06	5.09E-12	0.00E+00	1.05E+06	5.77E-13	0.00E+00
1.13E+06	5.25E-12	0.00E+00	1.13E+06	5.09E-12	0.00E+00	1.13E+06	5.76E-13	0.00E+00
1.21E+06	5.25E-12	0.00E+00	1.21E+06	5.09E-12	0.00E+00	1.21E+06	5.78E-13	0.00E+00
1.29E+06	5.25E-12	0.00E+00	1.29E+06	5.09E-12	0.00E+00	1.29E+06	5.77E-13	0.00E+00
1.37E+06	5.25E-12	0.00E+00	1.37E+06	5.09E-12	0.00E+00	1.37E+06	5.78E-13	0.00E+00
1.45E+06	5.25E-12	0.00E+00	1.45E+06	5.09E-12	0.00E+00	1.45E+06	5.77E-13	0.00E+00
1.52E+06	5.25E-12	0.00E+00	1.52E+06	5.09E-12	0.00E+00	1.52E+06	5.78E-13	0.00E+00
1.60E+06	5.26E-12	0.00E+00	1.60E+06	5.10E-12	0.00E+00	1.60E+06	5.78E-13	0.00E+00
1.68E+06	5.25E-12	0.00E+00	1.68E+06	5.10E-12	0.00E+00	1.68E+06	5.76E-13	0.00E+00
1.76E+06	5.25E-12	0.00E+00	1.76E+06	5.10E-12	0.00E+00	1.76E+06	5.77E-13	0.00E+00
1.84E+06	5.26E-12	0.00E+00	1.84E+06	5.10E-12	0.00E+00	1.84E+06	5.77E-13	0.00E+00
1.92E+06	5.26E-12	0.00E+00	1.92E+06	5.10E-12	0.00E+00	1.92E+06	5.77E-13	0.00E+00
2.00E+06	5.25E-12	0.00E+00	2.00E+06	5.10E-12	0.00E+00	2.00E+06	5.78E-13	0.00E+00
2.08E+06	5.25E-12	0.00E+00	2.08E+06	5.10E-12	0.00E+00	2.08E+06	5.80E-13	1.00E+02

032805#2

	Film UP	Film Down	C2
Average Capacitance:	5.52E-12	4.07E-12	5.33E-13
Average Distance:	31.46893619	42.7503862	326.4695619
Avg thickness:	295.0006258	283.719176	

31805

	Film UP	Film Down	C2
Average Capacitance:	5.35E-12	6.68E-12	5.80E-13
Average Distance:	32.50276816	26.0159481	299.6201015
Avg thickness:	267.1173333	273.604153	

032105#2

	Film UP	Film Down	C2
Average Capacitance:	7.26E-12	6.50E-12	5.70E-13
Average Distance:	23.95837734	26.759569	305.0027591
Avg thickness:	281.0443818	278.24319	

32505

	Film UP	Film Down	C2
Average Capacitance:	2.58E-12	2.38E-12	5.01E-13
Average Distance:	67.36344147	73.0468768	347.1477013
Avg thickness:	279.7842599	274.100824	

032205#1

	Film UP	Film Down	C2
Average Capacitance:	7.60E-12	5.23E-12	5.55E-13
Average Distance:	22.87868131	33.2717541	313.3364082
Avg thickness:	290.4577269	280.064654	

031705#2

	Film UP	Film Down	C2
Average Capacitance:	5.37E-12	3.98E-12	5.53E-13
Average Distance:	32.36532144	43.6549753	314.0949853
Avg thickness:	281.7296638	270.44001	

031705#1   Film UP   Film Down   C2
   Average Capacitance: 6.49E-12   5.22E-12   5.78E-13
   Average Distance: 26.78588734 33.3151091 300.6356263

   Avg thickness: 273.849739 267.320517

032105#1

                    Film UP   Film Down   C2
   Average Capacitance: 5.26E-12   5.09E-12   5.78E-13
   Average Distance: 33.02265371 34.1477746 300.7396384

   Avg thickness: 267.7169847 266.591864

040205#1

                    Film Up   Film Down
   Average Capacitance: 9.699E-12   6.0068E-12
   Average Distance: 17.92469769 28.9424891

   Avg thickness: 288.2167143 277.609367

FeTb 022205#1

                    Film Up   Film Down
   Average Capacitance: 4.55133E-12 3.8743E-12
   Average Distance: 38.19797047 44.8726543

   Avg thickness: 268.4365862   261.00679

033005#2

                    Film Up   Film Down
   Average Capacitance: 4.337E-12   7.805E-12
   Average Distance: 40.08567472 22.2743845

   Avg thickness: 280.0829648 297.894255

032205#2

                    Film Up   Film Down
   Average Capacitance: 3.095E-12   3.7396E-12
   Average Distance: 56.17175631 46.4893649

   Avg thickness: 273.7925331 283.437335

Appendix B: MathCAD Ray Trace for Spherical Aberration

Spherical aberration of a thin lens.
Calculation of focal length f and ff(corrected), longitudinal Spherical Aberration, and transverse spherical aberation. All lengths in mm. Adapted from:
Optics: Learning by Computing with examples using Mathcad, by K.D. Moller

Input data

lens material:

$n \equiv 1.5$
radius of curvature lens surfaces:

$r1 \equiv 5$
$r2 \equiv 10000$

r1 characterizes the surface nearer the object and r2 characterizes the other surface when an object faces a convex refracting surface the r will be positive. So for a double convex lens r1 is positive and r2 is negative. For a plano convex lens with the convex surface facing the object, r1 is positive, and r2 is very large (positive or negative)
Object distance (negative):
$xo \equiv -20000000$

This value should be negative. Choose a very large value if you want to consider the infinite conjugate situation (parallel incoming beam)
Beam Height:
$ro \equiv 0.1$

1. Calculation of f and xi
Calculation of xi

$$f := \frac{1}{(n-1)\cdot\left(\dfrac{1}{r1} - \dfrac{1}{r2}\right)}$$

$$xi := \frac{1}{\left(\dfrac{1}{f}\right) + \dfrac{1}{xo}}$$

$f = 10.005$
$xi = 10.005$

2. Calculation of ff and xi

$$a(xo) := \left[\left(\frac{1}{r1} - \frac{1}{xo}\right)^2 \cdot \left(\frac{1}{r1} - \frac{n+1}{xo}\right)\right]$$

$$c(xo) := \left[\frac{n^2}{r2} - \frac{n+1}{xo} - \frac{\left(n^2-1\right)}{r1}\right]$$

$$b(xo) := \left(\frac{1}{xo} + \frac{n-1}{r1} - \frac{n}{r2} \right)^2$$

$$ff(xo) := \frac{1}{\left[\frac{1}{f} + \frac{n-1}{n^2} \cdot \left(\frac{ro^2}{2} \right) \cdot (a(xo) - b(xo) \cdot c(xo)) \right]}$$

$$ff(xo) = 10.004$$

Image distance for no Sph Abb

Image distance for Sph Abb

$$xil(xo) := \frac{1}{\left(\frac{1}{xo} + \frac{1}{f} \right)}$$

$$xiisph(xo) := \frac{1}{\left(\frac{1}{xo} + \frac{1}{ff(xo)} \right)}$$

$$xil(xo) = 10.00501$$

$$xiisph(xo) = 10.00384$$

3. Calculation of LSA (Longitudinal Spherical Aberation):

Ray Tracing results:

$$LSAxi(xo) := xil(xo) - xiisph(xo)$$

$$LSAxi(xo) = 0.001167$$

3rd order Seidel Coefficients (Melles Griot):

$$fnumb := \frac{f}{2 \cdot ro}$$

plano convex normal

$$0.272 \cdot \frac{f}{(fnumb)^2} = 0.00109$$

plano convex reversed

$$1.069 \cdot \frac{f}{(fnumb)^2} = 0.00427$$

Ray tracing is more or less exact, the Seidel coefficents give the 3rd order term and ignore higher order terms.

4. Calculation of lateral spherical aberration LAT

$$LAT := LSAxi(xo) \cdot \frac{ro \cdot 2}{xiisph(xo)}$$

$$LAT = 0.000023$$

Appendix C: Operation Manuals for Measurement Equipment
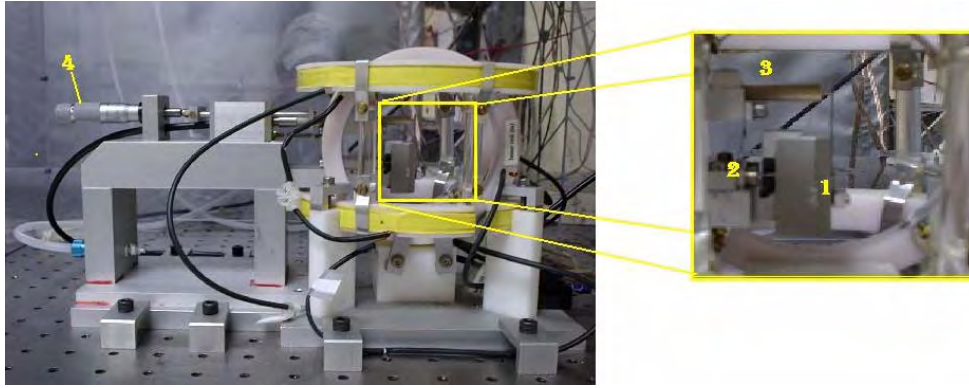
Magnetostriction Setup

Figure C-1

Calibration Procedure:

1. TURN ON EQUIPMENT - Turn on all equipment (computer interface, power supply, oscilloscope, audio amplifier, MTI Photonic Sensor)

2. PLACE SAMPLE - Make sure the optical fiber is withdrawn far enough to avoid making contact with the sample. Place sample in the sample holder (1 in Fig. A) in the center of the Helmholtz coils. It will slide between the sample holder and the copper spring, and be held in place by the spring. The sample holder can be adjusted vertically to change effective length of the sample by increasing the clamping distance. The scale located on the side of the sample holder can be adjusted from 2 to 8 and determines the clamping distance. Generally, measurements should be made at the maximum sample length (8 on the scale) to increase the sensitivity of the measurement by maximizing the magnitude of the deflection.

3. SET CALIBRATION MODE - The MTI Photonic Sensor is now ready to be calibrated. This should be done by first switching the sensor to calibration mode with the MODE switch on the far right side of the sensor.

4. MAXIMIZE VOLTAGE SIGNAL - Use the micrometer (4 in Fig. A) to move the optical fiber closer to the sample. The display on the sensor shows a voltage. The optical fiber should be slowly moved toward the sample until this voltage reaches a maximum value, usually ~1.5V. When approaching the sample, BE CAREFUL, DO NOT LET THE OPTICAL FIBER COME IN CONTACT WITH THE SAMPLE. This can severely damage the sensor.

When the voltage is at a maximum, the sensor is at the optical peak. Figure B illustrates the output of the optical probe versus probe gap.
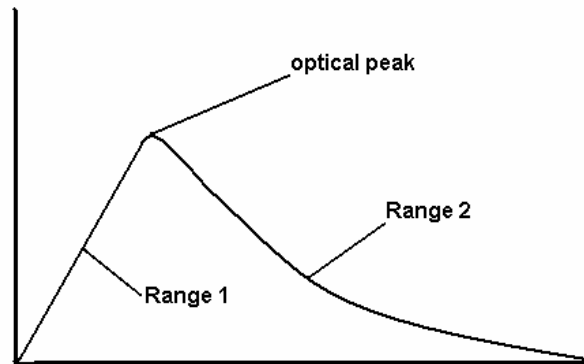

Figure C-2

5. SET CALIBRATION POINT - When the probe is at the optical peak, press the SET CAL button on the sensor, and wait for the system to set the point.

6. SWITCH TO DISPLACEMENT MODE - Set the MODE switch to displacement. This will change the display from volts to microns. The readout will probably be ~33 microns. Remember, this is the value when the probe is at the peak. Measurements should be made in the "Range 1" portion, or on the front slope of the curve (Fig. B).

7. MOVE PROBE INTO RANGE - The probe can be moved into the "Range 1" position by slowly moving it closer to the sample until the display zeros out (+/-.05 is close enough). Again, be careful the probe does not touch the sample.

8. SWITCH TO HIGH GAIN - Once the probe is in range, close the hood covering the setup and switch the gain to "HIGH."

9. ADJUST OFFSET - Adjust the offset knob and again zero the display (+/-.009 is acceptable). Look to the external oscilloscope and adjust it to display the DC Coupling, which will show the deflection of the sample during the measurement. The base line should be as close to zero as possible to ensure that the measurement will stay in the readable range.

10. ALLOW SYSTEM TO STABILIZE – Because the micrometers are oil-driven, the display will drift until the system settles. The system usually takes 15 to 30

minutes to settle enough to begin taking measurements. It may be necessary to readjust the offset after the system stabilizes.

Measurement Procedure:

When a magnetic thin film is exposed to an external magnetic field, the atoms or molecules of the film tend to align parallel to the direction of the applied field. If the magnitude of the field is high enough, the atoms or molecules will elongate, or stretch, thus producing a stress on the substrate, causing it to slightly "bend." If the applied field rotates in a plane parallel to the alignment of the sample, the sample will "vibrate", due to the varying direction of the stress. The photonic sensor in the apparatus essentially measures the maximum deflection of the sample during this vibration.

1. OPEN MAGNETOSTRICTION PROGRAM – After the calibration, the system is now ready to begin measuring. Start by opening the Direct Magnetostriction LabView program on the PC.

2. ADJUST PARAMETERS – Adjust the parameters of the program, i.e. the substrate thickness, film thickness, desired maximum field strength, integration time, number of data points, etc. The clamping distance can be read from the scale on the side of the sample holder. For quick measurements, 20 data points and an integration time of 1 sec. are sufficient. Be sure to enter a sample name that will identify the sample and measurement for later analysis.

3. RUN MEASUREMENT – During the course of the measurement, the strength of the magnetic field is displayed, along with the deflection and calculated magnetostriction above the plot area in the program. The oscilloscope on the power supply also represents the relative magnitude of the field, and the external oscilloscope displays the relative magnitude of the deflection, during intervals when the magnetic field is being applied.

4. ANALYZE DATA – When the measurement is complete, a graph will appear in the plot area of the magnetostriction program. This is a plot of the maximum deflection (in micrometers) as a function of applied magnetic field (Oe). The data file is also saved in a designated folder, and can be imported into Excel for further analysis.

Measuring Substrate Thicknesses Using the Agilent 16451B Dielectric Test Fixture and the 4192A LF Impedance Analyzer

The Agilent 16451B Dielectric Test Fixture can be used to measure substrate thicknesses of conducting samples using the properties of capacitance. Simply speaking, the Agilent 16451B Dielectric Test Fixture can be used as a capacitor, having an accuracy of up to .0001 pF (10^{-16} F) depending on AC frequency. By measuring the capacitance between the test sample and the electrode, the distance between the sample and the electrode can be calculated using the equation,

$$D_1 = \varepsilon_0 * A / C_1 \qquad \textit{Equation C-1}$$

where D_1 is the distance between the electrode and the sample, ε_0 is the permittivity of free space, A is the area of the electrode and C is the measured capacitance.

By removing the sample and again measuring the capacitance (C_2), the distance between the two electrodes (D_2), can be determined via the same equation.

The thickness of the sample (T) can then be determined by subtracting D_2 from D_1.

$$T = D_2 - D_1 \qquad \textit{Equation C- 2}$$

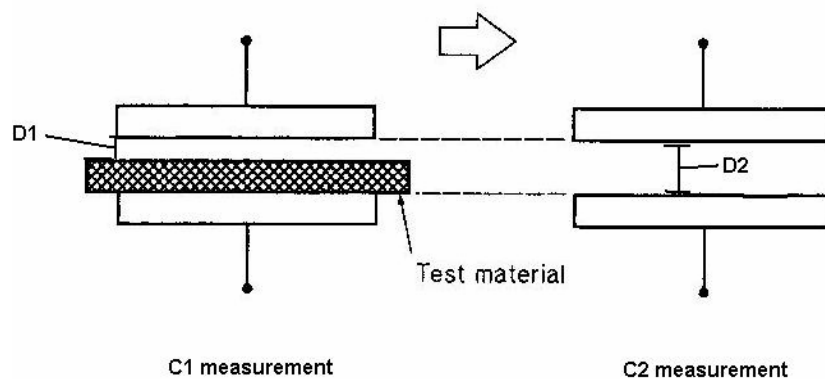An illustration of the measurement procedure is provided below:

Figure C-3

Using the Agilent 16451B and the 4192A Impedance Analyzer to measure capacitance

The Agilent 16451B uses 2 electrodes to form a capacitor. The bottom unguarded electrode is fixed and is not interchangeable. The top electrode can be interchanged to select a size appropriate for a given sample. Most of the samples being used in the magnetostriction setup generally have a width less than 10mm, because of the geometry of the magnetostriction setup sample holder. The 5mm diameter electrode is the best choice for these samples. The dimensions of the unguarded electrode and the 5 mm electrode are shown below.
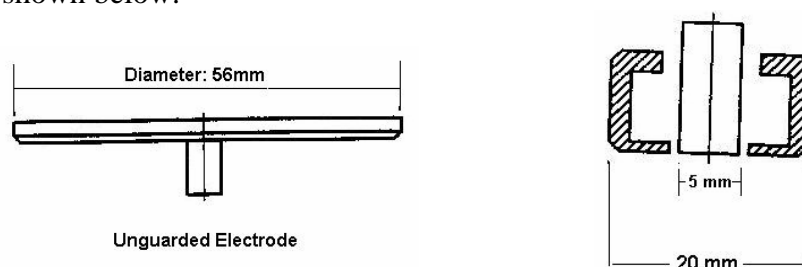

Figure C-4

Before making measurements using the Agilent 16451B, it is important to introduce the equipment being used. Below is a labeled schematic of the Agilent 16451B.

Figure C-5
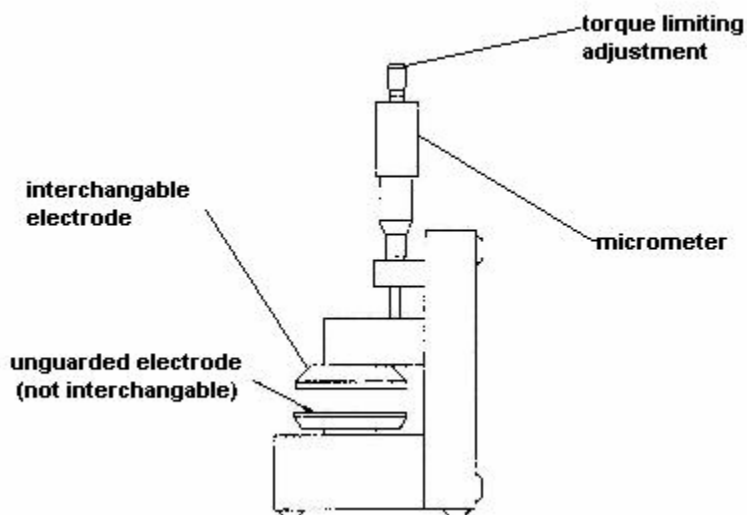
when adjusting the distance between the electrodes, it is important to adjust the micrometer from the torque limiting adjustment at the end of the micrometer. This will prevent over tightening, which can damage the micrometer.

Connect the Agilent 16451B Dielectric Test Fixture to the 4192A LF Impedance Analyzer by locking the connectors of the Agilent 16451B to the corresponding inputs on

the impedance analyzer. Also, make sure the DC bias voltage is off (on the back of the analyzer).

Turn on the Impedance Analyzer and set display (A) to capacitance mode, and select the series circuit mode located near the bottom of the analyzer. Next, set Display (B) to R/G. This will give a measurement of R in (Ω) for series mode and G in (S) for parallel mode.

Place the test sample on the bottom electrode and center it under the 5mm circle of the top electrode. Now move the top electrode closer to the sample. Position the top electrode as close to the sample as possible WITHOUT touching it. You will notice the capacitance on display (A) sharply increase and go out of range if the electrode comes in contact with the sample. If this occurs just back the electrode off. Again, use the torque limiting adjustment of the micrometer to avoid damage.

When conducting curvature measurements, it is important to measure the sample with the convex side upwards first to insure that the sample will fit between the electrodes after it is flipped. The position of the electrodes should not be changed during the measurement process.

The equipment is now ready to begin taking measurements for C_1. Select an AC frequency at which to measure the capacitance with the sample in place. Past measurements have shown that the best results were obtained at a frequency range of 100 kHz – 2 MHz. Frequencies lower than this range usually yield unreliable and inaccurate data, and frequencies above this range tend to posses a high serial resistance, thus compromising the accuracy of the measurements. The graph below is actual data collected from this procedure:
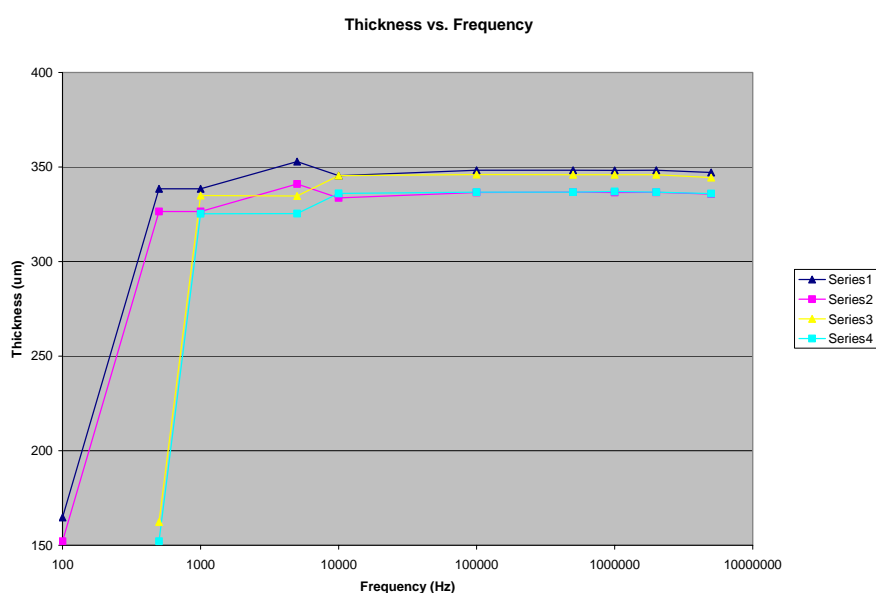

Figure C-6

It is clear from this data that low frequencies do not provide accurate measurements. Likewise, as the frequency exceeds ~ 2 MHz, the graph tends to fall off. The optimal

frequency range is the point at which the graph looks the consistent, and according to this data that would be the range from ~ 100 kHz to about 2 MHz.

After capacitance measurements have been recorded for several different frequencies within the suggested range, the sample can be removed (WITHOUT MOVING THE ELECTRODES). The capacitance measurement procedure can be repeated with the sample removed to determine C_2. These measurements should be made at the same frequencies as those previously used to determine C_1.

After measuring C_1 and C_2, the distance between the electrode and the sample (D_1) and the distance between the electrodes (D_2) can be calculated via equation (1). Furthermore, the thickness of the sample (T) can be determined using equation (2).

Many times when a thin film is deposited onto a substrate, the film will put a stress on the substrate causing the sample to deform. Because the sample is no longer perfectly flat, thickness measurements will vary depending on the curvature of the sample. The illustration below is an exaggerated example of this case.

Sample Orientaion A (convex up)   Sample Orientation B (concave up)
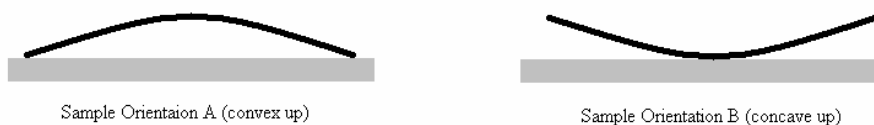
Figure C-7

To determine the curvature of a sample, use the above procedure to determine its thickness and then flip the sample over and re-measure the thickness. If the sample is not completely flat, these measurements will be different. If the sample is convex up (Sample Orientation A), the thickness will vary from the true thickness that is measured with the sample oriented with the concave side up assuming both samples are measured in the center. By comparing the differences in the thickness, the curvature of the sample can be determined.

<u>Kerr Tracer/Scanning Kerr Microscope</u>

Scan profile program
Called VINscan_profile_runningX8
This program continuously scans the intensity of a single line. The user can determine the following:

- Orientation (horizontally/vertically)
- Speed
- Sample distance
- Length of the line
- Position; the user can change the position of the scan real-time

Use: This program can be used to estimate the current spot size by scanning over a surface with a sharp intensity step.

Step by step instructions

1. First you set:
   - Sample distance (take a sample every 'sample distance' micron)
   - Length of scanline
   - Speed (max 250micron/s)
   - Orientation

   Note: Make sure the sample rate is below 70Hz and the number of samples is below 220!

2. Make sure the DC signal is within the <u>DC-Voltmeter (HP3457A) range</u>.
3. Position the laser spot to the right place using the "STEPMOTOR" program
4. Hit the "Start Scanning" button to start scanning!
   - The intensity graph is given in the upper right graph
   - The derivative is given in the upper left and
   - the absolute value of the derivative is in the lower left graph with some peak detection options
   - Some smoothing filters can be applied if necessary
5. Push "Stop scanning" to stop! This button ensures that scanning will end at the same position it started.

Measure Kerr Hysteresis curves

Called Measure_kerr_all_hp3457A_next_switching2
This program can measure both Kerr ellipticity and Kerr rotation at different field values.

Use: This program is used to measure the Hysteresis of a particular sample (or spot on sample)

Step by step instructions
1. If you want to save the results you can set 'sample name' and 'operator name' en set 'save results' to 'yes'.
2. ADVANCED SETTINGS
   a. You can change what is measured on which Lock-In-Amplifier (A or B).
   b. Time constant of the Lock-in-amps and time between taking samples can bet set, but most of the time you can leave these settings at their default value. (time between samples should always be greater than the time constant)
   c. Put the resistor in series for smaller possible field steps. (about .25 Gauss with and .50 Gauss without).
   d. You can set the step size used for building up the initial field.
   e. Leave 'delete duplicate datapoints' checked.
3. Set "stepsize regions"
   • You can set the step size which is used to set the field for different regions and for both up and downward direction.
   • Normally you should choose one direction and use 'mirror values option'
      a. Upward direction
         Go from low to high and define the start field value, the end field value, and the step size that is used in between those values. Then define the next region (take the 'starting field value' of your last used 'end field value') so that they are connected.
4. make sure the used Gauss/Volt value is correct.. you can measure these values using the SCAN-SURFACE program.
5. Run program to start measuring

Scan Surface

Called Vinscan_surface_application12
With this program surface scans can be made using both Kerr Ellipticity and rotation at the same time (the DC intensity is also measured). The program also includes buttons that will start
1. the "Measure Kerr Hysteresis curves" program.
2. A surface scan viewer/editor

Step by Step instruction on how to make a surface scan
1. Press the 'Measurement Points configuration' button and enter:
   - which Gauss value to go to (always assume you start at zero)
   - and what stepsize is to be used
   - what kind of scan to make
     1: take on scan when the desired Gauss value has been reached
     E: take a scan every step (smallest stepsize is about .25 with resistor/ .50 without   resistor)
     N: take no scan
2. Press the 'Scan Surface – configuration' button to
   1. Define the orientation scanning will take place
   2. Enter the length of the scanline, sample distance, scan speed(max 250micron/s), distance between scanlines and the number of scanlines (speed between scanlines should normally be the same as scan speed)
3. Hit 'Scan Surface' to start scanning

You should normally check if all the desired gauss values are reached correctly.. do this by selecting setting 'number of scanlines' to 1 and do a test run.

If you want to reach a desired value very accurately then go there slowly.
For taking consecutive scans with the smallest possible field interval use the 'E' (every scan) option and set the step to .12 gauss if you're using the resistor and to .25 gauss if you're not.
(the smallest step taken will still be .25 or .5 Gauss)

EXAMPLE 1:
Goto 100 Gauss to saturate the sample and than back up to about -20 Gauss to do some scans with the smallest stepsize. And make some scans in between at 300 and at 'exactly' 0 zero Gauss

Then your table should look something like this:

Goto	Stepsize	1 / E/ N
100	20	1
10	20	N
1	1	N
0	.12	1
-16	5	N
-19	1	N
-20	.12	1
-22	.12	E

Press "See scan results" after the scan is done to quickly see your results and save them
Press "Start results analyzer" to more accurately inspect and edit your results

Results Analyzer

Used to manipulate and view surface scanning results.

The main screen is split up in two parts: Top and Bottom. Both with the same functionality of viewing/loading/saving and manipulating surface scanning results. You choose which side (up or down) to manipulate by using the 'Select Up/Down' checkbox. You can choose what to display by using the LIA/LIB checkboxes on each side.

Operations you can perform on the scans are:
- Normalize LI's
  Performs a global normalization; after this operation the lowest value found in the consecutive LIA/LIB scans will be 0 and the highest will be 1.
- Normalize LI with DCV
  Divides all LIA/LIB scans by the associated DV-voltage scans.
- Subtract current scan from LIA/LIB scans
  Subtracts the currently viewed scan from al the other scans.
- Delete selected scan
  Deletes the currently viewed scan
- Delete all scans on selected side
  Deletes alls scans on the selected side (up/down)
- Copy current scan to other side
  Copy the currently viewed scan (of the selected side) to the currently viewed 'position' (no overwriting) on the other side.

The Align Graphs tab-window
This is used to align scan that are shifted with respect to each other on a pixel by pixel basis
Usage:
- Use the cursor to select a common pixel that you want to align to in each successive scan. Every time after setting the cursor press "set alignment point" to store each position.

- Now go to the scan that you want not affected and press "align now" to shift all other scans.

Note: whatever gets shifted out on one side will be shifted back in on the opposite side.

BIBLIOGRAPHY

[1]Etienne du Tremolet de Lacheisserie. *Magnetism Vol I –Fundamentals*. Kluwer Academic. Norwell, MA c2002

[2]Kassap, S.O. *Principles of Electronic Devices*, Boston : McGraw-Hill, c2006

[3]Charles Kittel. *Introduction to Solid State Physics 7th ed*. John Wiley & Sons c1996

[4]Charles Kittel. "Physical Theory of Ferromagnetic Domains" Reviews of Modern Physics **21**,4 (1949)

[5]John R. Reitz, Frederick J. Milford and Robert W. Christy. *Foundations of Electromagnetic Theory*. Reading, Mass. Addison-Wesley, c1979

[6]Victor Antonov, ET. Al. Electronic *Structure and Magneto-Optical Properties of Solids.*. Dordrecht ; Boston : Kluwer Academic Publishers, c2004

[7]Brian Donehew. *Experimental Setup for Measuring the Magneto-optical Kerr Effect Under High Isotropic Pressure*. Master's Thesis – Texas State University-San Marcos c2001

[8]Patrick Holland, Mary Kemptona, et. al. "The magnetic hysteresis of NiFe-31% thin films under isotropic in-plane stress" Journal of Magnetism and Magnetic Materials 250 (2002) L1–L5

[9]Etienne du Tremolet de Lacheisserie. *Magnetostriction-Theory and Applications of Magnetoelasticity* CRC Press, Boca Raton, FL c1993

[10]Bogaart, E.W. "Magnetostriction in thin film ferromagnetic layers for applications in data heads." Kluwer Academic. The Netherlands c2004

[11]Claude Garrett. *Fabrication and Magnetic Properties of Patterned Thin Films*. Master's Thesis – Texas State University-San Marcos c2002

[12]Hinds Instruments. http://www.hindsinstruments.com/PEM_Components/Technology/principlesOfOperation.aspx

[13] L.H. Bennett and R.E. Watson, editors. *Magnetic Multilayers.* Singapore ; River Edge, NJ : World Scientific, c1994

[14] H.W. ten Brinke. "Development of a Scanning Modulating Magneto-Optical Kerr Microscope", Texas State University at San Marcos c2004

[15] Vincent Sombroek. "A Scanning Kerr Microscope for Quantitative Domain Studies on Magnetic Thin Films", Texas State University at San Marcos c2006

[16] M.R.J. Gibbs, Editor. *Modern Trends in Magnetostriction Study and Application.* Kluwer Academic c2000 pp. 57-71

[17] Heng Gong, Maithri Rao, David E. Laughlin, and David N. Lambeth. "Highly oriented NiFe soft magnetic films on Si substrates" Journal of Applied Physics **85**, 8 5750-5753 (1999)

[18] E. Quadt, A. Ludwig, J. Betz, K. Mackay and D. Givord. J. Appl. Phys. 81, 1997, 5420

[19] MTI-2000 Fotonic Sensor manual

[20] E. Klokholm. "The Measurement of Magnetostriction in Ferromagnetic Thin Films" IEEE Transactions on Magnetism 12, 819 (1976)

[21] E. Klokholm and C.V. Jahnes. "Comments on: Magnetostriction and Internal Stresses in Thin Films: the cantilever method revisited" Journal of Magnetism and Magnetic Materials 152, 226-230 (1996)

[22] Etienne du Tremolet de Lacheisserie and J.C. Peuzin. "Magnetostriction and Internal Stresses in Thin Films: the cantilever method revisited" Journal of Magnetism and Magnetic Materials 136, 189-196 (1994)

[23] E.van de Riet. "Deflection of a Substrate Induced by an Anisotropic Thin Film Stress", Journal of Applied Physics 76(1), 584-586 (1996)

[24] Agilent 16451B Dielectric Test Fixture manual

[25] 4192A LF Impedance Analyzer manual

[26] Alex Hubert and Rudolf Schafer. *Magnetic Domains: The Analysis of Magnetic Microstructures.* Springer-Verlag Berlin, Germany c1998 pp.20-31

[27] Edmund Optics. http://www.edmundoptics.com/US/

[28] Anthony E. Seigman. *Lasers*, University Science Books, Mill Valley, CA pp. 675-679

[29] Eugene Hecht. *Optics. 4th edition.* Addison Wesley, 2002 pp. 472-475

[30]Melles Griot. http://www.mellesgriot.com/products/optics/fo_3_2_1.htm

[31]Francis A. Jenkins and Harvey E. White. *Fundamentals of Optics 4th ed.* McGraw Hill pp. 151-161

[32]R.Bonin et. al. "Dependence of magnetization dynamics on magnetostriction in NiFe alloys" Journal of Applied Physics **98**, 123904 (2005)

[33]Soshin Chikazumi. *Physics of Ferromagnetism 2nd Ed.* Oxford University Press, New York c1997

[34]Y. Y. Hu and W. M. Huang. "Elastic and elastic-plastic analysis of multilayer thin films:Closed-form solutions" Journal of Applied Physics **96** 4154 (2004)

[35]Robert O'Handley. *Modern Magnetic Materials: Principles and Applications*. John Wiley & Sons Inc. c2000

VITA

Joel H. Dunn Jr. was born in Wharton, Texas, on November 1, 1980, the son of Agnes Dunn and Joel Dunn Sr. After completing his work at Wharton High School in Wharton, Texas in 1999, he attended Wharton County Junior College before attending St. Mary's University in San Antonio, Texas in 2002. In the fall of 2002 he transferred to Texas State University-San Marcos and completed his Bachelor of Science in Physics in August 2004. In the spring of 2005 he entered the Graduate College at Texas State to pursue his Master of Science. During his graduate studies, he was employed as a research assistant and an instructional assistant. He completed his Master of Science in Physics in May 2006.

Permanent Address: 1350 N LBJ

                       San Marcos, Texas 78666

This thesis was typed by Joel H. Dunn Jr.